From Thought to Action

by

Lakshminarayan Srinivasan

S.M. Electrical Engineering & Computer Science
Massachusetts Institute of Technology, 2003

B.S. Electrical & Computer Engineering
California Institute of Technology, 2002

Submitted to the Department of Electrical Engineering & Computer Science
in partial fulfillment of the requirements for the degree of

Doctor of Philosophy

at the

MASSACHUSETTS INSTITUTE OF TECHNOLOGY

September 2006

Signature of Author: ______________________________
Department of Electrical Engineering & Computer Science
August 11, 2006

Certified by: ______________________________
Emery N. Brown
Professor of Brain & Cognitive Sciences and Health Sciences & Technology

Certified by: ______________________________
Sanjoy K. Mitter
Professor of Electrical Engineering & Computer Science and Engineering Systems

Accepted by: ______________________________
Arthur C. Smith
Chairman, Department Committee on Graduate Students

From Thought to Action

by

Lakshminarayan Srinivasan

Submitted to the Department of Electrical Engineering & Computer Science
on September 1, 2006, in partial fulfillment of the
requirements for the degree of
Doctor of Philosophy

Abstract

Systems engineering[1] is rapidly assuming a prominent role in neuroscience that could unify scientific theories, experimental evidence, and medical development. In this three-part work, I study the neural representation of targets before reaching movements and the generation of prosthetic control signals through stochastic modeling and estimation.

In the first part, I show that temporal and history dependence contributes to the representation of targets in the ensemble spiking activity of neurons in primate dorsal premotor cortex (PMd). Point process modeling of target representation suggests that local and possibly also distant neural interactions influence the spiking patterns observed in PMd.

In the second part, I draw on results from surveillance theory to reconstruct reaching movements from neural activity related to the desired target and the path to that target. This approach combines movement planning and execution to surpass estimation with either target or path related neural activity alone.

In the third part, I describe the principled design of brain-driven neural prosthetic devices as a filtering problem on interacting discrete and continuous random processes. This framework subsumes four canonical Bayesian approaches and supports emerging applications to neural prosthetic devices. Results of a simulated reaching task predict that the method outperforms previous approaches in the control of arm position and velocity based on trajectory and endpoint mean squared error.

These results form the starting point for a systems engineering approach to the design and interpretation of neuroscience experiments that can guide the development of technology for human-computer interaction and medical treatment.

Thesis Supervisors:

Emery N. Brown, Professor of Brain & Cognitive Sciences and Health Sciences & Technology
Sanjoy K. Mitter, Professor of Electrical Engineering & Computer Science and Engineering Systems

---

[1] Here "systems engineering" is a surrogate term for a growing intersection between many fields: statistics, control, information theory, inference, and others.

Acknowledgments

This work was made possible by the generous support of advisors, collaborators, colleagues, teachers, funding agencies, friends, and family. Thank you all.

Financial Support
The research stipends granted or offered by the NIH Medical Scientist Training Program (MSTP) Grant (Ruth L. Kirschstein National Research Service Award, T32 GM07753-27), MIT Presidential Fellowship, and NSF Graduate Research Fellowship made it possible for me to think broadly about possible research directions. This research was additionally supported by NSF Grant CCR-0325774 to Sanjoy Mitter, NIDA Grant R01 DA015644 to Emery Brown, and NINDS Grant R01 NS045853-01 to Nicholas Hatsopoulos.

Advisors
Through critical review and discussion, my advisors Emery Brown and Sanjoy Mitter emphasized a systematic and comprehensive approach to research and communication. At the same time, they generously allowed me the freedom to develop and pursue the problems described in this thesis. Committee member Steve Massaquoi offered a distinct perspective that incorporated clinical considerations in movement control. Nancy Kanwisher, my master's thesis advisor, introduced me to experimental design in cognitive neuroscience. I received expert academic advice from my course advisors Richard Mitchell, Martha Gray, and John Wyatt.

Collaborators
Nicholas Hatsopoulos, at the University of Chicago, graciously shared his expertise on dorsal premotor cortex and the recordings from his primate electrophysiology experiments that are the data analyzed in Chapter 4. I spent countless days learning about estimation and point processes from Uri Eden, a graduate student and postdoctoral fellow with Emery Brown until September 2006 when he joined the faculty at Boston University. Uri composed the independent increments proof that is reproduced in Chapter 5.5. Discussions with Alan Willsky about my term project for his course on recursive estimation (MIT course 6.433) developed into Chapter 5.

Colleagues
Members of the Mitter and Brown research labs have fostered an atmosphere of creativity in their discussions. Lav Varshney at MIT, Patrick Purdon at MGH, and Todd Coleman, now at UIUC, have helped me to begin looking beyond the boundaries of this thesis. Andrew Richardson, Simon Overduin, and Emilio Bizzi helped me understand my work in the context of the canon of primate motor physiology.

Friends
I had the good fortune to befriend many labmates and classmates at MIT and Harvard Medical School - I am especially indebted to Benjie Limketkai for our weekly excursions and Ali Shoeb for days of soul-searching discussions. Agedi Boto and Robb Rutledge bolstered my spirits from JHMI and NYU. Conversations with Krishna Shenoy, now at Stanford, continue to help me navigate my pursuit of nirvana.

Family
My family has been a constant source of emotional support and scientific inspiration, including my father Rengaswamy, mother Uma, and brother Shyam.

Contents

Chapter 1

Introduction

1.1 Problem statement

Our ability to complete everyday tasks such as drinking a glass of water or assembling a bookshelf relies on the coordination of sensation and actuation through the estimated 100 billion neurons that compose the human nervous system. Most of us go about our daily routines effortlessly. The true underlying difficulty of these purposeful movements becomes apparent in the attempt to treat diseases such as stroke, Parkinson's disease, and spinal cord injury that lead to severe incapacitation. Research in humanoid robotics also underscores the difficulty of generating systems that produce robust, dexterous, and efficient movement.

The neuroscience of movement control attempts to discover simplifying principles behind how this complex nervous system solves challenging motor tasks. The scientific endeavor attempts to explain and predict empirical observations, while the engineering discipline works to develop medical treatments for motor deficits. This thesis relates to both the scientific and medical engineering concerns of neural movement control.

The research presented here begins in Chapter 4 with a focus on directed reaching movements made with the arm. This study investigates the role of neural activity in dorsal premotor cortex in the representation of visually presented target positions during an instructed delay period before the reaching movement begins. We then examine (Chapter 5) how this target information could be used to constrain estimates of the entire reaching movement trajectory and subsequently be combined with neural activity related to the intended path. Finally, we develop (Chapter 6) a general approach to the design of neural prosthetic devices that may one day enable dexterous control of assistive technology specified directly by neural activity.

1.2 Contributions of the thesis

This thesis contributes to both the scientific and medical engineering aspects of neural movement control. In this section, we describe those contributions in general terms, while a more technical description is provided in the conclusion (Chapter 7).

The average spiking rate of neurons in dorsal premotor cortex (PMd) was previously understood to relate to visually-presented targets before reaching movements. Here (Chapter 4), we clarify this concept, demonstrating that the spiking dependence on the timing of post-target-onset and the history of spiking contribute to target position representation beyond average spiking rates alone. Furthermore, this study represents the first statistical modeling study of PMd spiking that incorporates model selection methods to determine the best description of spiking behavior from a selection of competing models. This analysis reveals that the physical processes that contribute to the structure of spiking activity in PMd include spatially local phenomena such as membrane properties, and possibly distant interactions such as reciprocal connections to other brain regions. Furthermore, the analysis represents a canonical approach to the interpretation of experiments that relate spiking responses to defined stimuli.

Previous studies of reaching movements presented estimation procedures to decode target related neural activity separately from path related neural activity in the brain. This previous work reinforced a view that certain brain regions during particular time intervals relative to a reaching movement are exclusively related to either the target or path to the target. Here (Chapter 5), we instead emphasize the dependence between target and path through a probabilistic description of reaching movements. The resulting analysis represents the first recursive filtering procedure that is capable of combining path and target related neural activity to generate estimates of the entire arm movement, including real time estimates of the target as the movement proceeds.

Estimation procedures for neural prosthetic devices attempt to map neural activity to estimates of the user-intended device state. Previously, these estimation procedures were developed for specific applications, such as arm movement, or typing. Here (Chapter 6), we unify existing approaches for estimation in prosthetic devices to address a wide range of current and emerging applications.

Our contributions to the scientific and engineering aspects of neural movement control develop an approach for approximate estimation based on models using point processes where the sample space has both discrete and continuous components. The relation between these technical contributions and the study of neural movement control are further described in the conclusion (Chapter 7).

Chapter 2

Neurons and the Control of Movement

This chapter introduces concepts in neuroscience that are relevant to subsequent chapters which study target position representation in PMd spiking (Chapter 4), the estimation of reaching movements (Chapter 5), and general-purpose filter design for neural prosthetic devices (Chapter 6).

2.1 Cells of the nervous system and the action potential

The nervous system is composed of neurons, support cells (glia), blood supply (vasculature), and extracellular material (matrix). Each cell in the nervous system is composed of basic elements that are common to all cells. A lipid bilayer membrane defines the boundaries of the cell. Within the cell, organelles are involved in the controlled production and interaction of proteins, sugars, nucleotides, and other molecular constituents. The processes that define the state of the nervous system occur on multiple scales, from molecular interactions to meter-length electrical events. Ultimately, a unified theory of the nervous system would involve phenomena across all these scales. Intermediate steps towards reaching this objective include the statistical characterization of empirical observations, and the development of various biophysical models, each with different explanatory scope. This section describes the electrical potentials that facilitate interactions between neurons and with the world that is external to the nervous system. This discussion is drawn primarily from [1-3].

Protein and protein-sugar channels, receptors, and molecular pumps form a fluid mosaic in the cell membrane, regulating molecular transport and chemical signalling across the lipid bilayer. Each neuron consists of a cell body between 4 and 100 μm in diameter.

Several short roots, called dendrites, and one long trunk, called the axon, extend from the cell body of a typical neuron. A single axon can extend to hundreds of centimeters in length, as with motor neurons that reach from the surface of the brain to the lower sections of the spinal cord.

The action of pumps and channels maintains an ionic concentration gradient across the cell membrane, resulting in a transmembrane electrical potential. In neurons, potassium, sodium, and calcium ions, together with the resistivity of their corresponding ion-selective membrane channels, are the principle determinants of the membrane potential. Among all cell types, neurons are especially capable of rapidly propogating local changes in this membrane potential across the length of the cell through travelling waves called action potentials or spikes. This is due to the dynamics of voltage-sensitive potassium, sodium, and calcium channels. The response is "all-or-nothing," meaning that the membrane potential in any given location along the cell must exceed a threshold to generate a spike. Spikes typically travel away from the cell body along the axon, but possibly also into the dendrites. At the end of the axon, spikes induce the release of chemical neurotransmitters that diffuse across an extracellular gap called the synaptic cleft. These neurotransmitters then bind to receptors on the dendrite of a post-synaptic neuron. The binding of neurotransmitter modulates membrane potentials in the dendrites, that combine and pass a threshold value at the cell body to induce a spike in the post-synaptic neuron.

A set of helper cells called glia also regulate neuron membrane potentials. These include astrocytes, schwann cells, and oligodendrocytes. Astrocytes participate in the uptake of neurotransmitter at the synapse. These cells also form the blood-brain barrier that determines the molecules that diffuse from capillaries to extracellular space surrounding cells. Schwann cells and oligodendrocytes surround axons in a process called myelination. This increases the propagation velocity of a spike and decreases metabolic demand by increasing resistance and decreasing capacitance of the membrane in regular segments. This effectively creates an axon that is composed of passive wires (myelinated segments) that rapidly transmit the membrane potential, interleaved with slower repeaters (unmyelinated segements) that boost the signal.

Neurons that are modulated by a given neuron are described as "downstream" with relation to that neuron. Downstream neurons may be just one synapse away, or modulated via an intervening network of many neurons. Colloquially, the modulation of membrane potentials is referred to as "information processing" when examined within a neuron or network, and "communication" when described as occuring between neurons or networks. These word choices have inspired the analysis of neural systems in analogy to computation and data transmission problems.

A spike generates a transient millivolt or picoampere surge in a measurement electrode that is placed within or outside the cell. An intracellular recording provides observations of isolated spikes that can unambiguously be attributed to an individual neuron. However, intracellular recordings are challenging in live-animal studies because the electrode tip must be stabilized within the cell body while brain matter pulses by millimeters with each heart beat. In contrast, extracellular recordings from a single electrode allow the simultaneous observation of spikes from multiple neurons (typically three). Because the electrode can be placed anywhere within proximity to the cell, it is feasible to stabilize even an array of hundreds of electrodes for recording in live, moving animals. However, the spikes cannot be unambiguously assigned to different neurons simply because the electrodes are not definitively placed within cells. In a process called spike sorting, the differences in action potential shape that arise with distance and other factors, are used to assign detected spikes to individual neurons.

Recordings of neural activity are also available on whole-brain scales, with coarser resolution, and through different modalities. Extracellular recordings from the same electrodes that observe spikes are low-pass filtered to provide local field potentials, which are believed to represent coordinated dendritic input averaged over hundreds of neurons in the vicinity. By adjusting electrode impedence and positioning, averaged activity can be gathered over millions of neurons. This is the case with electrocorticoencephalography (EcoG), electroencephalography (EEG), and other variants that describe electrode placement relative to the dura (the leathery sheath surrounding the brain), the skull, and the scalp. Electrodes placed closer to the brain are able of accessing higher frequency electric potentials without attenuation. Other modalities that support whole-brain imaging on millimeter or coarser scales include magnetoencephalography (MEG) which employs magnetometers, and functional magnetic resonance imaging (fMRI), a variant of MRI anatomical imaging that provides blood flow information that is believed to relate to neural activity.

With current technology, it is virtually impossible to unambiguously verify the anatomical connectivity of a set of neurons in conjunction with electrophysiological recording from those neurons. This makes it diffult to understand how patterns of neural activity are generated from the underlying architecture. Functional magnetic resonance imaging can provide blood flow measurements related to averaged activity of tens of thousands of neurons, complementing diffusion tensor imaging which provides gross-anatomical connectivity. Retrograde electrical stimulation can verify connectivity between neurons separated by a single synapse in conjuntion with electrophysiology, but is currently practical for only a few to tens of neuron pairs. Microscope-based techniques with voltage-contrast dyes are currently being developed to possibly allow detailed functional and anatomical information of a set of hundreds or thousands of neurons.

To circumvent this present-day disjunction between recordings of membrane potentials and precise anatomy, the analysis of electrophysiological data can be made in the context of general anatomical connections that have been previously documented through dissection, staining, microscopy, MRI, diffusion tensor imaging, and other anatomical techniques. In the following section, we discuss the most prominent connections of the brain with a focus on the neural control of movement.

2.2 Functional anatomy of motor control

How does the nervous system work with skeletal muscle and sensory organs to produce controlled movements? This is the central question in motor neuroscience. A detailed enumeration of the cellular and molecular constituents and phenomena of the nervous system is only a starting point in answering this question. Just as in physics, the ultimate goal here is a simple but powerful explanation for a partial or full set of phenomena that are observed. Such a theory of motor control would extract only the essential components of the physiology to reveal operating principles and bounds on performance.

Nevertheless, the initial phase of inquiry involves a cataloging of phenomena placed in the context of anatomical structure. This chapter introduces the nervous system involved in motor control through a description of the anatomy. While in this thesis, we work with electrophysiological phenomena of specific brain regions in relation to behavior, this more general anatomical framework will be important to subsequently interpreting the phenomena in the larger context of interconnected regions and motor control.

2.2.1 Basic Anatomical Orientation

The central nervous system encompasses the brain and spinal cord, while the peripheral nervous system includes nerves that connect the spinal cord to the rest of the body. The brain alone weighs approximately 1.3 kg and contains an estimated 100 billion neurons. On crossection, the brain appears to be segmented into grey and white matter, composed of neuronal cell bodies and myelinated axons, respectively. “Brain regions” correspond to sections of grey matter, while “tracts” and “connections” refer to white matter. The major brain regions are denoted in Figure 2.1. The cortex, latin for bark, includes the outermost layer of brain. Subcortical regions include the thalamus and basal ganglia. The brainstem extends from the spinal cord into the core of the cerebrum, where it terminates at the thalamus. The cerebellum connects to the cerebrum through the brainstem, and contains more cells in a smaller volume than the cerebrum and brainstem together. White matter tracts coarse between and through all of these regions.

Supporting tissue includes the dura which surrounds the brain, vessels which perfuse the brain with blood, and ventricles which communicate cerebrospinal fluid (CSF).

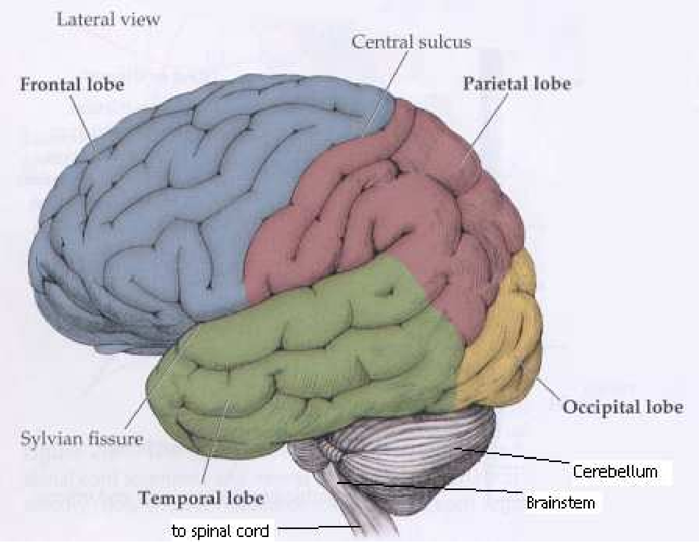

Figure 2.1. Major brain regions. The cortex includes five lobes: frontal, parietal, occipital, temporal, and insular (not visible). Other major brain structures include the cerebellum, brainstem, and basal ganglia (not visible). Adapted from [3].

2.2.2 Historical Context of Motor Anatomy

The modern study of motor control is strongly influenced by a compartmental view of the brain that emerged in the late eighteenth century. Forwarded by German physician Francis Gall, the theory of phrenology described the brain as a composite of 35 organs, each with a different function. The specific claims of this theory have largely been discredited, including the hypothesized functions of brain regions such as "hope" and "veneration." Nevertheless, Gall's notion of compartmentalization was reinforced in the mid-ninteenth and early twentieth century by anatomical and lesion studies that suggested that individual neurons were organized into distinct ensembles to serve specific functions. The proponents of this theory of cellular connectionism include Jackson, Wernicke, Sherrington, and Ramón y Cajal, some of the most vaunted neurophysiologists in history.

In the early twentieth century, Korbinian Brodmann developed a comprehensive anatomical segmentation of the brain. Based on detailed studies of cell types and layering, Brodmann designated 52 brain areas without specifically attributing functions to these areas. This segmentation has been influential in guiding electrophysiological exploration, where it has reinforced the notion of functional homogeneity among anatomically localized brain regions. As a result, the brain is typically described as a circuit consisting of modular brain regions with distinct functions.

Within the past fifteen years, Peter Strick and collegues have employed special staining techniques to provide greater detail with regards to the connectivity of specific brain regions that project motor axons to the spinal cord [4]. Special tracers are injected into a region of interest to selectively follow axons that lead towards or project away from that brain region. One technique based on neurotropic viruses allows the tracer to cross synapses and follow more extended patterns of connectivity. In conjunction with previous anatomical studies, this work has helped to clarify the architecture of brain regions that are located within a few synapses of lower motor neurons which drive skeletal muscle.

Most recently, cubic-millimeter-resolution MRI has enabled longitudinal studies of anatomy in normal living humans. For example, changes in brain anatomy have recently been described with relation to learning, including piano practice [5] and meditation [6]. Diffusion tensor imaging (DTI) is a related technique that allows the segmentation of white matter tracts. The use of fMRI in combination with MRI and DTI holds the promise of inspiring biologically grounded models of phenomena in the normal living human brain that occur at a coarse but broad spatiotemporal scale compared to cellular electrophysiology.

The modern study of neuroanatomy is a nontrivial exercise in deductive reasoning. The brain is an intricate three dimensional structure, composed of more than 100 billion neurons. Within minutes of death, the brain undergoes liquifactive necrosis which destroys anatomy. Typically, fixing agents or cryogenics are employed to preserve structure in a post-mortem preparation. As with most tissue preparations, staining is necessary to make cell structures visible under light microscopy. Various staining procedures interact with the tissue to accentuate different nonspecific features of the cellular structure. Antibody based staining preparations can additionally allow the detection and localization of specific proteins within the tissue. Mass spectroscopy and other methods for sample analysis are able to characterize the molecular constituents of tissue.

All of these methods, from staining procedures to DTI, require inferences to be drawn about the underlying structure and composition of the brain based on measurements. This inference stage is particularly subjective and unverifiable in the case of staining and imaging. Should a spectrum of cell shapes be described in two categories or three? Does a cross-section contain four cell layers or none? Does a pattern of staining represent two distinct regions or one contiguous area? Some assay results are unanimously interpreted, whereas other results require years of training in accepted conventions to provide conformity in interpretation. Consequently, it is essential to qualify the following sections on the anatomy of motor control with the caveat that the brain regions and connections that are described were inferred based on a heterogeneous set of standards that draw on historical precident and were largely verified based on consistency rather than ground truths.

2.2.3 Structure and Connectivity in the Sensorimotor System

The neural control of movement requires the contraction of muscles in coordination with behavioral objectives (goals) and sensory feedback. Classically, motor areas designate neurons that are two synapses away from the muscle, and sensory areas refer to neurons that are one or several synapses from sensory organs, but generally farther from muscle. This distinction has been increasingly weakened by the understanding that in this interconnected “sensorimotor” system, no neuron is exclusively involved in either sensory feedback or muscle contraction. In the following sections, we trace the anatomy of motor control from the sensory organs and muscular actuators of the periphery into the layers of neural structures that govern the relationship between contraction, behavioral objectives, and sensory feedback.

2.2.4 Spinal Cord and Muscle

In total, the spinal cord is an extension of the brain, with long, segregated axonal tracts that relay action potentials towards and away from the brain, and a core of neural cell bodies that include lower motor neurons that extend towards muscle, and secondary sensory neurons that extend towards various parts of the brain (Figure 2.2).

Skeletal muscle is composed of oblong multinucleated cells that are 50-100 μm in diameter and 2-3 cm in length. Each cell is packed with contractile units called sarcomeres that are chained in serial and parallel. Each lower motor neuron in the spinal cord extends its axon to between 100 and 1000 muscle cells, although each muscle cell is innervated by only one lower motor neuron. Lower motor neurons that innervate the same muscle also have cell bodies that cluster into columns within the spinal cord.

The synapse between a lower motor neuron and a muscle cell is called a neuromuscular junction. When the lower motor neuron spikes, acetylcholine is released from the neuron onto the muscle fiber. Receptors on the fiber induce a sequence of molecular events that increase intracellular calcium and initiates contraction of the cell. Energy for this contraction is provided by adenosine triphosphate (ATP) which also drives many other cellular processes.

Peripheral neurons also extend into the spinal cord, modulated by stretch, pressure, and other sensations. These sensations are described as proprioceptive (relating to joint position) or exteroceptive (relating to pressure, pain, or other stimuli applied to the skin). This somatosensory information can be combined with visual and other sensory feedback to guide movements.

Inhibitory interneurons complete a network that connects peripheral sensory neurons, lower motor neurons and additional neurons that both descend from the brain (upper motor neurons) and extend towards the brain (secondary sensory neurons). Reflexive behaviors represent the interaction of peripheral sensory neurons with lower motor neurons through inhibitory interneurons that connect them. To demonstrate the patellar reflex, a subject sits with the thigh supported and leg dangling from a chair. A rubber hammer strikes the tendon of the rectus femoris, resulting in an uninstructed raising of the leg. This behavior can be explained by peripheral sensory activity that directly excites motor neurons to the rectus femoris, and relaxes opposing hamstring muscles through inhibitory interneurons. Several lines of research suggest that spinal cord networks might also allow the execution of more complex motor patterns that are modulated by the brain. For example, cats with full spinal cord transection between the upper and lower leg regions, are still capable of coordinating leg movements while walking on a treadmill, although this effect is not generally observed in analogous injuries to humans.

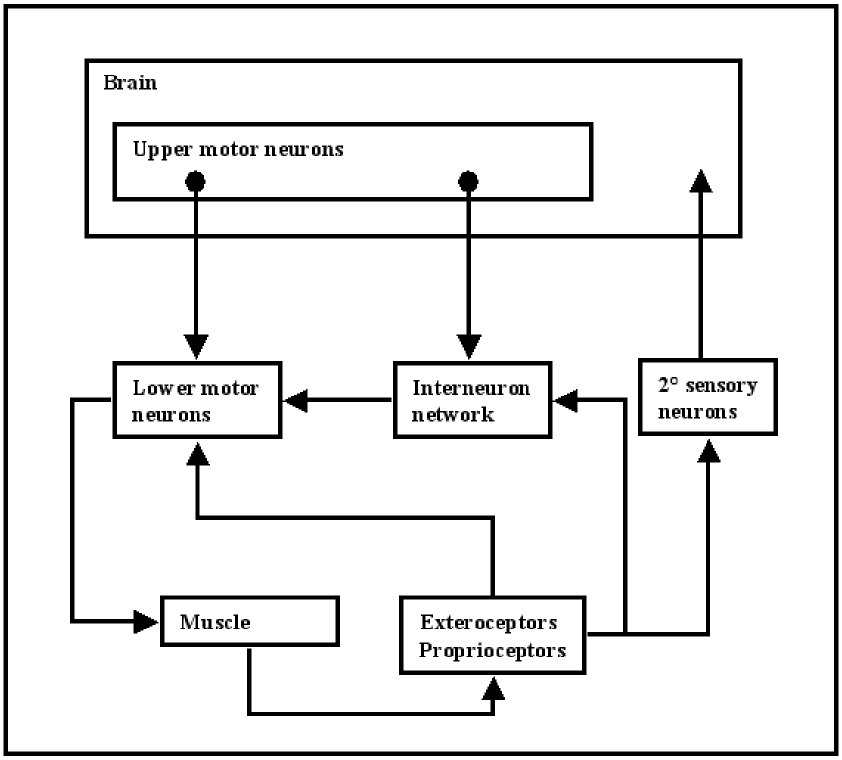

Figure 2.2. Major connections between spinal cord, brain, and periphery.

2.2.4 Cortical Motor Regions

The earliest definition of cortical motor regions in the brain was functional rather than anatomical. In the late ninteenth century, it was discovered that electrical stimulation in areas of the frontal cortex could induce skeletal muscle contraction. These areas were designated as cortical motor regions. It is now known that other brain regions can be stimulated to induce muscle contraction, including the mesencephalic locomotor region in the brainstem that is involved in walking. Conversely, several brain regions are implicated in motor control, although electrical stimulation of those regions does not induce muscle contraction. These include neurons in the basal ganglia, cerebellum, brainstem, somatosensory cortex, posterior parietal cortex, and visual cortex. These regions are collectively denoted "sensorimotor" to describe their involvement in control, although some of these regions are classically described as exclusively sensory or motor based on their proximity to sensory organs or muscle respectively.

A comprehensive view of motor control will likely include all these major sensorimotor areas. However, cortical motor regions continue to dominate the study of voluntary movement due to their expansive connections with other brain regions and especially lower motor neurons and interneurons in the spinal cord. The cortical motor regions are discussed in greater detail here only because this thesis involves a characterization of those neurons as described in subsequent sections. The connectivity of motor cortical regions is also included below, with relation to the other major brain structures involved in motor control.

The current definition of cortical motor regions is both functional and anatomical, and no unequivocal universal standard exists. One definition applies the ninteenth century standard to frontal cortex, and further subdivides motor cortices into primary motor (MI) and premotor (PM) regions based on the minimum level of current injection required to induce muscle contraction, while PM regions require increased thresholds. This approach is convenient for electrophysiologists when detailed post-mortem anatomy is unavailable. However, it is unknown what the relevance of injected current threshold is for the physiological control of movement.

An alternate definition, forwarded by Strick, describes MI based on the level of current injection, but describes PM regions based on anatomical grounds. By injecting retrograde tracers into MI, Strick claimed six distinct brain regions that projected to MI [4]. These regions were labeled dorsal premotor (PMd), ventral premotor (PMv), supplementary motor area (SMA), and rostral, dorsal, and ventral cingulate motor areas (CMAr, CMAd, and CMAv). However, the published staining sections that support this claim have an ambiguous segmentation pattern. This illustrates the difficulty in interpreting tissue stains in terms of anatomical organization. Based on a composite anatomical view, the cortical motor regions are extensively interconnected and linked to other brain regions (Figure 2.3).

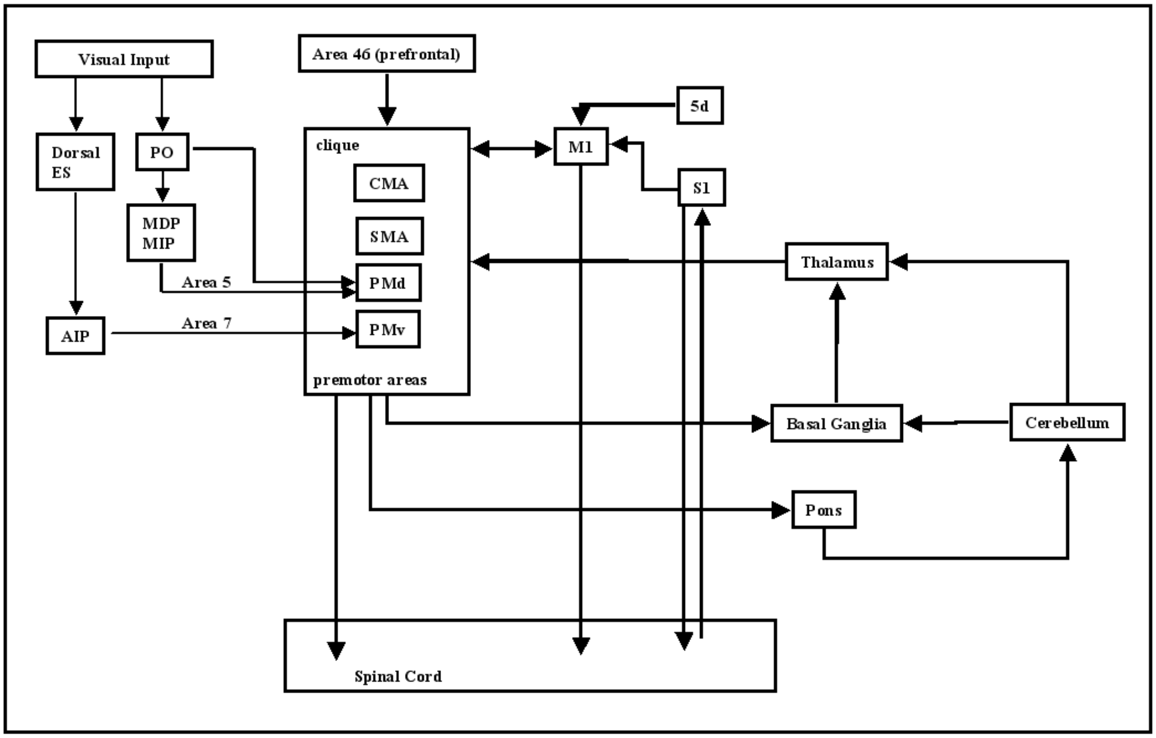

Figure 2.3. Prominent connections among sensorimotor areas of the brain, with detail on cortical structures. This diagram is not complete. For example, other brain regions exist in the brainstem that are involved in motor control and project to the spinal cord. The word clique in the premotor areas box indicates that these circumscribed brain regions are fully interconnected. This diagram is a composite based on [4, 7].

Cells in MI and primary somatosensory cortex (SI) demonstrate somatotopy, a relation between functional characteristics and anatomical location. Somatotopy specifically refers to the pattern of organization by which neigboring cells tend to respond to stimulation of localized sensory organelles or induce contraction in a localized region of musculature. This is the case with muscle contractions induced from current injection in MI, and spiking activity induced in MI through SI and in SI alone from cutaneous stimulation. For example, neurons in one region of MI can be stimulated to induce hand movements. Moreover, the regions of MI that respond to cutaneous stimulation of the hand can also induce contractions in hand muscles with current injection. Neurons in SI project to somatotopically corresponding regions in MI, explaining the somatotopic sensory response in MI. However, the interconnection between SI and MI is not sufficient to explain the coincidence between somatotopies related to sensory stimulation and muscle contraction in MI.

These anatomical relationships alone have inspired models based on control theory that feature a heirarchical and distributed architecture. By definition, anatomy is not sufficient to determine functional properties. Molecular constituents such as channels and neurotransmitter receptors determine the response properties of neurons. Consequently, neurons that appear to be connected in histological sections could instead possibly operate independently. Nevertheless, anatomy at the supra-molecular level represents constraints on the structure of the nervous system that begin to provide a physical context for the various electrophysiological measurements that are commonly made in stimulus-reponse or behavioral experiments.

A comprehensive review of all electrophysiological experiments related to motor control would require several volumes. The following section focuses on the classical delayed reach experiment and previous results that characterize and interpret spiking activity in dorsal premotor cortex during the moments before reaching movements to visually-acquired targets.

2.3 Movement plans and the instructed-delay reach experiment

Motor control experiments are interpreted based on basic themes in control theory and robotics. Elementary control tasks that machines must solve to achieve a goal include choosing a behavior, movement planning, and executing a movement by coordinating the goal with sensory feedback and actuation. Neurophysiologists have sought to attribute each of these tasks to separate groups of neurons in the brain. One prevalent approach involves the characterization of neural activity recorded from a monkey while it is engaged in a task with its arms or hands.

Through analogy with robotic control, neurophysiologists postulated that brain activity related to movement planning could be observed after the target was displayed but before the movement was initiated. Experiments were designed to extend the planning period, presumably to expand the time for which movement planning could be observed. This was the rationale for the delayed reach experiment which is described in the sequel.

The instructed-delay reach experiment is a classical task used in primate electrophysiology to study motor control. In our variant of this task (Figure 2.4), a monkey (*Macaca mulatta*) controls a cursor that it views on a horizonal computer display, through a two-joint manipulandum. Each trial that the monkey must complete involves three stages that choreograph a reaching movement to one of typically eight target locations. The first stage is the hold period, where the monkey is required to place the cursor over a central point. The second stage is the instructed delay period, where a target position is visually indicated, but the monkey is required to maintain the central cursor position for typically 500 to 1000 milliseconds. The third stage is the go period, where the target begins to flash, telling the monkey to proceed to generate a reaching movement that places the cursor at the target. If the target is acquired within 2 seconds of the go signal and held for 500 milliseconds, a water drop reward is delivered to the monkey's mouth.

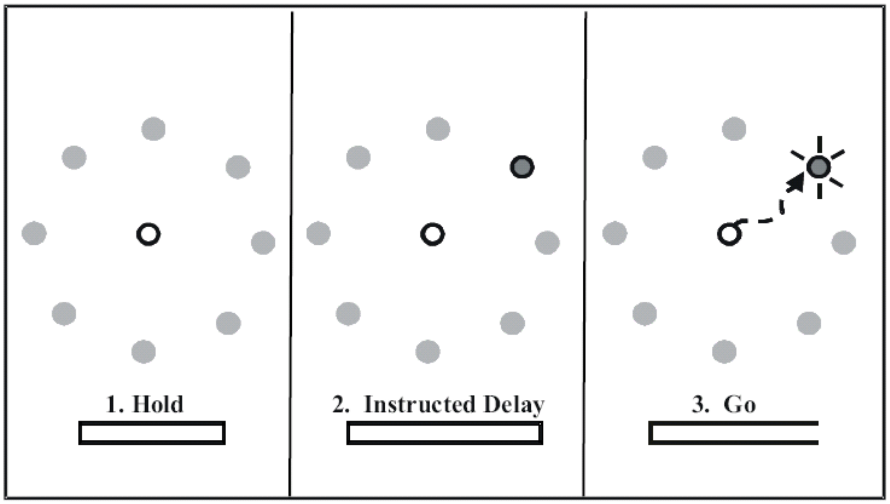

Figure 2.4. One trial of the instructed-delay task as in [8].

We do not naturally pause for any appreciable time before reaching movements. Nevertheless, some neurophysiologists believe that the delay period is an opportunity to study the planning of arm movements. From this perspective, it is important to guarantee that no target-related stimulus is provided during a substantial portion of the delay period. Accordingly, the instructed-delay experiment is modified so that the target is displayed for 150 to 300 milliseconds and then extinguished for the remaining 800 or more milliseconds of the instructed delay period [9]. Without this precaution, neural activity that is observed cannot be attributed to reach planning in exclusion of activity that is directly driven by the visual stimulus.

Although important from this perspective, the extinguished target precaution may not be essential to conduct a realistic study of motor control, because many natural circumstances involve reaching to targets that are visually accessible throughout the entire reaching movement. Reaching movements to an extinguished target may require different neural components than reaching to a continually cued target, but both scenarios could still be relevant to mechanisms of motor planning, and both essentially still involve some period of visual stimulus. The analysis presented in this thesis circumvents this issue by explicitly describing the visually-presented target position as an input to the neural system during the delay period. The assertion is that delay period activity is being characterized under different conditions, but that considering this activity in the context of target position representation is not precluded in either case.

The tracking of eye movements is another consideration in experiment design that is emphasized by some neuroscientists. The rationale for this emphasis is the notion that planning activity related to the spatial location of the target must exist in some reference frame relative to the animal. This reference frame could potentially be retinotopic, where the represented coordinates of the target change with eye position. Alternatively, the reference frame could be body centered, or some other intermediate or arbitrary reference frame. From this view, it might ultimately be desireable for the brain to represent the target in body-centered or other coordinates to allow arm movements to be easily related to the goal. The concept of sensorimotor transformation postulates that an important function of the nervous system is to solve this change of coordinates. This concept has driven efforts to characterize any target-related brain activity in terms of its coordinate frames. Consequently, both eye and hand position, measured during the delay period, are considered important covariates that explain the observed patterns of neural activity.

Eye movements were not recorded in the PMd experiment that is analyzed in this thesis. Hence, they are not available as explanatory variables in constructing models of delay period neural activity. Moreover, eye movements or positions were not specifically constrained. This will add to the potential sources of variation in the patterns of spiking activity that were recorded on multiple trials of the same target presentation. Such a characterization where eye movements are unconstrained could prove especially useful in the context of neural prosthetic devices where it would be particularly taxing to require that the user control their eye position, or intrusive and algorithmically nontrivial to track and correct for eye movements. Additionally, the modulation of PMd spiking by eye position is known to be slight when eye positions are unconstrained [10].

The following sections review qualitative and quantitative studies that were previously performed to understand the representation of visually-instructed target positions in the instructed-delay spiking activity of dorsal premotor cortical neurons. Other brain regions that have been studied in this regard include posterior parietal cortex [11], frontal cortex [12], and subthalamic nucleus [13].

2.4 Previous studies of PMd in movement planning

Premotor dorsal cortex (PMd) and other brain regions have been extensively studied with relation to movement planning in general, and the spiking representation of target position before visually guided reaching movements in particular. Lesions in PMd result in deficits of visually guided arm movements [14]. Specific features of the PMd delay period spiking response vary systematically with aspects of the movement or task. Average delay period firing rates change between trials where different target locations are presented [15]. A mean-normalized measure of across-trial variability decreases over the delay period, and covaries with reaction time [16].

Probability distributions have been used to describe the number of spikes (or other specific features of the response) in a delay period interval for each of a discrete set of targets. Several decoding methods have demonstrated target estimation from the average delay period spiking response of an ensemble of PMd neurons with varying degrees of success [8, 17]. Nevertheless, these studies typically employ unverified Poisson statistical models, and batch estimation procedures in their characterization of PMd target representation.

In contrast, the PMd study described in Chapter 4 of this thesis proceeds with a broader collection of statistical models, coupled to a model selection procedure that assesses both relative and absolute model quality. The resulting analysis demonstrates the extent to which various aspects of the PMd spiking response contribute to target representation, and sheds light on the possible physical processes that might be important to the structure observed in the PMd response.

2.5 The neural prosthetics design problem

Several neurological conditions dramatically restrict voluntary movement, including amyotrophic lateral sclerosis, spinal cord injury, brainstem infarcts, advanced-stage muscular dystrophies, and diseases of the neuromuscular junction. A growing set of technologies is being developed to allow brain-driven control of assistive devices for individuals with severe motor deficits. Variously called brain-machine interfaces [18, 19], motor neural prostheses [20-22], and cognitive prostheses [23, 24], they represent a communication link that bypasses affected channels of motor output.

Many alternative technologies are available that utilize remaining motor function rather than neural activity to generate control signals. Movements of the eye or tongue can be tracked to control a cursor. Suction on a straw can navigate a wheelchair. Contractions or electromyographic signals of larger muscle groups such as the platysma or pectoralis major can be monitored to activate joints in a prosthetic arm [25]. Volitional grasping with a prosthetic hand can be achieved through mechanical cabling to the contralateral shoulder [26]. Although they represent practical solutions for many patients, these alternatives provide restricted control to any user. Moreover, they may not be feasible for individuals with profound motor deficits.

Brain-driven interfaces have the potential to provide users with control that is more dexterous, natural to use, and less susceptible to fatigue than existing muscle-based alternatives. In principle, these interfaces would be available even for individuals with near-complete loss of voluntary motor function, such as with locked-in syndrome where only blinking and vertical gaze remain.

The four common elements of existing brain-driven interfaces are a method to monitor neural activity, an algorithm to map this activity to control signals, a device to be controlled, and a feedback mechanism that informs the user about the state of the device (Figure 2.5). This design problem is multifaceted. The nascent neural prosthetics literature already spans issues related to recording hardware, signal processing, robotics, functional electrical stimulation, clinical care, and surgical techniques.

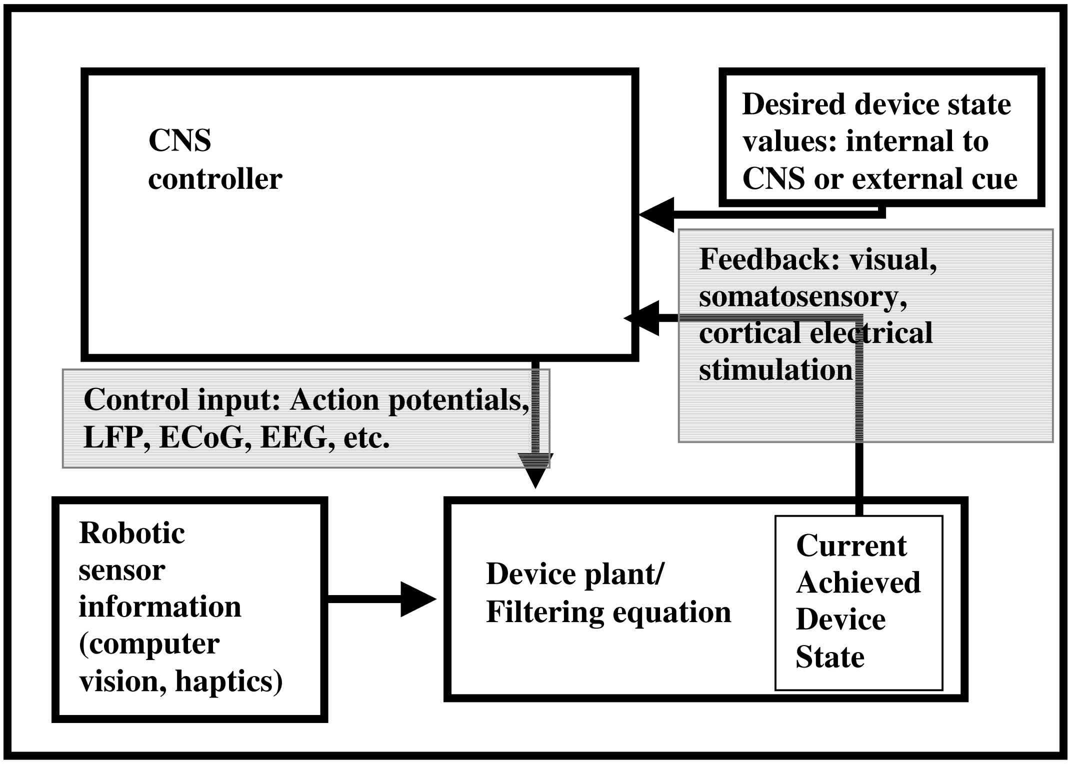

Figure 2.5. Complete circuit diagram of a neural prosthetic device.

Monitoring approaches balance finer spatial resolution and broader frequency bands against the invasiveness of electrode placement. Scalp leads provide waveforms up to 40 Hertz (Hz), integrating activity from square-centimeters of cortex [27]. Subdural leads provide electrocorticographic (ECoG) signals up to 200 Hz that are collected from an estimated area of fractions of a square millimeter [27]. Cortical electrode arrays have access to local field potentials similar to EcoG, but also monitor action potentials, which are transient one-millisecond electrical spikes from micrometer-scale neurons. These arrays typically record from tens but up to hundreds of individual neurons spread over one square millimeter.

Signal pre-processing is typically employed in all of these approaches, including band-pass filtering and spike sorting [28-31], where action potentials are grouped by shape in an effort to localize spiking events to distinct neurons. Various algorithms can then be employed to map neural signals to control signals. This mapping can be made adaptive, changing so as to minimize performance errors even as neurons fade out [32] and the subject learns to use the interface. Feedback in existing prototypes is predominantly limited to visualization of the device state and juice rewards [20-24], or auditory cues, but somatosensory cortical electrodes have also been proposed.

Challenges remain on all fronts in the design of brain-driven interfaces. Cortical electrode arrays have only preliminarily been evaluated for chronic recording in humans [33]. To endure long-term use, monitoring approaches must achieve low power consumption, mechanical stability, biocompatibility, and otherwise reliable access to relevant neural signals. Movements generated by existing prototypes are either slow and deliberate, or fast and uncontrolled. The evaluation of learning is not standardized. Reported training times range from minutes [19] to months [18] for acquiring proficiency with a device, depending on the device and method of performance evaluation. Algorithms must be developed to enable increased dexterity, faster learning, and robust performance. Finally, the optimization of real time feedback and training regimens is largely unexplored.

The mapping of preprocessed neural activity to device control signals is typically approached in two steps (Figure 2.6). First, an algorithm estimates the user's intention for the device based on neural activity that serves as a noisy observation of that intention. Second, a controller acts to bring the device state close to this estimate of the user's intention. This second stage is often implicitly assumed in literature on algorithms for neural prosthetic devices.

The development of neural prosthesis estimation procedures parallels the earlier development of estimation procedures in electrical engineering and later applications to neurophysiology: manually adjusted linear combinations of power spectral band energies

[34], population vectors for automated but sub-optimal linear mappings [35], linear regression for optimized linear mappings [36], and most recently, recursive Bayesian estimation procedures [37-39]. This last advance in particular has allowed dramatically better tracking than linear regression in off-line data analyses. In decoding trajectories or sequences of intentions, this improvement is largely due to the introduction of a state equation, a mathematical expression of underlying structure in the intention, such as continuity. Variants have evolved to progressively account for the true statistical nature of spiking activity: the Kalman filter [39], particle filter [37], and point process filter [38]. Bayesian estimation [23, 24], support vector machines, and other classification methods have also been used with neural observations of discrete intentions that are relevant to prosthetic applications such as icon selection from an on-screen menu.

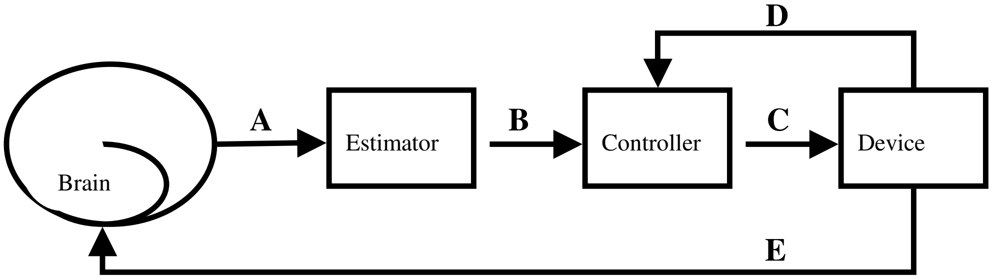

Figure 2.6. Standard approach to the design of neural prosthetic devices. The user expresses neural activity (A) to communicate an intended state for the prosthetic device. An estimator converts this neural activity into an estimate of the intended state (B). A controller generates inputs (C) to drive the prosthetic device to this estimate in coordination with feedback (D) that informs the controller about the device state. The user receives sensory information (E) that serves as an additional level of feedback for guiding the device to the user-intended state.

Two of the chapters in this thesis relate closely to the estimation problem in prosthetic devices. In Chapter 5, an estimation procedure is developed to drive reaching movements of a prosthetic limb from the combination of target-related information (such as from PMd instruted-delay activity) and path related information (such as from MI activity that corresponds to intended velocities) regardless of the specific recording modality. In Chapter 6, a general-purpose estimation framework is developed for a variety of prosthetic devices while incorporating either spiking activity or continuous field potentials.

2.6 References

[1] T. F. Weiss, *Cellular Biophysics: Electrical Properties*, vol. 2. Cambridge, Massachusetts: The MIT Press, 1997.

[2] E. R. Kandel, J. H. Schwartz, and T. M. Jessel, *Principles of Neural Science*, 4th ed. New York: McGraw-Hill, 2000.

[3] H. Blumenfeld, *Neuroanatomy Through Clinical Cases*. Sunderland, Massachusetts: Sinauer Associates, 2002.

[4] R. P. Dum and P. L. Strick, "Motor areas in the frontal lobe of the primate," *Physiol Behav*, vol. 77, pp. 677-82, 2002.

[5] S. L. Bengtsson, Z. Nagy, S. Skare, L. Forsman, H. Forssberg, and F. Ullen, "Extensive piano practicing has regionally specific effects on white matter development," *Nat Neurosci*, vol. 8, pp. 1148-50, 2005.

[6] S. W. Lazar, C. E. Kerr, R. H. Wasserman, J. R. Gray, D. N. Greve, M. T. Treadway, M. McGarvey, B. T. Quinn, J. A. Dusek, H. Benson, S. L. Rauch, C. I. Moore, and B. Fischl, "Meditation experience is associated with increased cortical thickness," *Neuroreport*, vol. 16, pp. 1893-7, 2005.

[7] J. Krakauer and C. Ghez, "Voluntary Movement," in *Principles of Neural Science*, E. R. Kandel, J. H. Schwartz, and T. M. Jessell, Eds., 4th ed. New York: McGraw-Hill, 2000, pp. 756-779.

[8] N. Hatsopoulos, J. Joshi, and J. G. O'Leary, "Decoding continuous and discrete motor behaviors using motor and premotor cortical ensembles," *J Neurophysiol*, vol. 92, pp. 1165-74, 2004.

[9] A. P. Batista, C. A. Buneo, L. H. Snyder, and R. A. Andersen, "Reach plans in eye-centered coordinates," *Science*, vol. 285, pp. 257-60, 1999.

[10] P. Cisek and J. F. Kalaska, "Modest gaze-related discharge modulation in monkey dorsal premotor cortex during a reaching task performed with free fixation," *J Neurophysiol*, vol. 88, pp. 1064-72, 2002.

[11] R. A. Andersen and C. A. Buneo, "Intentional Maps in Posterior Parietal Cortex," *Annual Review of Neuroscience*, vol. 25, pp. 189-220, 2002.

[12] J. D. Schall, "Neural basis of deciding, choosing and acting," *Nat Rev Neurosci*, vol. 2, pp. 33-42, 2001.

[13] Z. M. Williams, J. S. Neimat, G. R. Cosgrove, and E. N. Eskandar, "Timing and direction selectivity of subthalamic and pallidal neurons in patients with Parkinson disease," *Exp Brain Res*, vol. 162, pp. 407-16, 2005.

[14] U. Halsband and R. E. Passingham, "Premotor cortex and the conditions for movement in monkeys (Macaca fascicularis)," *Behav Brain Res*, vol. 18, pp. 269-77, 1985.

[15] M. Weinrich and S. P. Wise, "The premotor cortex of the monkey," *J Neurosci*, vol. 2, pp. 1329-45, 1982.

[16] M. M. Churchland, B. M. Yu, S. I. Ryu, G. Santhanam, and K. V. Shenoy, "Neural variability in premotor cortex provides a signature of motor preparation," *J Neurosci*, vol. 26, pp. 3697-712, 2006.

[17] G. Santhanam, S. I. Ryu, B. M. Yu, A. Afshar, and K. V. Shenoy, "A high-performance brain-computer interface," *Nature*, vol. 442, pp. 195-8, 2006.

[18] J. R. Wolpaw and D. J. McFarland, "Control of a two-dimensional movement signal by a noninvasive brain-computer interface in humans," *Proc Natl Acad Sci U S A*, vol. 101, pp. 17849-54, 2004.

[19] E. C. Leuthardt, G. Schalk, J. R. Wolpaw, J. G. Ojemann, and D. W. Moran, "A brain-computer interface using electrocorticographic signals in humans," *J Neural Eng*, vol. 1, pp. 63-71, 2004.

[20] J. M. Carmena, M. A. Lebedev, R. E. Crist, J. E. O'Doherty, D. M. Santucci, D. F. Dimitrov, P. G. Patil, C. S. Henriquez, and M. A. Nicolelis, "Learning to control a brain-machine interface for reaching and grasping by primates," *PLoS Biol*, vol. 1, pp. E42, 2003.

[21] M. D. Serruya, N. G. Hatsopoulos, L. Paninski, M. R. Fellows, and J. P. Donoghue, "Instant neural control of a movement signal," *Nature*, vol. 416, pp. 141-2, 2002.

[22] D. M. Taylor, S. I. Tillery, and A. B. Schwartz, "Direct cortical control of 3D neuroprosthetic devices," *Science*, vol. 296, pp. 1829-32, 2002.

[23] K. V. Shenoy, D. Meeker, S. Cao, S. A. Kureshi, B. Pesaran, C. A. Buneo, A. P. Batista, P. P. Mitra, J. W. Burdick, and R. A. Andersen, "Neural prosthetic control signals from plan activity," *Neuroreport*, vol. 14, pp. 591-6, 2003.

[24] S. Musallam, B. D. Corneil, B. Greger, H. Scherberger, and R. A. Andersen, "Cognitive control signals for neural prosthetics," *Science*, vol. 305, pp. 258-62, 2004.

[25] T. A. Kuiken, G. A. Dumanian, R. D. Lipschutz, L. A. Miller, and S. K.A., "Targeted muscle reinnervation for improved myoelectric prosthesis control," *Proc 2nd Internat IEEE EMBS Conf on Neural Engineering*, pp. 396-399.

[26] D. D. Frey, L. E. Carlson, and V. Ramaswamy, "Voluntary-Opening Prehensors with Adjustable Grip Force," *Journal of Prosthetics & Orthotics*, vol. 7, pp. 124-131, 1995.

[27] W. J. Freeman, M. D. Holmes, B. C. Burke, and S. Vanhatalo, "Spatial spectra of scalp EEG and EMG from awake humans," *Clin Neurophysiol*, vol. 114, pp. 1053-68, 2003.

[28] E. H. D'Hollander and G. A. Orban, "Spike recognition and on-line classification by unsupervised learning system," *IEEE Trans Biomed Eng*, vol. 26, pp. 279-84, 1979.

[29] F. Worgotter, W. J. Daunicht, and R. Eckmiller, "An on-line spike form discriminator for extracellular recordings based on an analog correlation technique," *J Neurosci Methods*, vol. 17, pp. 141-51, 1986.

[30] M. S. Fee, P. P. Mitra, and D. Kleinfeld, "Automatic sorting of multiple unit neuronal signals in the presence of anisotropic and non-Gaussian variability," *J Neurosci Methods*, vol. 69, pp. 175-88, 1996.

[31] R. Chandra and L. M. Optican, "Detection, classification, and superposition resolution of action potentials in multiunit single-channel recordings by an on-line real-time neural network," *IEEE Trans Biomed Eng*, vol. 44, pp. 403-12, 1997.

[32] U. T. Eden, W. Truccolo, M. R. Fellows, J. P. Donoghue, and E. N. Brown, "Reconstruction of hand movement trajectories from a dynamic ensemble of spiking motor cortical neurons," *Proc 26th IEEE Engineering in Medicine and Biology Society Annual Conference (EMBC '04)*, vol. 2, pp. 4017- 4020, 2004.

[33] L. R. Hochberg, J. A. Mukand, G. I. Polykoff, G. M. Friehs, and J. P. Donoghue, "Braingate neuromotor prosthesis: nature and use of neural control signals," *Program No. 520.17. Abstract Viewer/Itinerary Planner, Washington, DC: Society for Neuroscience Online*, 2005.

[34] J. R. Wolpaw and D. J. McFarland, "Multichannel EEG-based brain-computer communication," *Electroencephalogr Clin Neurophysiol*, vol. 90, pp. 444-9, 1994.

[35] A. P. Georgopoulos, A. B. Schwartz, and R. E. Kettner, "Neuronal population coding of movement direction," *Science*, vol. 233, pp. 1416-9, 1986.

[36] J. Wessberg, C. R. Stambaugh, J. D. Kralik, P. D. Beck, M. Laubach, J. K. Chapin, J. Kim, S. J. Biggs, M. A. Srinivasan, and M. A. Nicolelis, "Real-time prediction of hand trajectory by ensembles of cortical neurons in primates," *Nature*, vol. 408, pp. 361-5, 2000.

[37] A. E. Brockwell, A. L. Rojas, and R. E. Kass, "Recursive bayesian decoding of motor cortical signals by particle filtering," *J Neurophysiol*, vol. 91, pp. 1899-907, 2004.

[38] U. T. Eden, L. M. Frank, R. Barbieri, V. Solo, and E. N. Brown, "Dynamic analysis of neural encoding by point process adaptive filtering," *Neural Comput*, vol. 16, pp. 971-98, 2004.

[39] W. Wu, Y. Gao, E. Bienenstock, J. P. Donoghue, and M. J. Black, "Bayesian population decoding of motor cortical activity using a Kalman filter," *Neural Comput*, vol. 18, pp. 80-118, 2006.

[40] T. M. Cowan and D. M. Taylor, "Predicting reach goal in a continuous workspace for command of a brain-controlled upper-limb neuroprosthesis," *Proc 2nd Internat IEEE EMBS Conf on Neural Engineering*, pp. 74, 2005.

[41] C. Kemere and T. H. Meng, "Optimal estimation of feed-forward-controlled linear systems," *Proc IEEE International Conference on Acoustics, Speech and Signal Processing (ICASSP '05)*, vol. 5, pp. 353-356, 2005.

[42] L. Srinivasan, U. T. Eden, A. S. Willsky, and E. N. Brown, "Goal-directed state equation for tracking reaching movements using neural signals," *Proc 2nd Internat IEEE EMBS Conf on Neural Engineering*, pp. 352-355, 2005.

[43] B. M. Yu, G. Santhanam, S. I. Ryu, and K. V. Shenoy, "Feedback-directed state transition for recursive Bayesian estimation of goal-directed trajectories," *Computational and Systems Neuroscience (COSYNE) meeting abstract, Salt Lake City, UT*, 2005.

Chapter 3

Modeling and Filtering Point Processes

This chapter introduces concepts in statistical modeling and estimation that are applied in subsequent chapters to the study of target position representation in PMd spiking (Chapter 4), the estimation of reaching movements (Chapter 5), and general-purpose filter design for neural prosthetic devices (Chapter 6).

3.1 The point process in continuous time

Consider a recording of spiking activity from a single neuron over a time interval $\left[0,T\right)$, where the sequence of spike times is given by $0 < w_1 < w_2 < ... < w_m < T$. Let the counting process $N(t)$ represent the cumulative spike count from the start of the interval up to time t. The evolution of this counting process may depend causally on continuous random processes $x(t)$, discrete random processes $s(t)$, or counting processes $L(t)$ that describe the state of the biological neural network or its inputs, including the neuron's own spiking history. Define the history of these random processes as $H_t = \left\{ x(\tau), s(\tau), L(\tau) \mid \tau \in [0,t) \right\}$.

We describe this spiking activity as a point process [1-5]. The point process is completely specified by its conditional intensity function [2], defined as follows:

$$\lambda(t \mid H_t) = \lim_{\Delta \to 0} \frac{P\left[N(t+\Delta) - N(t) \mid H_t \right]}{\Delta} \tag{3.1}$$

This conditional intensity function characterizes the joint data probability of observing a particular experimental outcome represented by the realized counting process $N(t)$, over the interval $\left[0,T\right)$:

$$P\left(\left\{N(\sigma)\,|\,\sigma\in[0,T)\right\}\right)=\exp\left[\int_0^T\log\lambda(\sigma\,|\,H_\sigma)dN(\sigma)-\int_0^T\lambda(\sigma\,|\,H_\sigma)d\sigma\right] \tag{3.2}$$

where $\int_0^T\log\lambda(\sigma\,|\,H_\sigma)dN(\sigma)\triangleq\sum_{i=1}^{m}\log\lambda(w_i\,|\,H_{w_i})$ is a Riemann-Stieltjes integral [2].

3.2 The point process in discrete time

We now introduce additional notation to represent the point process in discrete time, and to describe the spiking activity of an ensemble of neurons instead of just one neuron. Divide the recording interval $\left[0,T\right)$ into k discrete time steps, each of length $\delta=T/k$ seconds, so that the k^{th} timestep is $\left[(k-1)\delta,k\delta\right)$. Define the number of spikes that arrive for neuron c in the k^{th} timestep as $n_k^c=\int_{(k-1)\delta}^{k\delta}N(\sigma)d\sigma$. The ensemble spiking activity of C neurons at the k^{th} timestep is denoted $n_k^{1:C}=\left(n_k^1,n_k^2,...,n_k^C\right)$. Let $x_k=x((k-1)\delta)$ and $s_k=s((k-1)\delta)$. Define $x_{1:k}=\left(x_1,x_2,...,x_k\right)$, and similarly for $s_{1:k}$. The discrete-time history is accordingly $H_k=\left(n_1^{1:C},n_2^{1:C},...,n_{k-1}^{1:C},x_{1:k-1},s_{1:k-1}\right)$.

The conditional intensity of neuron c evaluated in discrete time is given by $\lambda_k^c=\lambda^c((k-1)\delta\,|\,H^t)$ in units of spikes per second. Consider time steps δ that are chosen to be smaller than the refractory period, typically 1×10^{-3} seconds, so that n_k^c is either 0 or 1. The discrete-time joint data probability is then approximated [6] to resemble the continuous-time data likelihood (3.2) as follows:

$$p(n_1^{1:C},n_2^{1:C},...,n_K^{1:C})=\prod_{c=1}^{C}\exp\left\{\sum_{k=1}^{K}\log\left[\lambda_k^c\delta\right]n_k^c-\sum_{k=1}^{K}\lambda_k^c\delta\right\} \tag{3.3}$$

The corresponding discrete-time probability density of the ensemble spiking activity at time k conditioned on the history and the discrete and continuous states at time k is given by:

$$p(n_k^{1:C} \mid x_k, s_k, H_k) \propto \prod_{c=1}^{C} \exp(n_k^c \log(\lambda_k^c \delta_k) - \lambda_k^c \delta_k) \tag{3.4}$$

This quantity is the point of departure for applying discrete-time nonlinear filtering algorithms to point process observations.

3.3 The point process with generalized linear models (GLM)

This section overviews the generalized linear model (GLM) approach [7] used in this thesis to describe neuronal activity with point processes. The most pervasive approach to modeling spiking neural activity in the neuroscience literature is to relate stimuli and spiking through a Gaussian linear model [8]:

$$y = X\beta + \varepsilon \tag{3.5}$$

Here, $y = \left[n_1^c, n_2^c, ..., n_K^c\right]'$ is a column vector of binned spike times for one neuron, $\beta = \left[\beta_1, \beta_2, ..., \beta_R\right]'$ is a column vector of R parameters, X is a $K \times R$ matrix of covariate signals. Each column of X includes the discrete-time sequence of values realized by a one-dimensional covariate signal, such as an attentional state $\left[s_1 = 0, s_2 = 1, ..., s_K = 1\right]'$. The term $\varepsilon = \left[\varepsilon_1, \varepsilon_2, ..., \varepsilon_K\right]'$ is a column vector of independent, identical, zero mean Gaussian random variables with an unknown variance.

This approach typically uses δ of tens to hundreds of milliseconds that produce a large set of possible binned spike counts n_k, because n_k conditioned on the random variables corresponding to the k^{th} row of X are described as Gaussian under the model in (3.5). In contrast, the point process modeling approach allows for millisecond-resolution modeling.

Generalized linear models extend the linear Gaussian model in (3.5) to the exponential family of distributions, making it possible to relate covariates to responses that are not necessarily Gaussian. The exponential family includes distributions of the following form:

$$f(y \mid \beta) = \prod_{k=1}^{K} \exp\{T(y_k)C(\beta) + H(y_k) + D(\beta)\} \tag{3.6}$$

where y_k denotes the k^{th} element of y, and T, C, H, D are known functions. The GLM describes the linear combination of covariates as some function of μ, which refers to the mean of the distribution in (3.6) for Gaussian and Poisson distributions, but the standard parameter for the binomial distribution [7]:

$$g(\mu) = X\beta \tag{3.7}$$

The link function $g(\cdot)$ is any monotonic differentiable scalar function where $g(\mu) = \left[g(\mu_1), g(\mu_2), \ldots, g(\mu_K)\right]$. A specific choice of link function, the canonical link, results in a convex likelihood, which permits a standard gradient-ascent-based maximum likelihood parameter fitting procedure [7]. The canonical link function is obtained by equating $C(\beta) = X\beta$. The canonincal link function for the Poisson model with mean λ is $\log\left(\lambda\right) = X\beta$.

Parameter fitting for GLMs is commonly solved by iterative reweighted least-squares, a gradient-ascent approach which includes the Fisher scoring method and the Newton-Raphson method. The Matlab function `glmfit` automated this procedure for the maximum likelihood (ML) parameter fitting steps of our study on dorsal premotor cortex (Chapter 4).

To connect the GLM framework with the point process approach, we model the distribution of n_k as Poisson when conditioned on the covariate random variables corresponding to the k^{th} row of X. δ is chosen small (typically 1 ms) relative to changes in λ_k. The natural log is the canonical link function for the Poisson distribution. Accordingly, our generalized linear models are of the form:

$$\log \lambda = X\beta \tag{3.8}$$

where $\log \lambda = \left[\log(\lambda_1), \log(\lambda_2), ..., \log(\lambda_K)\right]'$.

3.4 Relative model quality with Akaike Information Criterion

With multiple models specified in the form given in (3.8), a procedure was desired to select the model that would best conform with the data *on average*. The Akaike Information Criterion (AIC) captures this notion, because it is derived as an approximation to the expected log likelihood $E_{g(Y)}\left[\log f\left(Y;\theta\right)\right]$, for the data-generating distribution $g\left(Y\right)$ and the model $f\left(Y;\theta\right)$ parameterized by θ.

The AIC can also be considered as an approximation to the part of the Kulback-Liebler (K-L) information $E_{g(Y)}\left[\log \frac{g(Y)}{f\left(Y;\theta\right)}\right]$ that differs between competing models. The expected log likelihood is identically this deciding term when two models are compared based on K-L distance to the data-generating distribution. See [9] for a derivation and [10] for a discussion of small-sample corrections and other properties of the AIC, including its equivalence to crossvalidation.

The formula for the AIC balances goodness-of-fit against model complexity. It credits a model for large data likelihood, and penalizes for the number of parameters in the model:

$$AIC = -2\log\left[\, p(n_1^{1:C}, n_2^{1:C}, ..., n_K^{1:C} \mid \hat{\beta}) \right] + 2R \tag{3.9}$$

where $\hat{\beta}$ is the ML estimate of β given the data, and $p(n_1^{1:C}, n_2^{1:C}, ..., n_K^{1:C} \mid \hat{\beta})$ is the data likelihood in (3.3) evaluated with ML parameters. The term R denotes the number of parameters, as with our GLM given in (3.8).

3.5 Absolute model quality with the time-rescaling theorem

Although AIC was used to assess relative model quality, we additionally required that the observed data was sufficiently typical under the minimum AIC model. The time-rescaling theorem, specific to point processes, provided statistics with confidence intervals to allow us to characterize the typicality of the deviation between a model and the spiking data.

The theorem can be stated as follows. Given spike times $0 < w_1 < w_2 < ... < w_m < T$ for a point process specified by $\lambda\left(t \mid H_t\right)$, define the random variables z_i for $i = 1, 2, ..., m-1$:

$$z_i = \int_{w_i}^{w_{i+1}} \lambda\left(t \mid H_t\right) dt \tag{3.10}$$

Then the z_i are independent, unit-mean exponentially distributed random variables.

The z_i represent the original interspike intervals (ISI), rescaled with respect to the conditional intensity function of the model. Statistics based on the time-rescaling theorem verify the extent to which the rescaled ISI are consistent with a set of independent and exponentially distributed random variables.

The z_i can be further transformed to independent uniform $\left[0,1\right]$ random variables u_i :

$$u_i = 1 - \exp(-z_i) \tag{3.11}$$

and then to independent standard Gaussian random variables g_i using the inverse CDF of the standard Gaussian, $\Phi^{-1}(u_i)$:

$$g_i = \Phi^{-1}(u_i) \tag{3.12}$$

where the standard Gaussian CDF is:

$$\Phi(x) = \frac{1}{\sqrt{2\pi}} \int_{-\infty}^{x} \exp\left(-\frac{u^2}{2}\right) du \tag{3.13}$$

For a proof, refer to [11].

The standard Kolmogorov-Smirnov test was used to compare the cumulative density function (CDF) of the u_i against that of the $\left[0,1\right]$ uniform distribution [11]. The statistic is the maximum deviation of the empirical CDF from the uniform CDF. In a cartesian plot of the empirical CDF as the y coordinate versus the uniform CDF as the x coordinate, the 95% (99%) confidence interval lines are:

$$y = x \pm \frac{1.36}{(m-1)^{1/2}} \qquad \left(y = x \pm \frac{1.63}{(m-1)^{1/2}} \right) \tag{3.14}$$

The one-lag autocorrelation a_m (as a function of the number of spikes m) was used as a preliminary test of independence. Here, the empirical autocorrelation is calculated on the standard Gaussian rescaled ISIs g_i because uncorrelated Gaussian random variables are independent:

$$a_m = \sum_{i=1}^{m-1} g_i \times g_{i+1} \tag{3.15}$$

Confidence intervals were calculated by Monte Carlo, where the distribution on a_m was assumed Gaussian, and a variance on the one-lag autocorrelation was estimated from multiple sets of simulated draws of m independent identically distributed standard Gaussian random variables.

3.6 Simulating spikes with the time-rescaling theorem

The converse of the time-rescaling theorem is also true [11]. This allows us to simulate point processes in discrete time from a model specification of the conditional intensity function λ_k by solving (3.10) for w_i given z_i. Spike simulation is employed in a type of model validation that is described further in the study on dorsal premotor cortex (Chapter 4). Additionally, we simulate spikes for off-line evaluation of neural prosthesis estimation algorithms (Chapters 5 and 6), where spiking activity is converted into an estimate of the user-intended device trajectory.

The procedure is described as follows. To generate the i^{th} simulated spike, draw a unit-mean exponential waiting time z_i. Step forward in discrete time steps k of 1 millisecond duration, summing the values of λ_k until a time step where the summed value equals or exceeds z_i. Generate a spike corresponding to that time step and reset the sum to zero. Repeat this procedure until the discrete-time point process has been simulated for the desired time interval.

3.7 Discrete-time point process filtering

In the discrete-time point process filtering problem, the posterior density of an underlying random process must be estimated from observations of a point process whose conditional intensity is a function of the underlying random process itself. In this thesis, we apply discrete-time point process filtering to understand the representation of target position in dorsal premotor cortex spiking (Chapter 4), and to estimate user-intended device states from spikes for neural prosthetic devices (Chapters 5, 6).

As mentioned in Section 3.2, the critical element for filtering point processes in discrete time is the discrete-time probability density in equation (3.4) of the ensemble spiking activity at time k conditioned on the history H_k, discrete state s_k, and continuous state x_k. With this quantity, any of a variety of nonlinear discrete-time filtering procedures can be adapted to point process filtering of an underlying Markov process. An exact discrete-time posterior density can be calculated in the case of a discrete-valued Markov process by applying a recursive form of Bayes' Rule, as employed in this thesis to study the representation of a discrete set of target positions in ensemble spiking activity recorded from dorsal premotor cortex (Chapter 4). The Gaussian approximation to the posterior density, also called the Laplace approximation, is used in this thesis (Chapters 5 and 6) for estimation of continuous-valued and hybrid (continuous and discrete valued) Markov processes. Other general nonlinear filtering techniques are available in the literature, including particle filters [12].

3.8 References

[1] D. J. Daley and D. Vere-Jones, *An introduction to the theory of point processes*, 2nd ed. New York: Springer, 2003.

[2] D. L. Snyder and M. I. Miller, *Random point processes in time and space*, 2nd ed. New York: Springer-Verlag, 1991.

[3] T. P. McGarty, *Stochastic systems and state estimation*. New York: Wiley, 1974.

[4] N. T. Twum-Danso, "Estimation, information, and neural signals," in *Division of Engineering and Applied Sciences*. Cambridge, MA: Harvard University, 1997, pp. 136.

[5] W. Truccolo, U. T. Eden, M. R. Fellows, J. P. Donoghue, and E. N. Brown, "A point process framework for relating neural spiking activity to spiking history, neural ensemble, and extrinsic covariate effects," *J Neurophysiol*, vol. 93, pp. 1074-89, 2005.

[6] U. T. Eden, L. M. Frank, R. Barbieri, V. Solo, and E. N. Brown, "Dynamic analysis of neural encoding by point process adaptive filtering," *Neural Comput*, vol. 16, pp. 971-98, 2004.

[7] P. McCullagh and J. A. Nelder, *Generalized Linear Models*, 2nd ed. New York: Chapman and Hall, 1989.

[8] F. Rieke, *Spikes : exploring the neural code*. Cambridge, Mass.: MIT Press, 1997.

[9] G. Kitagawa and W. Gersch, *Smoothness priors analysis of time series*. New York: Springer, 1996.

[10] K. P. Burnham and D. R. Anderson, *Model selection and multimodel inference : a practical information-theoretic approach*, 2nd ed. New York: Springer, 2002.

[11] E. N. Brown, R. Barbieri, V. Ventura, R. E. Kass, and L. M. Frank, "The time-rescaling theorem and its application to neural spike train data analysis," *Neural Comput*, vol. 14, pp. 325-46, 2002.

[12] A. Doucet, N. de Freitas, and G. Gordon, *Sequential Monte Carlo Methods in Practice*. New York: Springer-Verlag, 2001.

Chapter 4

Delay Period Target Representation in Dorsal Premotor Cortical Spiking

Premotor dorsal cortex (PMd) is believed to be involved in the representation of target position during the enforced delay period prior to visually-instructed reaching movements. In this chapter, we seek to understand the structure of the PMd response and demonstrate the extent to which aspects of the response contribute to target representation. Because of its extensive connectivity with other cortical and subcortical regions, it is unclear whether the PMd target representation can be adequately described with simple statistical models. Moreover, although various algorithms have demonstrated target decoding from PMd neurons, it remains an open question as to what extent various aspects of the PMd response contribute to the representation of targets.

In this study, we apply generalized linear models based on point process statistical methods to determine how elapsed time (time post-target-onset) and spiking history relate to the PMd response, and the extent to which these factors contribute to target representation. Action potentials are obtained from a population of 61 simultaneously recorded PMd neurons from a macaque monkey during a instructed-delay center out reaching task to one of 8 fixed target positions arranged evenly on a circle of 6 centimeters radius. PMd neurons span a diverse set of representations, of which more than 70% demonstrate both history and elapsed-time dependence. Log-linear point process statistical models adequately describe all target representations in 38 of the 61 recorded cells. Both history and elapsed-time dependencies contribute to faster, more efficient target position representations than the average firing rate that is typically summarized in tuning curves.

4.1 Introduction

The generation of voluntary movements involves multiple brain regions that coordinate goals with sensory input to determine muscle activation patterns. The functions of these brain regions are classically described in terms of planning and execution. Presented with an object to reach, a subject develops an estimate of the target position, and contracts musculature in concert with somatosensory and visual feedback to bring the hand to the target. The delayed reach experimental paradigm enforces movement phases that can be interpreted as planning and execution. Here, the subject is required to wait during a "delay period" for a cue before initiating movement to the target.

Premotor dorsal cortex (PMd) and other brain regions have been extensively studied with relation to movement planning. Lesions in PMd result in deficits of visually guided arm movements [1]. Specific features of the PMd delay period spiking response vary systematically with aspects of the movement or task: Average delay period firing rates change between trials that present different target locations [2]. A mean-normalized measure of across-trial variability decreases over the delay period, and covaries with reaction time [3]. Probability distributions have been used to describe the number of spikes (or other specific features of the response) in a delay period interval for each of a discrete set of targets. Several decoding methods have demonstrated target estimation from the delay period spiking response of an ensemble of PMd neurons with varying degrees of success [4, 5].

A quantitative theory of the role of PMd in movement control requires that we understand the whole delay period spiking response of PMd as well as specific features that describe it in part. How complex are theoretical models of PMd spiking that are consistent with empirically recorded activity? To what extent do various aspects of the PMd response contribute to rapid, efficient target representation? An adequate mathematical model of PMd spiking must capture the effects of a physical system governed by local neuronal properties and anatomical connections with numerous cortical and subcortical areas.

This chapter investigates these questions with a point process description of PMd delay period spiking activity. Using a generalized linear model framework, we attempt to capture the millisecond-by-millisecond spiking probability of a given neuron in terms of its dependence on elapsed time (time post-target-onset) and spiking history. We determine the adequacy of these models in relative and absolute terms, and the extent to which elapsed time and spiking history contribute to model quality and the speed and efficiency of target position representation with a fixed, discrete target set.

4.2 Methods

4.2.1 Behavioral task

One male macaque monkey (*Macaca mulatta)* was trained for 11 months to perform the instructed-delay center-out reaching task. The monkey sat in front of a horizontal display with its right arm resting in cushioned troughs of a 2-joint robotic arm (KINARM system [6]) under the display. The hand position was projected to a cursor on the display where target locations would also subsequently appear. The task consists of 3 time periods: hold, instructed-delay, and go (Figure 4.1). During the hold period (500 ms), a central target location appeared on a horizontal display over which the monkey was required to position the cursor. During the instructed delay period (variable length drawn uniformly from 1000 to 1500 ms), the target was displayed as a 1 cm x 1 cm square. Target locations were drawn uniformly from a fixed set of points spaced evenly on a circle of 6 centimeters radius about the central target. The monkey was required to continue maintaining its hand over the central target during this delay period. In the go period (maximum of 2 seconds allowed), the peripheral target flashed to instruct the monkey to initiate and complete a reaching movement to the target. A water drop reward was delivered when the cursor was held over the target for 500 milliseconds.

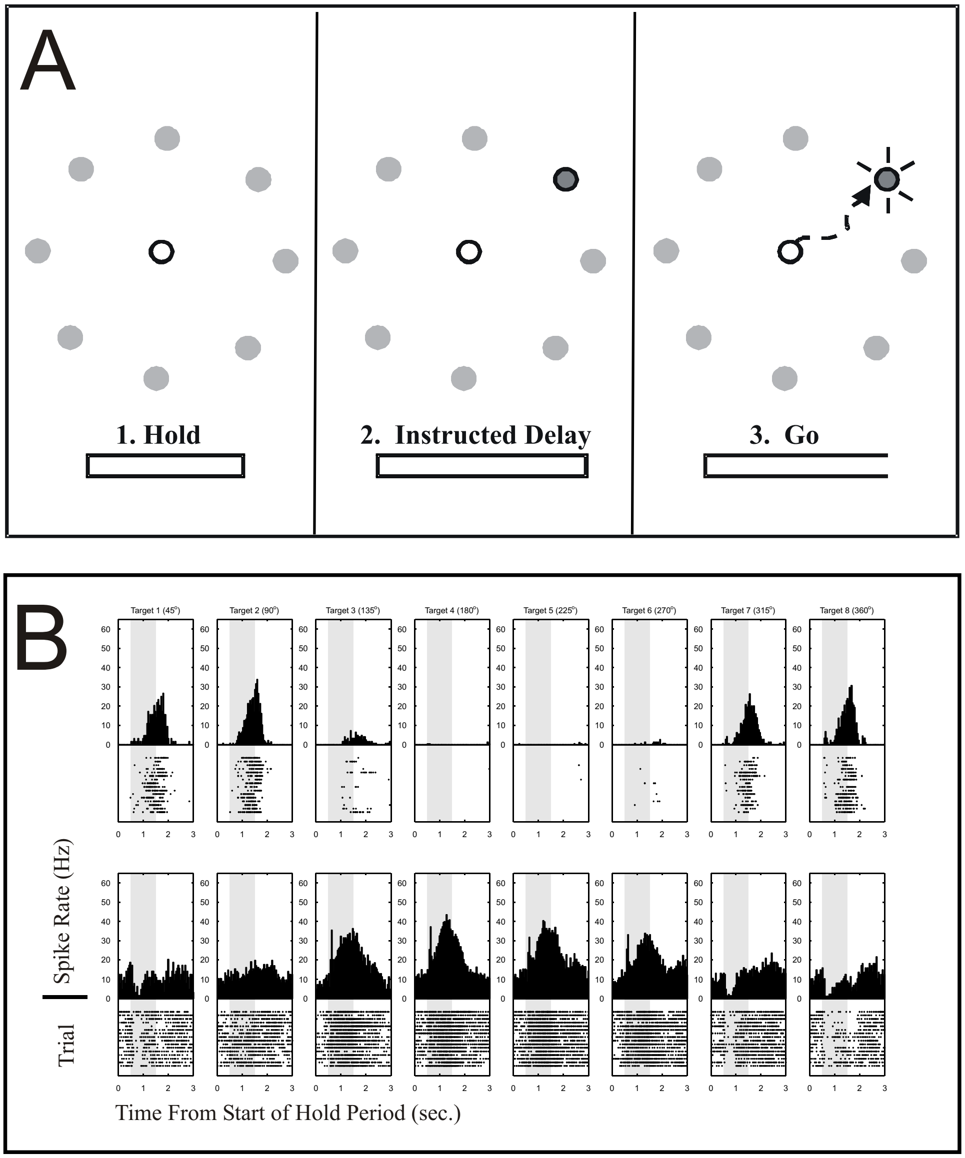

Figure 4.1. **(A)** The instructed-delay center-out task (CO) includes three periods: hold (500 ms), instructed delay (variable 1000 to 1500 ms), and go (variable, typically 500 to 1500 ms). See *Methods* for full description of the behavioral task. **(B)** Contrasting responses from two PMd neurons. Activity during the delay period can involve focal bursts of up to 20 spikes per second that are repeatable over multiple trials (upper row), or sustained firing with temporal dependence that approaches 50 spikes per second (lower row). Each row of panels correspond to the response of a different neuron to the eight target locations versus time from start of the hold period. The bottom half of each panel is a raster plot of spike times over multiple trials. The top half of each panel displays the corresponding average spike histogram, binned at non-overlapping 40 ms intervals.

4.2.2 Electrophysiology

Multiple single unit extracellular measurements were obtained from the caudal subdivision of dorsal premotor cortex (PMd) in the left hemisphere, with a chronically implanted array containing a 10x10 grid of electrodes (1 mm shaft lengths) spaced evenly over a 4 mm x 4 mm base (Cyberkinetics, Foxborough, MA). Signals were amplified with a gain of 150, sampled at 30 kHz per channel, and digitized at 14 bits per sample with a Cerebus acquisition system (Cyberkinetics, Foxborough, MA). Sampled waveform windows of 1.6 ms surrounding a threshold-exceeding signal were used to sort spikes with the Offline Sorter (Plexon, Dallas, TX).

4.2.3 Model forms and fitting

Delay period spiking responses of each neuron corresponding to each target position were described as a separate point process. The neurons were assumed independent in their ensemble response, and the quality of this assumption was explicitly tested (see *Absolute Model Quality* below).

A point process description of one neuron's spiking provides the instantaneous probability of firing as a function of elapsed time t and generally conditioned on other signals $x(t)$ including spiking history H_t, where $N(t)$ denotes the total number of spikes accumulated since target onset:

$$\lambda(t \mid x(t), H_t) = \lim_{\Delta \to 0} \frac{\Pr(N(t+\Delta) - N(t) = 1 \mid x(t), H_t)}{\Delta} \tag{4.1}$$

This is the continuous-time conditional intensity function. Each PMd point process model (one for each neuron/target pair) is expressed in discrete time steps δ of 1 millisecond, indexed by k. The value of the continuous-time conditional intensity function at timestep k is denoted by λ_k. This discrete-time conditional intensity may be a function of elapsed time (time post-target-onset) and the history of preceding spikes.

Elapsed time is described in terms of Δ_I second time intervals post-target-onset. The indicator function $I(i,k,\Delta_I)$ denotes whether or not a time step k falls into the i^{th} interval of elapsed time:

$$I(i,k,\Delta_I) = \begin{cases} 1 & if \quad (i-1)\Delta_I \le k\delta < i\Delta_I \\ 0 & otherwise \end{cases} \tag{4.2}$$

Elapsed time represents a surrogate for physical processes that determine firing probabilities in intervals of time after the target presentation, apart from history terms.

The discrete-time spiking history H_k of a particular 1 ms time step k includes both short-term and long-term history. The short-term history includes spike counts in each of the last ten milliseconds $(n_{k-1}, n_{k-2}, ..., n_{k-10})$. The long term history includes spike counts between 10 ms and 150 ms, binned at 10 ms intervals, denoted by $(n_{[k-10-1]:[k-20]}, n_{[k-20-1]:[k-30]}, ..., n_{[k-140-1]:[k-150]})$. Short term history is believed to be dominated by local physical interactions such as PMd neuronal cell membrane properties or local interneuron inhibition, whereas long term history is generally attributed to more distant reciprocal connections with conduction delay. These distinctions are not yet well established, and membrane properties alone may exert effects with histories that last 100 ms [7].

Spike counts in each 1 ms time step k were modeled with a Poisson distribution conditioned on history, elapsed time, and average firing rate parameters. The mean λ_k depended log-linearly on the elapsed time interval $I(i,k,\Delta_I)$ and spiking history H_k, with model parameters $\alpha_i, \beta_i, \gamma_i$:

Model	$\log(\lambda_k)$
1	α_1
2	$\alpha_1 + \beta_1 n_{k-1}$
3	$\sum_{i=1}^{\left\lceil \frac{1500ms}{\Delta_I=150ms} \right\rceil} \alpha_i I(i,k,\Delta_I = 150ms)$
4	$\sum_{i=1}^{\left\lceil \frac{1500ms}{\Delta_I=150ms} \right\rceil} \alpha_i I(i,k,\Delta_I = 150ms) + \beta_1 n_{k-1}$
5	$\sum_{i=1}^{\left\lceil \frac{1500ms}{\Delta_I=150ms} \right\rceil} \alpha_i I(i,k,\Delta_I = 150ms) + \sum_{i=1}^{10} \beta_i n_{k-i} + \sum_{i=1}^{14} \gamma_i n_{[k-10j-1]:[k-10j-10)]}$
6	$\sum_{i=1}^{\left\lceil \frac{1500ms}{\Delta_I=75ms} \right\rceil} \alpha_i I(i,k,\Delta_I = 75ms) + \sum_{i=1}^{10} \beta_i n_{k-i} + \sum_{i=1}^{14} \gamma_i n_{[k-10i-1]:[k-10i-10)]}$

This is the generalized-linear model (GLM) form that makes maximum likelihood parameter estimation easy: a convex optimization problem that can be solved with an iteratively reweighed least squares procedure. We employed the Matlab routine glmfit to perform this procedure. Models 5 and 6 were obtained by further reducing the corresponding models in the above table. Parameters were discarded that were not significant at the p=0.10 level based on hypothesis testing with the observed Fisher information calculated based on the given model's likelihood. While this model reduction procedure can result in overfitting [8], all models were subsequently compared using AIC and crossvalidation (see below).

4.2.4 Relative model quality: Akaike Information Criterion (AIC)

How important are elapsed time and spiking history versus average firing rate in describing the PMd delay period response? To address this question, we evaluated the relative quality of the six model types that captured various aspects of these factors using the Akaike Information Criterion (AIC).

See Chapter 3 for an introduction to AIC. The formula for the AIC using notation from this chapter is expressed as follows:

$$AIC = -2 \times \log\left[p\left(n_{0:T_r}^{c,d,r=1:R_{n,d}} \mid \hat{\theta}_{ML}^{n,d} \right) \right] + 2K \tag{4.3}$$

The first term contains the data likelihood, $p\left(n_{0:T_r}^{c,d,r=1:R_{c,d}} \mid \hat{\theta}_{ML}^{c,d} \right)$, evaluated at the maximum likelihood estimate $\hat{\theta}_{ML}^{c,d}$, where $n_{0:T_r}^{c,d,r=1:R_{c,d}}$ denotes all delay period one-millisecond time bins for neuron c and target d over all trials $r = 1:R_{c,d}$, where $R_{c,d}$ is the number of trials available for that neuron and target. The second term includes K, notation used to denote the number of parameters that compose the model. This term penalizes the model for complexity. The same Matlab function glmfit that was used to determine maximum likelihood parameter estimates, also returns the deviance with which to calculate the AIC.

4.2.5 Absolute model quality: time-rescaling statistics

Once minimum AIC models were chosen for each neuron/direction pair, we evaluated whether the model sufficiently described the data in an absolute sense. The time rescaling theorem and its associated statistics allow us to determine whether the empirically observed spiking data is sufficiently typical under the proposed point process model. A detailed mathematical description of this procedure was previously reported [10]. See Chapter 3 for an introduction to the time rescaling statistics.

4.2.6 Decoding: recursive estimation/classification of targets from ensemble PMd spiking

How important are elapsed time and history versus average firing rate in the quality of target representation among the spiking of an ensemble of PMd neurons? To address this question we applied a discrete time point process filter to provide target estimates that would theoretically approximate the minimum classification error assuming our selected models were correct. Because we assumed complete initial uncertainty about the target in each decoding trial, this approach was equivalent to choosing the maximum a posteriori (MAP) or the maximum likelihood (ML) target.

The filtering problem requires that we calculate the posterior density on the target position X given spike counts from a PMd ensemble of C neurons, including the first $k+1$ time bins of the delay period. The target position random variable can take on a particular value x that indicates one of the eight fixed target locations. The task draws targets at random, so that the initial probability of any given target is uniform:

$$p\left(X=x\right)=0.125 \tag{4.4}$$

Binned spike counts are updated with each new millisecond bin of ensemble observations using the following filtering equation:

$$p(X=x\mid n_{1:k+1}^{1:C})=\frac{\left[\prod_{c=1}^{C}(\lambda_{k+1,c,x})^{n_{k+1}^{c}}\exp(-\lambda_{k+1,c,x})\right]p(X=x\mid n_{1:k}^{1:C})}{R_{k+1}} \tag{4.5}$$

Here, $\lambda_{k+1,c,x}$ is the instantaneous probability of firing at time $k+1$, specified by the model for neuron c and target position x, and expressed in spikes per bin (here spikes per millisecond). This term captures history or elapsed-time dependence that is represented in the model. $n_{1:k}^{1:C}$ is the set of spikes counts from the first k one millisecond bins of the delay period.

Equation (4.5) simply represents an application of Bayes Rule. The expression in square brackets corresponds to a discrete time approximation of the point process observation density, namely $p\left(n_{k+1}^{1:C} \mid X = x, n_{1:k}^{1:C}; \theta_k\right)$. The normalization constant R_{k+1} includes $p(n_{k+1}^{1:C} \mid n_{1:k}^{1:C})$.

The mode of this posterior density (4.5) represents the target estimate that is most frequently correct:

$$\hat{x}_{k+1} = \arg\max_{x} \left(p(X = x \mid n_{1:k+1}^{1:C}) \right) \tag{4.6}$$

The number of trials for which this target estimate is correct at a given time interval k is reported as “Percent Correct (%)” (Figures 4.4 A,D, and G).

Our use of the point process filter explicitly states its assumptions through the statistical model. In contrast to previous PMd decoding approaches [4, 5], these assumptions are verified in the model quality steps (see previous sections). In an effort to reduce the effects of model mismatch, only minimum AIC models of neurons that passed the time rescaling statistics were included in the decoding analysis.

The filter allows millisecond-by-millisecond updates of the best target estimate over the duration of any given delay period. By switching between various model assumptions, we can demonstrate the extent to which those assumptions are important to target representation in PMd.

Model fitting and filtering were coordinated using three approaches. In leave-one-out crossvalidation, only the trial being decoded is not used in fitting model parameters. In leave-zero-out validation, all trials are used in fitting model parameters. In simulated validation, premovement PMd activity was generated using the time rescaling theorem from models that were fit using all trials, and decoded with the same models. See [10] for a description of spike simulation using the time rescaling theorem. The interpretation and comparison of these three approaches is explained in subsequent sections.

4.3 Results

We first studied the extent to which elapsed time and spiking history better describe delay period PMd activity than average firing rate alone. Six point process models were proposed (see Methods), each of which captured different aspects of average firing rate, elapsed time, and spiking history. After these models were fit to the data, the relative importance of these factors in predicting delay period activity could be assessed with the Akaike Information Criterion (AIC) (see Methods). This measure captures the notion that models that generalize well to unseen data are careful to balance goodness-of-fit with simplicity.

The AIC analysis is summarized in a bar graph (Figure 4.4.2A). These results indicate that elapsed time and spiking history together describe PMd delay period responses better than any factor alone for more than 70 percent of neuron/direction pairs. Consistent with the contribution of elapsed time, we would expect that the presentation of a target in the context of the delayed reach training regimen is associated with physical processes that preserve a dynamic temporal structure over multiple trials. In contrast, roughly 20% of neuron/direction pairs were consistent with models that would describe a PMd response dictated by physical processes that retain a static structure over the delay period.

History terms distributed throughout the last 150 milliseconds were represented in the minimum AIC models (Figure 4.2C), and their contributions tended to be inhibitory (not shown). Taken together, this data suggests that both local and distant neuronal processes contribute to the PMd response during the delay period. Cell membrane properties and inhibitory interneuron connections might predominate the short term history, while more distant recurrently connecting pathways [11, 12] to parietal cortex, frontal cortex, basal

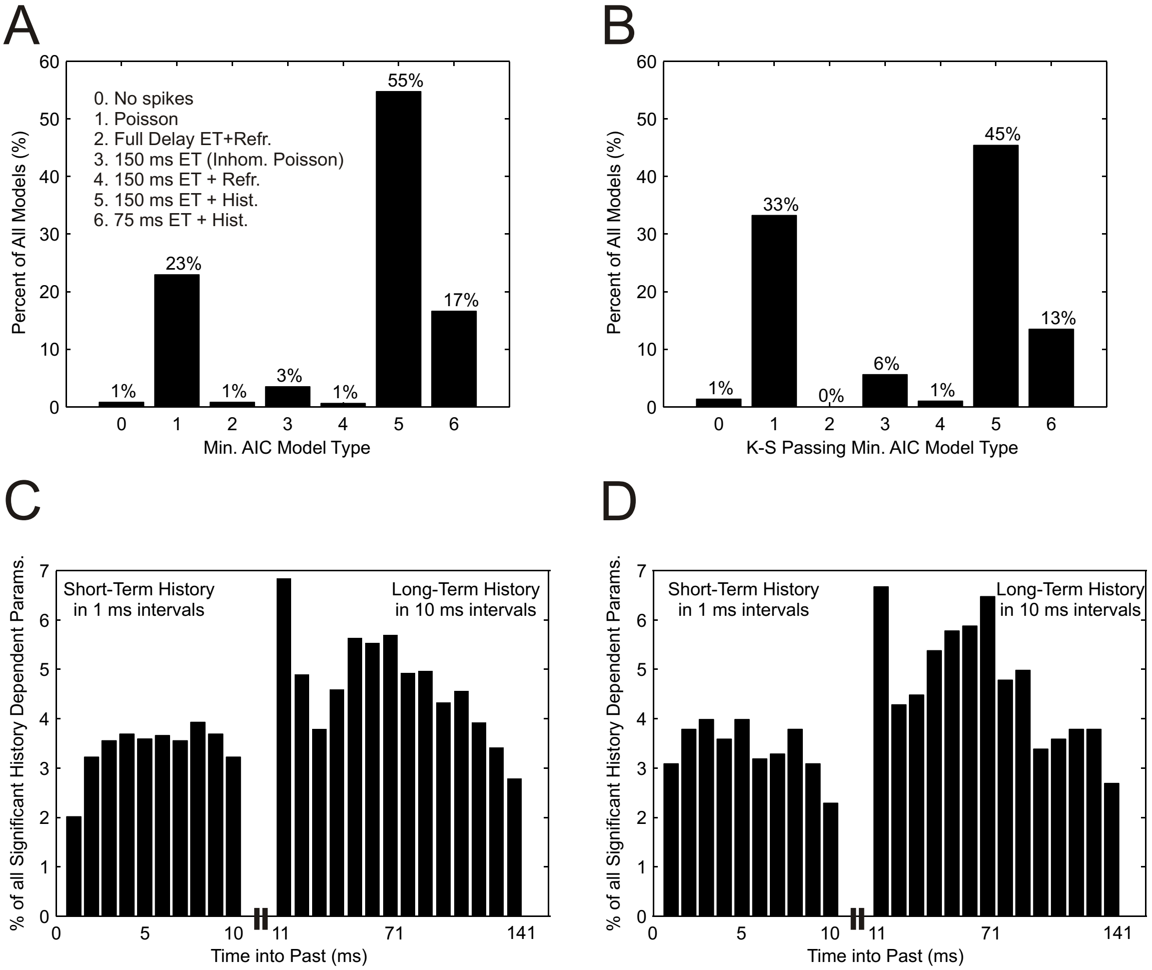

Figure 4.2. Models are fit across all trials of every neuron, separately for each target. The Akaike Information Criterion (AIC) balances goodness-of-fit against generalizability to assess model quality. **(A)** Percentage of all models that are best described by each model type. Slightly more than 70 percent of PMd responses across 61 neurons and 8 directions were better modeled with history beyond absolute refractory periods than with simpler dependencies indicated in the figure legend. Elapsed time (ET) models of varying resolution (Full Delay, 150 ms, 75 ms) and other model types are explained under Methods. **(B)** Same as in (A), but computed among models that correspond to neurons with satisfactory models for all 8 directions based on the K-S and autocorrelation tests (Figure 2). **(C)** Distribution of history intervals that contributed to the minimum-AIC models described in (A), including short-term history that extends backwards in time from 1 to 10 ms in 1 ms intervals, and long term history that further extends from 11 to 150 ms in 10 ms intervals. **(D)** Same as in (C), but computed among models that correspond to neurons with satisfactory models for all 8 directions based on the K-S and autocorrelation tests (Figure 2). This broad history dependence may arise from properties of the individual neuron, recurrent connections of the associated network, and temporal correlations in the visually presented stimulus.

ganglia, and cerebellum might contribute to long term history. This supports the idea that a network of neurons distributed throughout cortical and subcortical regions cooperate in determining activity that specifically precedes the movement and follows the visually-directed cue, but that local PMd properties also contribute to history dependence. Indeed, delay period activity distinct from activity in other movement phases has been observed in posterior parietal cortex [13], frontal cortex [14], and the subthalamic nucleus [15].

Could PMd responses, determined by both local and distant physical processes, be adequately described by these relatively simple models? The time rescaling theorem and related statistics (see Methods) allowed us to evaluate our models in this absolute sense. We plot sample results from the K-S statistic and one-lag autocorrelation for illustration (Figures 4.3A and B). The threshold for passing the K-S test can be varied to include more neurons that have satisfactory models for every target position (Figure 4.3C). The 99 percent confidence interval corresponds to the vertical dashed line, where 40 of the 61 PMd neurons have adequate models in all directions. Of these 40 neurons, 38 additionally passed the one-lag autocorrelation test. Consequently, just over 60 percent of the neurons studied could be adequately described (in the sense of time rescaling statistics) by these model classes. The model classes among this passing subset (Figure 4.2B) tend to include more Poisson models than the original subset (Figure 4.2A). Short and long term history are still represented (Figure 4.2C).

How important are average firing rate, elapsed time and spiking history in the representation of targets? By capturing how quickly and efficiently targets could be decoded when each of these factors were incorporated, our analysis characterized the extent of advantage that downstream neural networks or prosthetic algorithms would acquire by tuning their responses to those factors.

Results of leave-one-out crossvalidation (Figures 4.4 A-C), leave-zero-out validation (Figures 4.4 D-F), and simulated validation (Figures 4.4 G-I) were summarized. See Methods for definitions. In all decoding cases, the minimum AIC filter provides better results than inhomogeneous Poisson (elapsed time) or Poisson models (Figures 4.4 A,D,

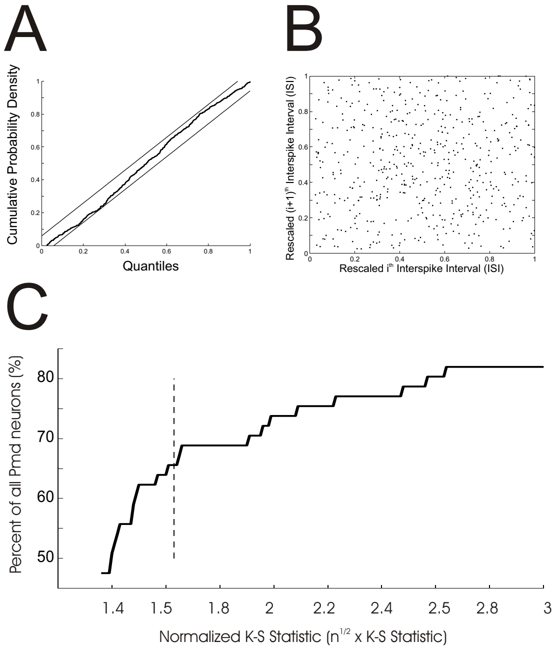

Figure 4.3. Use of the time-rescaling theorem to evaluate the minimum AIC models determined in Figure 2C. The time-rescaling theorem states that the correct model of spiking activity will proportion the interspike intervals (ISIs) of a spike train into series of independent, exponentially distributed random variables of mean 1. **(A)** The K-S plot verifies that rescaled ISIs are exponentially distributed. Spikes generated from the Min AIC model of one example neuron produce empirical cumulative probability density functions that fall within the solid lines 99 percent of the time. **(B)** The one-delay-autocorrelation test checks that neighboring interspike intervals are independent, as depicted pictorially with this same model from the uniform scatter of ISIs. **(C)** More neurons pass the K-S test when the normalized K-S statistic is increased. At the normalized K-S statistic corresponding to 99 percent confidence intervals (vertical dashed line), 40 out of 61 (approximately 65%) of the neurons pass the K-S test, of which 38 neurons additionally pass the one-delay-autocorrelation test with a confidence interval of 3 standard deviations.

G). Decisions that are made on the scale of reaction times (200 ms) make more efficient use of neurons when both elapsed time and history are incorporated (Figures 4.4 B,E,H). Performance improvements appear to diminish substantially as the population size approaches 40 neurons. This effect is likely an artifact of the analysis: because neurons are drawn with replacement from a pool of 38 neurons, fewer independent observations are introduced as the tested ensemble size grows. The simulated validation (Figure 4.4 H) introduces independent responses, but from the same pool of 38 tuning curves (spiking models). Similarly, projected estimates of performance reported in previous studies [4, 5, 16] are expected to under or overestimate the number of neurons needed to achieve a particular performance level if the observed set of neurons have a different distribution of tuning curves than the general population. Reliable decisions can generally be made more rapidly by considering elapsed time and history structure in addition to average firing rate (Figures 4.4 C,F,I).

Why aren't these decoding results perfect? The simulated validation (Figures 4.4 G,H,I) shows that even when a filter is perfectly matched to spiking activity, decoding errors cannot be eliminated entirely during the delay period because the spiking response is intrinsically noisy. However, the error rates can be brought down both by increasing the numbers of neurons (Figure 4.4H) and by waiting longer before a decision is made (Figure 4.4G). In practice decoding performance is worse than would be suggested by the simulated analysis. The concepts of overfitting and underfitting capture this notion. In overfitting, the model is unable to adequately generalize because it captures features of the noise specific to the training data set. The difference in performance between leave-zero-out validation (Figure 4.4D) and leave-one-out crossvalidation (Figure 4.4A) suggests that the minimum AIC and inhomogeneous Poisson models suffer from overfitting to a greater extent than the Poisson model. In underfitting, the model fails to generalize well because it is unable to capture the correct intrinsic structure in the PMd response. The difference in performance between leave-zero-out and simulated validation indicates that the Poisson model suffers in part from simplicity: performance degradation from poor goodness-of-fit (model mismatch) is indicative of underfitting.

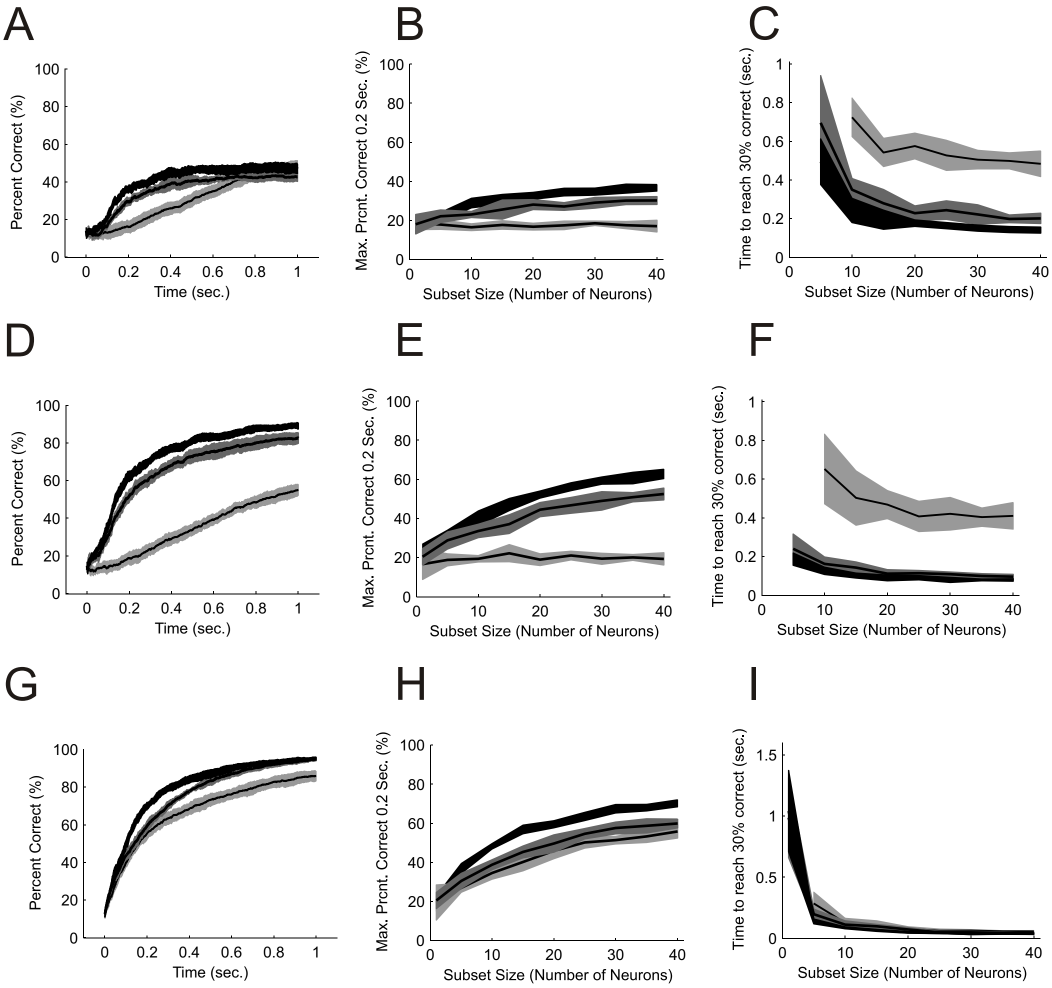

Figure 4.4. Point process filter decoding analysis. Three model classes were considered for decoding, including the minimum AIC model (model 6, black), an inhomogeneous Poisson model (model 3, dark gray), and a Poisson model (model 1, light gray). Three types of analyses are displayed: **(A,B,C)** Leave-one-out crossvalidated empirical decoding performance. **(D,E,F)** Leave-zero-out empirical decoding performance, and **(G,H,I)** Simulated decoding performance. Three types of graphs are used to summarize the results: **(A,D,G)** The percentage of trials classified correctly is plotted against time for an ensemble of 40 neurons. **(B,E,H)** The largest percent correct achieved by each model class in the first 500 ms post-target-onset is plotted against ensemble size. **(C,F,I)** The time post-target-onset required to reach 30% correct is plotted against ensemble size. Shaded lines in all graphs indicate 2 standard deviations above and below a mean percent correct, calculated from the variance of 10 simulation results, each of which runs at least 500 decoding trials.

4.4 Discussion

The modeling analysis presented in this work suggests that for the majority of PMd neurons, the incorporation of elapsed time and history better describes delay period activity than the standard average firing rate tuning curve alone. The delay period response of many PMd neurons can be adequately described (in the sense of time-rescaling statistics) by these relatively simple models despite extensive local and distant recurrent connections. The heterogeneity of physical phenomena associated with PMd is reflected in a broad based history dependence over 150 ms.

The decoding analysis highlights that better target representations can be achieved in at least three ways: adjusting the neural code, growing the population of neurons in the ensemble, and waiting longer times before decisions are made. Often we are unable to wait longer to generate reliable representations, such as when shooting a basketball in a game, or playing a rapid piano piece. Recruitment of larger population sizes and adjusted neural codes are two possible ways in which experts might improve their performance in the face of time constraints.

Our simulated validation shows that even Poisson neural codes with realistic firing rates and tuning curves are capable of target representation that is far superior to what would be inferred from leave-one-out crossvalidation. The spiking of most PMd neurons is better described by elapsed time and history dependence, but a minority of ensemble subsets that are sufficiently decoupled from recurrent connections might still contribute to target representation in a Poisson-like fashion.

Although we have characterized the relative importance of various factors in contributing to high quality target representation in PMd, the best downstream neural systems for decoding would need to consider robustness, energy consumption, and other costs in addition to expected classification performance. As a result, the physical instantiation of an optimized *in vivo* decoding algorithm could be very different from what is considered optimal with respect to minimum classification error.

The minimum AIC models in this report present better generalizability than standard PMd models and achieve adequate goodness-of-fit based on the time rescaling statistics. However, the statistical description of PMd delay period activity is not complete. Subsequent work must achieve stronger generalizability in the statistical description of PMd. The next generation of statistical models should begin to consider known physical constraints. Techniques like diffusion tensor imaging may be able to provide estimates of conduction delays related to recurrent connections to the specific PMd neurons being investigated in any given study. A physically constrained approach may allow for stronger generalization as well as statements about PMd target representation that can be interpreted more directly in the context of the neural architecture.

4.5 References

[1] U. Halsband and R. E. Passingham, "Premotor cortex and the conditions for movement in monkeys (Macaca fascicularis)," *Behav Brain Res*, vol. 18, pp. 269-77, 1985.

[2] M. Weinrich and S. P. Wise, "The premotor cortex of the monkey," *J Neurosci*, vol. 2, pp. 1329-45, 1982.

[3] M. M. Churchland, B. M. Yu, S. I. Ryu, G. Santhanam, and K. V. Shenoy, "Neural variability in premotor cortex provides a signature of motor preparation," *J Neurosci*, vol. 26, pp. 3697-712, 2006.

[4] N. Hatsopoulos, J. Joshi, and J. G. O'Leary, "Decoding continuous and discrete motor behaviors using motor and premotor cortical ensembles," *J Neurophysiol*, vol. 92, pp. 1165-74, 2004.

[5] G. Santhanam, S. I. Ryu, B. M. Yu, A. Afshar, and K. V. Shenoy, "A high-performance brain-computer interface," *Nature*, vol. 442, pp. 195-8, 2006.

[6] S. H. Scott, "Apparatus for measuring and perturbing shoulder and elbow joint positions and torques during reaching," *J Neurosci Methods*, vol. 89, pp. 119-27, 1999.

[7] C. C. McIntyre, A. G. Richardson, and W. M. Grill, "Modeling the excitability of mammalian nerve fibers: influence of afterpotentials on the recovery cycle," *J Neurophysiol*, vol. 87, pp. 995-1006, 2002.

[8] K. P. Burnham and D. R. Anderson, *Model selection and multimodel inference : a practical information-theoretic approach*, 2nd ed. New York: Springer, 2002.

[9] G. Kitagawa and W. Gersch, *Smoothness priors analysis of time series*. New York: Springer, 1996.

[10] E. N. Brown, R. Barbieri, V. Ventura, R. E. Kass, and L. M. Frank, "The time-rescaling theorem and its application to neural spike train data analysis," *Neural Comput*, vol. 14, pp. 325-46, 2002.

[11] J. Krakauer and C. Ghez, "Voluntary Movement," in *Principles of Neural Science*, E. R. Kandel, J. H. Schwartz, and T. M. Jessell, Eds., 4th ed. New York: McGraw Hill, 2000, pp. 756-779.

[12] R. P. Dum and P. L. Strick, "Motor areas in the frontal lobe of the primate," *Physiol Behav*, vol. 77, pp. 677-82, 2002.

[13] R. A. Andersen and C. A. Buneo, "Intentional Maps in Posterior Parietal Cortex," *Annual Review of Neuroscience*, vol. 25, pp. 189-220, 2002.

[14] J. D. Schall, "Neural basis of deciding, choosing and acting," *Nat Rev Neurosci*, vol. 2, pp. 33-42, 2001.

[15] Z. M. Williams, J. S. Neimat, G. R. Cosgrove, and E. N. Eskandar, "Timing and direction selectivity of subthalamic and pallidal neurons in patients with Parkinson disease," *Exp Brain Res*, vol. 162, pp. 407-16, 2005.

[16] J. Wessberg, C. R. Stambaugh, J. D. Kralik, P. D. Beck, M. Laubach, J. K. Chapin, J. Kim, S. J. Biggs, M. A. Srinivasan, and M. A. Nicolelis, "Real-time prediction of hand trajectory by ensembles of cortical neurons in primates," *Nature*, vol. 408, pp. 361-5, 2000.

Chapter 5

A State Space Analysis for Reconstruction of Goal-Directed Movements Using Neural Signals[1]

The execution of reaching movements involves the coordinated activity of multiple brain regions that relate variously to the desired target and a path of arm states to achieve that target. These arm states may represent positions, velocities, torques, or other quantities. Estimation has been previously applied to neural activity in reconstructing target separately from path. However, target and path are not independent. Because arm movements are limited by finite muscle contractility, knowledge of the target constrains the path of states that leads to the target. In this chapter, we derive and illustrate a state equation to capture this basic dependency between target and path. The solution is described for discrete-time linear systems and Gaussian increments with known target arrival time. The resulting analysis enables the use of estimation to study how brain regions that relate variously to target and path, together specify a trajectory. The corresponding reconstruction procedure may also be useful in brain-driven prosthetic devices to generate control signals for goal-directed movements.

---

[1] L. Srinivasan, U.T. Eden, A.S. Willsky, E.N. Brown. *Neural Computation*, vol. 18, no. 10, October 2006.

5.1 Introduction

An arm reach can be described by a number of factors, including the desired hand target and the duration of the movement. We reach when moving to pick up the telephone or to lift a glass of water. The duration of a reach can be specified explicitly (Todorov & Jordan, 2002) or emerge implicitly from additional constraints such as target accuracy (Harris & Wolpert, 1998). Arm kinematics and dynamics during reaching motion have been studied through their correlation with neural activity in related brain regions, including motor cortex (Moran & Schwartz, 1999), posterior parietal cortex (Andersen & Buneo, 2002), basal ganglia (Turner & Anderson, 1997), and cerebellum (Greger, Norris, & Thach, 2003). Separate studies have developed control models to describe the observed movements without regard to neural activity (Todorov, 2004a). An emerging area of interest is the fusion of these two approaches, to evaluate neural activity in terms of the control of arm movement to target locations (Todorov, 2000; Kemere & Meng, 2005). While several brain areas have been implicated separately in the planning and execution of reaches, further study is necessary to elucidate how these regions coordinate their electrical activity to achieve the muscle activation required for reaching. In this chapter, we develop state-space estimation to provide a unified framework to evaluate reach planning and execution related activity.

Primate electrophysiology during reaching movements has focused on primary motor cortex (M1) and posterior parietal cortex, regions that represent elements of path and target, respectively. Lesion studies previously identified M1 with motor execution (Nudo, Wise, SiFuentes, & Milliken, 1996) and PPC with movement planning (Geschwind & Damasio, 1985). Several experiments have characterized the relationship between M1 neuronal activity, arm positions and velocities (Georgopoulos, Kalaska, Caminiti, & Massey, 1982; Schwartz, 1992; Moran & Schwartz, 1999; Paninski, Fellows, Hatsopoulos, & Donoghue, 2004), and forces (Georgopoulos, Ashe, Smyrnis, & Taira, 1992; Taira, Boline, Smyrnis, Georgopoulos, & Ashe, 1995; Li, Padoa-Schioppa, & Bizzi, 2001). PPC is presently described as relating broadly to the formation of intent, and specifically to the transformation of sensory cues into movement goals (Andersen &

Buneo, 2002). More recent experiments are beginning to elucidate the role of premotor cortical areas in motion planning and execution (Schwartz, Moran, & Reina, 2004), including interactions with PPC (Wise, Boussaoud, Johnson & Caminiti, 1997). Explicit regression analyses have also been performed to relate motor cortical activity to features of both target and path (Fu, Suarez, & Ebner, 1993; Ashe & Georgopoulos, 1994).

In parallel, theoretical models for the planning and execution of reaches have developed to include different concepts in control engineering and robotics. A common starting point is the state equation, a differential equation that describes how the arm moves due to passive sources like joint tension, and user controlled forces such as muscle activation. The state equation is used to prescribe a path or a sequence of forces to complete the reach based on the minimization of some cost function that depends on variables such as energy, accuracy, or time. Many reach models specify control sequences computed prior to movement that assume a noise-free state equation and perfect observations of arm state (Hogan, 1984; Uno, Kawato & Suzuki, 1989; Nakano et al., 1999). The execution of trajectories planned by these models can be envisioned in the face of random perturbations by equilibrium-point control, where each prescribed point in the trajectory is sequentially made steady with arm tension. Recently, reach models have been developed that explicitly account for noisy dynamics and observations (Harris & Wolpert, 1998; Todorov, 2004b). Based on stochastic optimal control theory, the most recent arm models (Todorov & Jordan, 2002; Todorov, 2004b) choose control forces based on estimates of path history and cost-to-go, the price associated with various ways of completing the reach. A general review of control-based models is provided in Todorov, 2004a.

Estimation has been used to relate neural activity with aspects of free arm movements (Georgopoulos, Kettner, & Schwartz, 1988; Paninski, Fellows, Hatsopoulos, & Donoghue, 2004). Alternate models of neural response in a specific brain region can be compared by mean squared error (MSE). Reconstruction of a measured parameter is one way to characterize neural activity in a brain region. Learning rates can be related explicitly and simultaneously to continuous and discrete behavioral responses using an estimation framework (Smith et al., 2004). Mutual information is a related alternative that has been prevalent in the characterization of neural responses to sensory stimuli (Warland, Reinagel, & Meister, 1997). Both mean squared error (MSE) and conditional entropy (calculated in determining mutual information) are functions of the uncertainty in an estimate given neural observations, and mean squared error (MSE) rises with conditional entropy for Gaussian distributions. These two methods were recently coupled to calculate the conditional entropy associated with recursively-computed estimates on neural data (Barbieri et al., 2004).

Estimation algorithms presently form the interface between brain and machine in the control of neural prosthetics, bearing directly on the clinical treatment of patients with motor deficits. Prototype systems have employed either estimation of free arm movement (Carmena, et al., 2003; Taylor, Tillery, & Schwartz, 2002; Wu, Shaikhouni, Donoghue, & Black, 2004), or target location (Musallam, Corneil, Greger, Scherberger, & Andersen, 2004; Santhanam, Ryu, Yu, Afshar, & Shenoy, 2005). Most recently, several estimation procedures were proposed to combine these two approaches and specifically facilitate reaching movements for brain-controlled prosthetics (Srinivasan, Eden, Willsky, & Brown, 2005; Cowan & Taylor, 2005; Yu, Santhanam, Ryu, & Shenoy, 2005; Kemere & Meng, 2005).

Two probability densities are used implicitly in estimation. The first density describes the probability of neural activity conditioned on relevant covariates like stimulus intensities or kinematic variables. This density arises through the observation equation in estimation, and as an explicit function in information theoretic measurements. The second density describes the interdependence of the relevant covariates before any neural activity is recorded. This density arises through the state equation in estimation and as a prior on stimulus values in the information-theoretic characterization of sensory neurons. In experiments that calculate mutual information between neural activity and independent stimulus parameters, this second probability density is commonly chosen to be uniform. In the study of reaching movements, the complete prior density on target and path variables cannot be uniform because the target and the path state at all times in the trajectory are dependent. A state equation naturally expresses these constraints, and serves as a point of departure for analysis based on estimation.

In this chapter, we develop a discrete-time state equation that relates target state and path states under weak assumptions about a reach. Specifically, the result represents the extension of the linear state-space description of free arm movement with no additional constraints. The states of the target or path refer to any vector of measurements of the arm at a particular point in time, such as joint torque, joint angle, hand velocity, and elbow position. This method supports arbitrary order, time-varying linear difference equations, which can be used to approximate more complicated state equation dynamics. The approach is based on the continuous-time results by Castanon, Levy, & Willsky, 1985 in surveillance theory, and draws on the discrete time derivation of a backwards Markov process described by Verghese & Kailath, 1979. Unlike existing theoretical models of reaching movement, we do not begin with an assumed control model or employ cost functions to constrain a motion to target. The resulting reach state equation is a probabilistic description of all paths of a particular temporal duration that start and end at states that are specified with uncertainty.

We first develop a form of the reach state equation that incorporates one prescient observation on the target state. We then extend this result to describe an augmented state equation that includes the target state itself. This augmented state equation supports recursive estimates of path and target that fully integrate ongoing neural observations of path and target. Sample trajectories from the reach state equation are shown. We then demonstrate the estimation of reaching movements by incorporating the reach state equation into a point process filter (Eden, Frank, Barbieri, Solo, & Brown, 2004). We conclude by discussing the applicability of our approach to the study of motion planning and execution, as well as to the control of neural prosthetics.

5.2 Theory

5.2.1 State Equation to Support Observations of Target Before Movement

The objective in this section is to construct a state equation for reaching motions that combines one observation of the target before movement with a general linear state equation for free arm movement. The resulting state equation enables estimation of the arm path that is informed by concurrent observations and one target-predictive observation, such as neural activity from brain regions related to movement execution and target planning respectively. We begin with definitions and proceed with the derivation.

A reach of duration T time steps is defined as a sequence of vector random variables $(x_0, x_1, ..., x_T)$ called a trajectory. The state variable x_t represents any relevant aspects of the arm at time sample t, such as position, velocity, and joint torque. The target x_T is the final state in the trajectory. While we conventionally think of a target as a resting position for the arm, x_T more generally represents any condition on the arm at time T, such as movement drawn from a particular probability distribution of velocities.

For simplicity, we restrict our trajectory to be a Gauss-Markov process. This means that the probability density on the trajectory $p(x_0, x_1, ..., x_T)$ is jointly Gaussian and that the probability density of the state at time t conditioned on all previous states $p(x_t \mid x_{t-1}, x_{t-2}, ..., x_0)$ equals $p(x_t \mid x_{t-1})$, the state transition density. Although more general probability densities might be considered, these special restrictions are sufficient to allow for history dependency of arbitrary length. This is commonly accomplished by including the state at previous points in time in an augmented state vector (Kailath, Sayed, & Hassibi, 2000). Figure 5.1A is a schematic representation of the trajectory and the target observation, emphasizing that the prescient observation of target y_T is related to the trajectory states x_t only through the target state x_T.

The conditional densities of the Gauss-Markov model can alternatively be specified with observation and state equations. For a free arm movement, the state transition density $p\left(x_t \mid x_{t-1}\right)$ can be described by a generic linear time-varying multidimensional state equation,

$$x_t = A_t x_{t\text{-}1} + w_t \tag{5.1}$$

where the stochastic increment w_t is a zero-mean Gaussian random variable with $E\left[w_t w_\tau^{'}\right] = Q_t \delta_{t-\tau}$. The initial position x_0 is Gaussian distributed with mean m_0 and covariance Π_0. The prescient observation y_T of the target state x_T is corrupted by independent zero-mean Gaussian noise v_T with covariance Π_T that denotes the uncertainty in target position:

$$y_T = x_T + v_T \tag{5.2}$$

The state equation coupled with this prescient observation is described schematically in Figure 5.1B.

Restated, our objective is to represent the free movement state equation together with the prescient observation on target, as a Gauss-Markov model on an equivalent set of trajectory states x_t conditioned on y_T for $t = 0,1,...,T$. The consequent reach state equation is of the form:

$$x_t = A_t x_{t\text{-}1} + u_t + \varepsilon_t \tag{5.3}$$

where u_t is a drift term corresponding to the expected value of $w_t \mid x_{t-1}, y_T$, and the ε_t are a new set of independent, zero-mean Gaussian increments whose covariances correspond to that of $w_t \mid x_{t-1}, y_T$. This reach state equation generates a new probability density on the trajectory of states that corresponds to the probability of the original states conditioned on the prescient observation, $p(x_0,...,x_T \mid y_T)$.

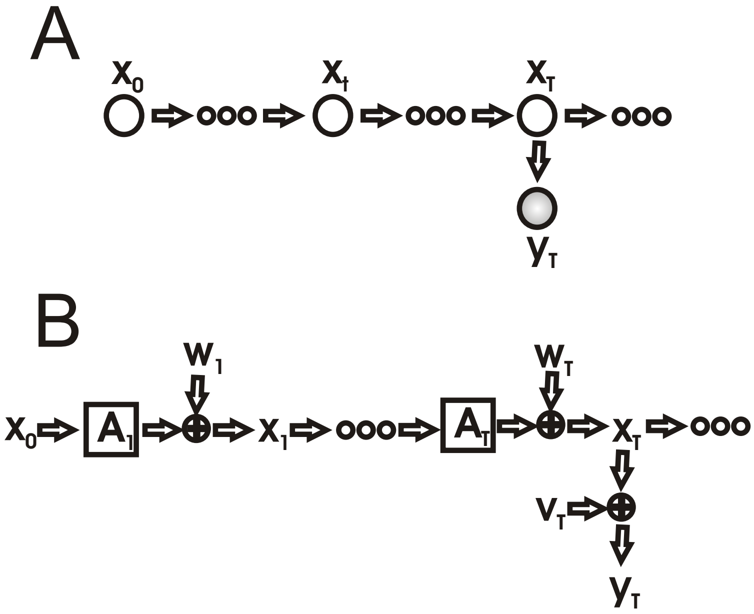

Figure 5.1. Alternate representations of a reaching trajectory and one observation on target. In the Markov model **(A)**, circles represent the state of the arm at various times, and the arrangement of directed arrows indicates that the state of the arm at time t is independent of all previous states conditioned on knowledge of the state at time t-1. Accordingly, the only state pointing to y_T, the prescient observation of target, is the target state x_T itself. In the system diagram **(B)**, the specific evolution of the arm movement is described. Consistent with the state equation, the arm state x_{t-1} evolves to the next state in time x_t through the system matrix A_t, with additive noise w_t that represents additional uncertainty in aspects of the arm movement that are not explained by the system matrix. The diagram also specifies that the observation y_T of the target state x_T is corrupted by additive noise v_T.

To derive this reach state equation, we calculate the state transition probability density $p(x_t \mid x_{t\text{-}1}, y_T)$. Because w_t is the only stochastic component of the original state equation, the new state transition density is specified by $p(w_t \mid x_{t-1}, y_T)$. To compute this distribution, we use the conditional density formula for jointly Gaussian random variables on the joint density $p(w_t, y_T \mid x_{t\text{-}1})$. The resulting distribution is itself Gaussian with mean and variance given by:

$$\begin{aligned} u_t &= E[w_t \mid x_{t-1}, y_T] \\ &= E[w_t \mid x_{t-1}] + \mathrm{cov}(w_t, y_T \mid x_{t-1})\,\mathrm{cov}^{-1}(y_T, y_T \mid x_{t-1})(y_T - E[y_T \mid x_{t-1}]) \end{aligned} \tag{5.4}$$

$$\begin{aligned} \tilde{Q}_t &= \mathrm{cov}(w_t \mid x_{t-1}, y_T) \\ &= \mathrm{cov}(w_t \mid x_{t-1}) - \mathrm{cov}(w_t, y_T \mid x_{t-1})\,\mathrm{cov}^{-1}(y_T \mid x_{t-1})\,\mathrm{cov}'(w_t, y_T \mid x_{t-1}) \end{aligned} \tag{5.5}$$

The mean u_t corresponds identically to the linear least squares estimate of $w_t \mid x_{t-1}, y_T$ and the variance $\tilde{Q}$ equals the uncertainty in this estimate.

The covariance terms in equations (5.4) and (5.5) can be computed from the following equation that relates w_t to y_T given $x_{t\text{-}1}$,

$$y_T = \phi(T, t-1)x_{t-1} + \sum_{i=t}^{T} \phi(T, i)w_i + v_T \tag{5.6}$$

where $\phi(t, s)$ denotes the state transition matrix that advances the state at time s to time t,

$$\phi(t, s) = \begin{cases} \displaystyle\prod_{i=1+\min(t,s)}^{\max(t,s)} A_i^{sign(t-s)}, t \neq s \\ \mathrm{I}, t = s \end{cases} \tag{5.7}$$

The covariance terms are accordingly given by

$$\mathrm{cov}(w_t \mid x_{t-1}) = Q_t \tag{5.8}$$

$$\mathrm{cov}(w_t, y_T \mid x_{t-1}) = Q_t \phi'(T,t) \tag{5.9}$$

$$\mathrm{cov}(y_T, y_T \mid x_{t-1}) = \Pi_T + \sum_{i=t}^{T} \phi(T,i) Q_i \phi'(T,i) \tag{5.10}$$

For notational convenience, define the following quantity:

$$\Pi(t,T) = \phi(t,T)\Pi_T \phi'(t,T) + \sum_{i=t}^{T} \phi(t,i) Q_i \phi'(t,i) \tag{5.11}$$

Simplifying and substituting into equations (5.4) and (5.5), we obtain the mean and covariance of the old increment given the target observation:

$$u_t = Q_t \Pi^{-1}(t,T)\phi(t,T)[y_T - \phi(T,t-1)x_{t-1}] \tag{5.12}$$

$$\tilde{Q}_t = Q_t - Q_t \Pi^{-1}(t,T) Q_t^{'} \tag{5.13}$$

The density on the initial state conditioned on the target observation is calculated similarly. The resulting mean and variance of the initial state is given by

$$\tilde{\Pi}_0 = (\Pi_0^{-1} + \Pi^{-1}(0,T))^{-1} \tag{5.14}$$

$$E[x_0 \mid y_T] = \tilde{\Pi}_0(0)(\Pi_0^{-1} m_0 + \Pi^{-1}(0,T)\phi(0,T) y_T) \tag{5.15}$$

A recursion can be obtained for equation (5.11) by writing $\Pi(t-1,T)$ in terms of $\Pi(t,T)$:

$$\begin{aligned} \Pi(t-1,T) = \phi(t-1,t)\Pi(t,T)\phi'(t-1,t) + \\ \phi(t-1,t) Q_{t-1} \phi'(t-1,t) \end{aligned} \tag{5.16}$$

with

$$\Pi(T,T) = \Pi_T + Q_T \tag{5.17}$$

Complementing the new initial conditions (5.14) and (5.15), the reach state equation can be written in various equivalent forms. The following form emphasizes that the old increment w_t has been broken into the estimate u_t of w_t from y_T and remaining uncertainty ε_t,

$$x_t = A_t x_{t-1} + u_t + \varepsilon_t \qquad (5.18)$$

$$\varepsilon_t \sim N(0, \tilde{Q}_t) \qquad (5.19)$$

with u_t as given in equation (5.12) and ε_t distributed as a zero-mean Gaussian with covariance $\tilde{Q}_t$.

This form is suggestive of stochastic control, where u_t is the control input that examines the state at time x_{t-1}, and generates a force to place the trajectory on track to meet the observed target. Nevertheless, this form emerges purely from conditioning the free movement state equation on the target observation rather than from any specific biological modeling of motor control. Note critically that u_t is a function of x_{t-1}, so that the covariance update in a Kalman filter implementation should not ignore this term.

Alternatively, we can group the x_{t-1} terms. This form is more conducive to the standard equations for the Kalman filter prediction update.

$$x_t = B_t x_{t-1} + f_t + \varepsilon_t \qquad (5.20)$$

$$B_t = [I - Q_t \Pi^{-1}(t,T)]A_t \qquad (5.21)$$

$$f_t = Q_t \Pi^{-1}(t,T)\phi(t,T) y_T \qquad (5.22)$$

In both forms, the resulting reach state equation remains linear with independent Gaussian errors ε_t, as detailed in the appendix. Because x_t is otherwise dependent on x_{t-1} or constants, we conclude that the reach state equation in (5.18) or (5.20) is a Markov process.

5.2.2 Augmented State Equation to Support Concurrent Estimation of Target

Building on the previous result, we can now construct a more versatile state equation that supports path and target estimation with concurrent observations of path and target. The previous reach state equation incorporates prescient target information into a space of current arm state x_t. We now augment the state space to include the target random variable x_T. According to this model, the state of the arm at time t is explicitly determined by the target and the state of the arm at time $t-1$.

The reach state equation derived above suggests an approach to calculating the state transition density $p(x_t, x_T \mid x_{t-1}, x_T)$ that corresponds to an augmented state equation. Because x_T is trivially independent of x_t conditioned on x_T, we can equivalently calculate the transition density of $p(x_t \mid x_{t-1}, x_T)$. This is identical to the reach state equation derivation of $p(x_t \mid x_{t-1}, y_T)$ with v_T set to zero. The resulting state equation can be consolidated into vector notation to give the augmented form:

$$\begin{pmatrix} x_t \\ x_T \end{pmatrix} = \begin{pmatrix} \Psi & \Gamma \\ 0 & I \end{pmatrix} \begin{pmatrix} x_{t-1} \\ x_T \end{pmatrix} + \begin{pmatrix} \varepsilon_t \\ 0 \end{pmatrix} \tag{5.23}$$

$$\Psi = B_t \tag{5.24}$$

$$\Gamma = Q_t \Pi^{-1}(t,T)\phi(t,T) \tag{5.25}$$

$$\Pi_T = 0 \tag{5.26}$$

The initial condition on the augmented state $[x_0, x_T]'$ is the joint distribution that corresponds to our uncertainty as external observers about the true starting and target states chosen by the brain at time zero.

This augmented state equation permits additional features to be incorporated into the model relative to the reach state equation. First, observations of the target can be incorporated throughout the duration of the reach to improve arm reconstructions. In contrast, the reach state equation incorporated one target observation before movement.

Second, refined estimates of the target can be generated recursively as estimates become more informed by reach and target related activity.

5.3 Results

5.3.1 Sample Trajectories

We proceed to illustrate the underlying structure of a reach for our goal-directed state equation, which appropriately constrains a general linear state equation to an uncertain target. We also explain how the underlying reach structure is affected by parameters of the model, namely reach duration, the target state observation, and target uncertainty.

The density on the set of trajectories, $p(x_t, x_{t\text{-}1}, ..., x_0 \mid y_T)$, can be calculated by iteratively multiplying the transition densities $p(x_t \mid x_{t-1}, y_T)$ given by the state equation. This density represents our assumptions about the trajectory before receiving additional observations of neural activity during the reach. Broader probability densities on the set of trajectories imply weaker assumptions about the specific path to be executed.

We can visually examine the structure of our assumptions by plotting samples from the density on trajectories as well as the average trajectory. Sample trajectories are generated by drawing increments ε_t from the density specified in equation (5.19). The simulated increments are accumulated at each step with $A_t x_t + u_t$, the deterministic component of the state equation (5.18). The resulting trajectory represents a sample drawn from $p(x_t, x_{t\text{-}1}, ..., x_0 \mid y_T)$, the probability density on trajectories. The average trajectory is generated from the same procedure, except that the increments ε_t are set to their means, which equal zero.

We first examine sample trajectories that result from small changes in model parameters. For illustration, the states were taken to be vectors $\left[x, y, v_x, v_y\right]_t^{'}$, representing position and velocity in each of two orthogonal directions. The original noise covariance was nonzero in the entries corresponding to velocity increment variances:

$$Q = \begin{pmatrix} 0 & 0 & 0 & 0 \\ 0 & 0 & 0 & 0 \\ 0 & 0 & q & 0 \\ 0 & 0 & 0 & q \end{pmatrix} \tag{5.27}$$

The uncertainty in target state Π_T was also diagonal, with

$$\Pi_T = \begin{pmatrix} r & 0 & 0 & 0 \\ 0 & r & 0 & 0 \\ 0 & 0 & p & 0 \\ 0 & 0 & 0 & p \end{pmatrix} \tag{5.28}$$

In Figure 5.2, sample trajectories from the reach state equation are generated with baseline parameters (Figure 5.2A) from which distance to target, reach duration, and increment uncertainty have been individually changed (Figures 5.2B-D). The baseline model parameters are given in the following table:

Parameter	Baseline Value
Reach distance	0.35 m
Time step	0.01 sec
Noise covariance (q)	$1\text{x}10^{-4}$ m^2
Reach duration	2 sec
Target position uncertainty (r)	$1\text{x}10^{-6}$ m^2
Target velocity uncertainty (p)	$1\text{x}10^{-6}$ m^2

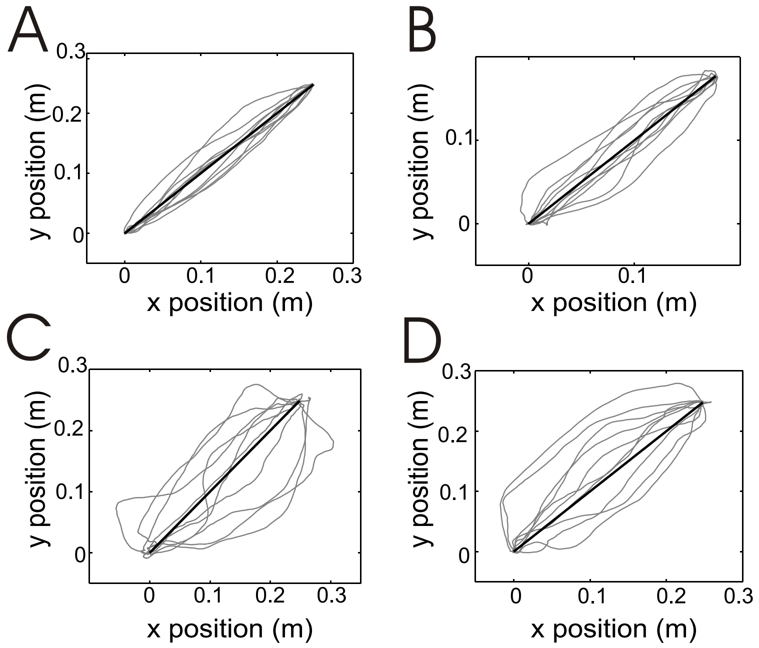

Figure 5.2. Sample trajectories (grey) and the true mean trajectory (black) corresponding to the reach state equation for various parameter choices. Appropriate changes in model parameters increase the observed diversity of trajectories, making the state equation a more flexible prior in reconstructing arm movements from neural signals. Parameter choices (detailed in section 3.1) were varied from **(A)** baseline, including **(B)** smaller distance to target, **(C)** increased time to target, and **(D)** increased increment uncertainty.

Parameters were individually altered from baseline as follows:

Parameter	Altered Value	Graph
Reach distance	0.25 m	Figure 5.2B
Reach duration	4 sec	Figure 5.2C
Noise covariance (q)	$3\text{x}10^{-4}$ m^2	Figure 5.2D

In Figure 5.3, sample trajectories are plotted for increasing uncertainty (r) in target position, with variances (A) $1\text{x}10^{-4}$, (B) $1\text{x}10^{-3}$, (C) $1\text{x}10^{-2}$, and (D) $1\text{x}10^{-1}$ m^2. This corresponds to scenarios in which observations of neural activity before movement initiation provide estimates of target position with varying certainty.

Figures 5.4A-C examines the velocity profiles in one direction generated by the reach state equation with various parameter choices. Velocity profiles from the baseline trajectory are displayed (Figure 5.4A), and parameters are sequentially altered from the baseline values (Figures 5.4B-C) as follows:

Parameter	Altered Value	Graph
Reach duration	4 sec	Figure 5.4B
Target position and velocity uncertainty	$r=1\text{x}10^{3}$ m^2 $p=1\text{x}10^{3}$ m^2	Figure 5.4C

Figure 5.4D examines the effect of target information on uncertainty in the velocity increment. The magnitude of one diagonal velocity term of the noise covariance $\tilde{Q}_t$ is plotted over the duration of the reach for comparison against the noise covariance Q_t of the corresponding free movement state equation.

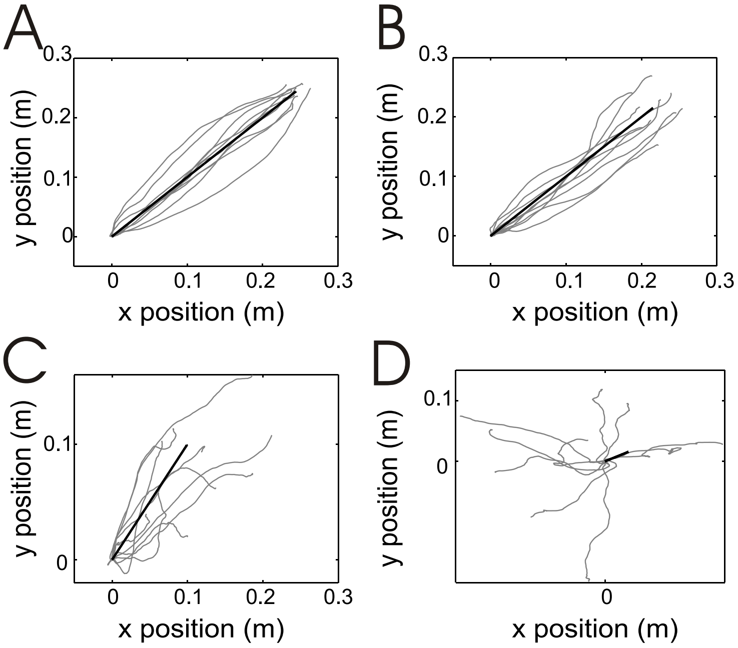

Figure 5.3. Sample trajectories (grey) and the true mean trajectory (black) of the reach state equation corresponding to various levels of uncertainty about target arm position. Variance in the noise v_T of the prescient observation y_T is progressively increased from **(A)** 1e-4, to **(B)** 1e-3, **(C)** 1e-2, and **(D)** 1e-1 m^2. As target uncertainty grows, trajectories become more unrestricted, corresponding to increasing flexibility in the prior for reconstruction of arm movements.

5.3.2 Reconstructing Arm Movements During a Reach

The reach state equation can be incorporated into any estimation procedure based on probabilistic inference, since it represents a recursively-computed prior. Because the reach state equation minimally constrains the path to the target observation, it may be useful in the analysis of coordinated neural activity with respect to planning and execution. We illustrate the reconstruction of reaching movements from simulated neural activity using a point process filter (Eden, Frank, Barbieri, Solo, & Brown, 2004), an estimation procedure that is conducive to the description of spiking activity in particular. The extension to variants of the Kalman filter is also direct, because the reach state equation (5.20) is written in standard Kalman filter notation.

We first simulated arm trajectories using the reach model as described in the previous section. For comparison, arm trajectories were also generated from a canonical model. This canonical model was a family of movement profiles from which specific trajectories could be chosen that guaranteed arrival at the desired target location and time:

$$\begin{pmatrix} x \\ y \\ v_x \\ v_y \end{pmatrix}_t = \begin{pmatrix} 1 & 0 & \Delta & 0 \\ 0 & 1 & 0 & \Delta \\ 0 & 0 & 1 & 0 \\ 0 & 0 & 0 & 1 \end{pmatrix} \begin{pmatrix} x \\ y \\ v_x \\ v_y \end{pmatrix}_{t-1} + (\frac{1}{2\delta})(\pi / T)^2 \cos(\pi t / T) \begin{pmatrix} 0 \\ 0 \\ x_T - x_0 \\ y_T - y_0 \end{pmatrix} \tag{5.29}$$

This deterministic equation relates velocities $\left[x, y, v_x, v_y \right]_t'$ to the time increment δ, the current time step t, and the distances in two orthogonal directions between the target and starting points, over $T+1$ time steps.

After generating trajectories, we simulated the corresponding multiunit spiking activity from 9 neurons, a typical ensemble size for present-day recording from a focal, single layer of cortex (Buzáki, 2004). Output from each unit in the ensemble was simulated independently as a point process with an instantaneous firing rate that was a function of the velocity.

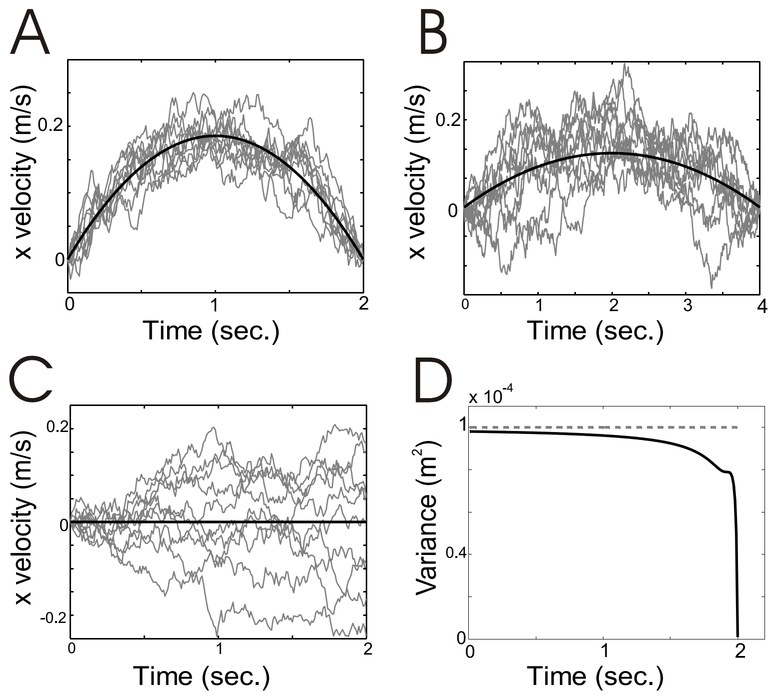

Figure 5.4. Sample velocity trajectories (grey) and the true mean velocity trajectory (black) generated by the reach state equation. **(A)** For baseline parameters (detailed in section 3.1) with reach duration of 2 seconds, the velocity profile is roughly bell-shaped. **(B)** As reach duration increases to 4 seconds, the trajectories become more varied. **(C)** If uncertainty in the observed target velocity and position is large (1e3 m^2 for each variance), velocity trajectories resemble samples from the free movement state equation. **(D)** Uncertainty in the velocity increment decreases with time due to the prescient target observation (solid line) as compared to the original velocity increment of the corresponding free movement state equation (dashed line).

This function, referred to as the conditional intensity (Eden, Frank, Barbieri, Solo, & Brown, 2004), is equivalent to specifying a receptive field. Our conditional intensity function is adapted from a model of primary motor cortex (Moran & Schwartz, 1999):

$$\lambda(t \mid v_x, v_y) = \exp(\beta_0 + \beta_1 (v_x^2 + v_y^2)^{1/2} \cos(\theta - \theta_p)) \tag{5.30}$$

$$= \exp(\beta_0 + \alpha_1 v_x + \alpha_2 v_y) \tag{5.31}$$

where v_x and v_y are velocities in orthogonal directions.

The receptive field parameters were either directly assigned or drawn from uniform probability densities on specific intervals as follows:

Parameter	Assignment or Interval
β_0	2.28
β_1	4.67 sec/m
θ_p	$[-\pi,\pi]$

The corresponding receptive fields had preferred directions between -π and π, background firing rates of 10 spikes/sec, and firing rates of 24.9 spikes/sec at a speed of 0.2 m/sec in the preferred direction.

Together with the simulated trajectory, this conditional intensity function specifies the instantaneous firing rate at each time sample based on current velocity. Spikes were then generated using the time rescaling theorem (Brown, Barbieri, Ventura, Kass, & Frank, 2002), where inter-spike intervals are first drawn from a single exponential distribution and then adjusted in proportion to the instantaneous firing rate. This method is an alternative to probabilistically thinning a homogeneous Poisson process.

The simulated spiking activity served as the input observations for the point process filter, described extensively in Eden, Frank, Barbieri, Solo, & Brown, 2004. The two defining elements of this filter are the state equation and observation equation. Our state equation is the reach model, and represents the dynamics of the variables we are estimating, specified by $p\left(x_t \mid x_{t\text{-}1}, y\right)$. Our observation equation is the receptive field of each neuron, specified by $p(\Delta N_t \mid \Delta N_{1:t\text{-}1}, x_t, y_T)$. This is the probability of observing ΔN_t spikes at time t, given previous spike observations $\Delta N_{1:t-1}$, the current kinematic state x_t, and the observation of target y_T. Because the spiking activity is described as a point process, the conditional intensity function specifies this observation density:

$$p(\Delta N_t \mid \Delta N_1, ..., \Delta N_{t\text{-}1}, x_t, y_T) \approx \exp[\Delta N_t^i \log(\lambda(\mathrm{t|x_t})\delta) - \lambda(\mathrm{t|x_t})\delta] \tag{5.32}$$

where δ denotes the time increment.

The formulation of a recursive estimation procedure from these two probability densities is the topic of Eden, Frank, Barbieri, Solo, & Brown, 2004. As with the Kalman filter, the resulting point process filter is comprised of a prediction step to compute $p(x_t \mid \Delta N_{1:t\text{-}1}, y_T)$ and an update step to compute $p(x_t \mid \Delta N_{1:t}, y_T)$. The reach state equation determines the mean and variance prediction steps of the point process filter, as given by

$$\hat{x}_{t|t-1} = B_t \hat{x}_{t-1|t-1} + f_t \tag{5.33}$$

$$\Lambda_{t|t-1} = B_t \Lambda_{t-1|t-1} B_t' + \tilde{Q}_t \tag{5.34}$$

The update step remains unchanged:

$$(\Lambda_{t|t})^{-1} = (\Lambda_{t|t-1})^{-1} + \left[\left(\frac{\partial \log \lambda}{\partial x_t}\right)\left[\lambda \Delta \delta_k\right]\left(\frac{\partial \log \lambda}{\partial x_t}\right) - \left(\Delta N_t - \lambda \Delta \delta_k\right)\frac{\partial^2 \log \lambda}{\partial x_t}\right]_{x_{t|t-1}} \tag{5.35}$$

$$\hat{x}_{t|t} = \hat{x}_{t|t-1} + \Lambda_{t|t}\left[\left(\frac{\partial \log \lambda}{\partial x_t}\right)'\left(\Delta N_t - \lambda \Delta \delta_k\right)\right]_{x_{t|t-1}} \tag{5.36}$$

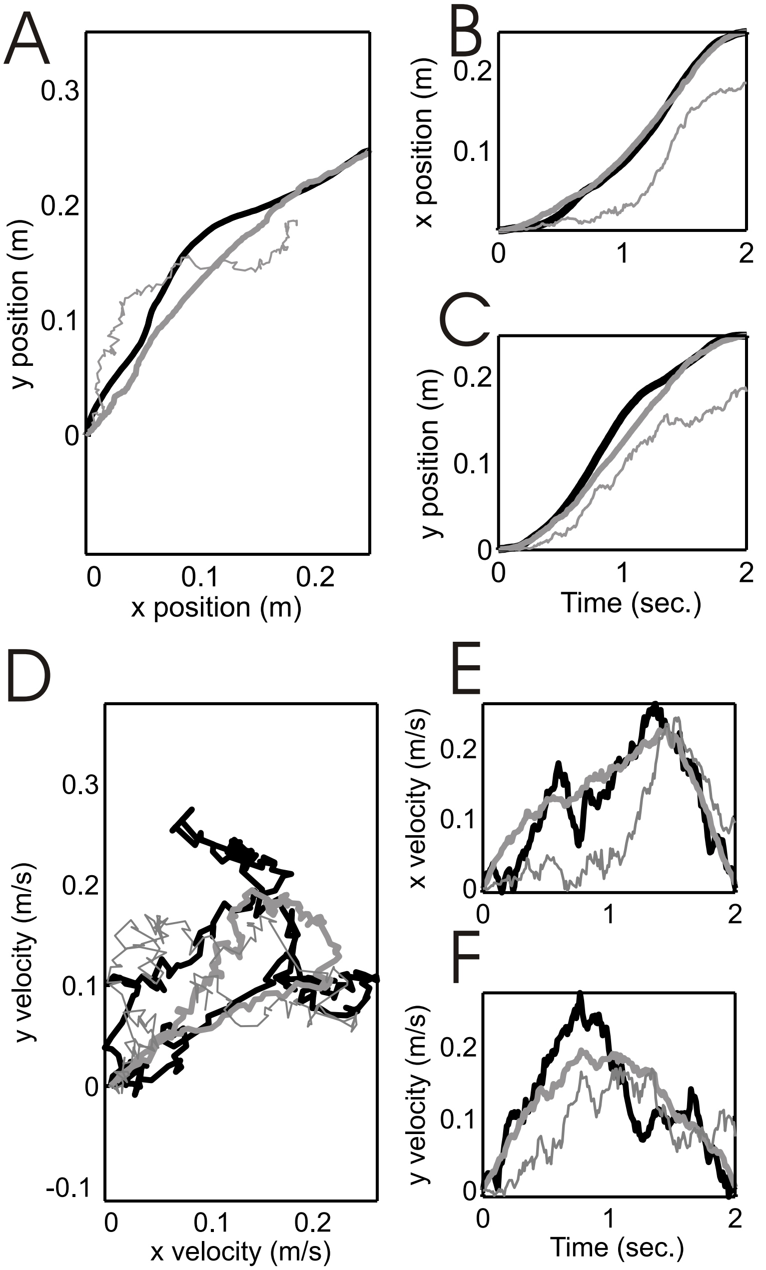

Figure 5.5. Reconstruction of reaching arm movements from simulated spiking activity. The reach state equation was used to generate trajectories, from which spiking activity was simulated with a receptive field model of primary motor cortex. Point process filter reconstructions using a free movement state equation (thin grey) and a reach state equation (thick grey) were compared against true movement values (black). Trajectories of x and y arm positions were plotted against each other **(A)**, and as a function of time **(B,C)**. Additionally, trajectories of x and y arm velocities were plotted against each other **(D)**, and as a function of time **(E,F)**. In these examples, target location is known almost perfectly to the reconstruction that uses the reach state equation, with position and velocity variances of 1e-5 m^2.

We compared the quality of reconstruction using the reach state equation versus the standard free arm movement state equation. The same covariance Q_t from equation (5.27) was incorporated into the free arm movement state equation (5.1) and the reach state equation (5.20). Figure 5.5 compares position and velocity decoding results for one simulated trial on a trajectory generated from the reach state equation. In this trial, the filter employing a reach state equation is provided the target location with relative certainty, by setting both the r and p parameters of Π_T to $1\times10^{-5}\,\mathrm{m}^2$ in equation (5.28). The point process filter appears to track the actual trajectory more closely with the reach state equation than with the free movement state equation.

Next, we examined the performance of the reach model point process filter in estimating trajectories that were generated from the canonical equation (5.29) rather than the reach state equation, to determine whether the reconstruction would still perform under model violation. Decoding performance for one trial with the canonical trajectory is illustrated in Figure 5.6, using the free movement state equation and the reach state equation with r and p in Π_T set to $1\times10^{-5}\,\mathrm{m}^2$ as with Figure 5.5. Again, the point process filter tracks the actual trajectory more closely when using the reach state equation than when using the free movement state equation.

We then assessed whether incorrect and uncertain target-planning information could be refined with neural activity that was informative about the path. We implemented the target-augmented state equation and examined the mean and variance of estimates of the target position as the reach progressed. Although the true target coordinates were (0.25 m, 0.25 m) on the x-y plane, the initial estimate of the target location was assigned to (1 m, 1 m) with a variance of 1 m^2, large relative to the distance between the initial target estimate and correct target location. Decoding performance for one trial is illustrated in Figure 5.7. In Figures 5.7 A and B, the estimate of the target location is shown to settle close to the true target location relative to the initial target

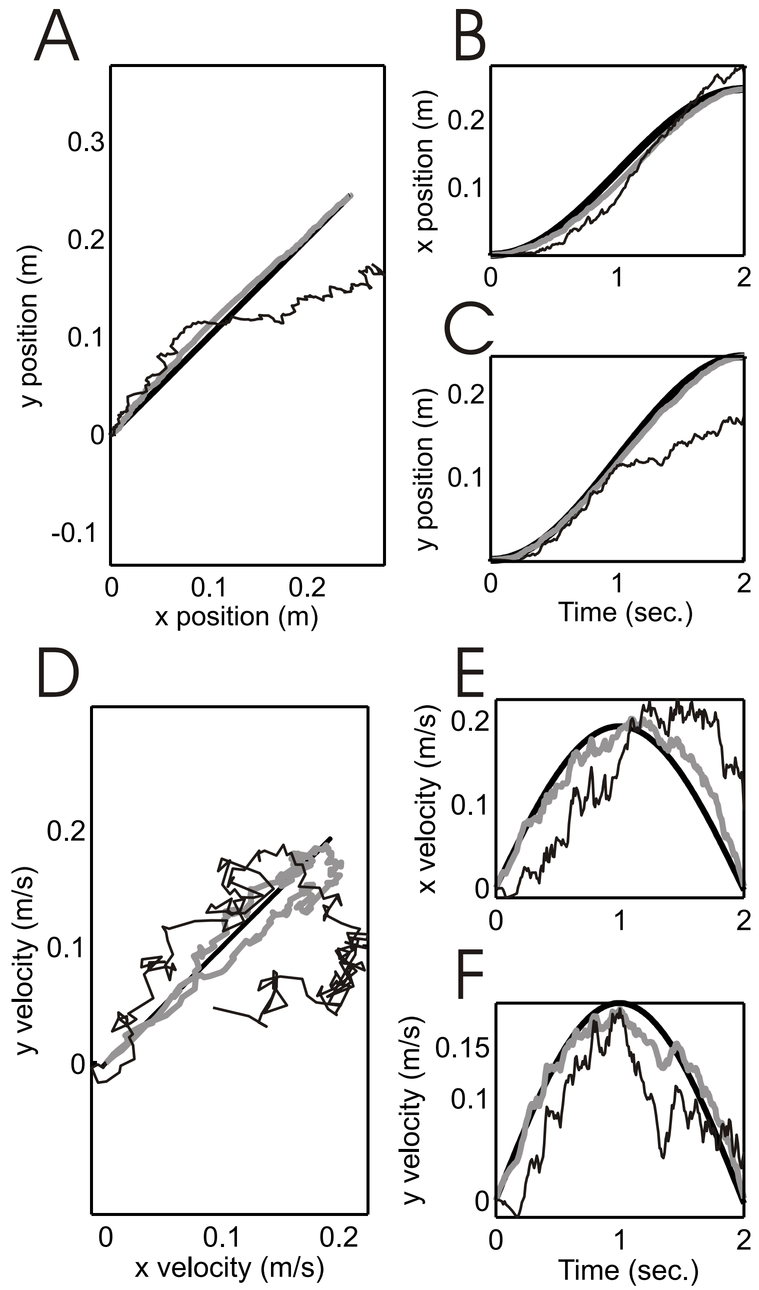

Figure 5.6. Reconstruction in the face of model violation. Trajectories are generated with an appropriately scaled cosine velocity profile. Again, results are compared for point process filtering using free (thin black) and reach (thick grey) movement state equations against true values (thick black). As with Figure 5.5, trajectories of x and y arm positions were plotted against each other **(A)**, and as a function of time **(B,C)**. Similarly, trajectories of x and y arm velocities were plotted against each other **(D)**, and as a function of time **(E,F)**. Position and velocity variances of the target observation are 1e-5 m^2.

estimate within 1.5 seconds of a 2 second reach. In Figure 5.7C, the variances in the position (solid) and velocity (dotted) estimates for target (black) approach the variances in estimates for the path (gray) as the reach proceeds.

Finally, we confirmed in simulation that the mean squared error of reconstruction using the reach state equation approaches that of the free movement state equation as the uncertainty in target position grows. One common simulated set of neural data was used to make a performance comparison between the two methods. Mean squared errors were averaged over 30 trials for the point process filter using the free and reach state equations separately. The results were plotted in Figure 5.8 for values of r and p in Π_T set equal, and over a range from $1\times10^{-7}\,\text{m}^2$ to 10 m^2, evenly spaced by 0.2 units on a $\log_{10}(\text{m}^2)$ scale. The mean squared error line for the reach state equation approaches that of the free movement state equation as Π_T grows large, and also flattens as Π_T approaches zero.

5.4 Discussion

We have developed a method for describing reaching arm movements with a general linear state equation that is constrained by its target. We first derived a reach state equation, which incorporates information about the target that is received prior to movement. This derivation was then adapted to explicitly include the target as an additional state space variable. The resulting augmented state equation supports the incorporation of target information throughout the reach as well as during the planning period.

As described in the derivation, the reach state equation is Markov. This property is guaranteed in part by the independence of noise increments that is demonstrated in the appendix. Consequently, the reach state equation is amenable to recursive estimation procedures. With no further alterations, the estimate of x_t can be obtained exclusively from the neural observation at time t and the estimate of x_{t-1} given data through time $t-1$.

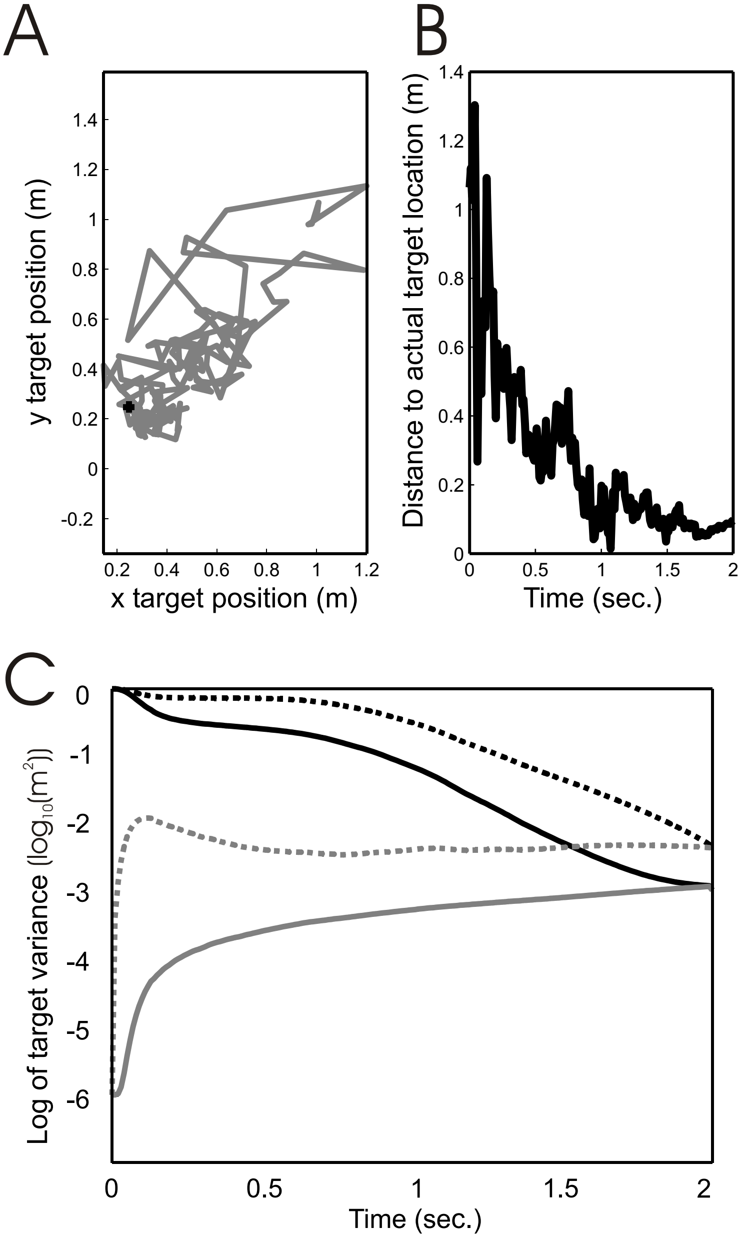

Figure 5.7. Target estimation with the augmented state equation for one trial. The initial estimate of the target is intentionally set to be incorrect at (1 m, 1 m) and with variance of 1 m^2 that is large relative to the distance to the true target location at (0.25 m, 0.25 m). Subsequent target estimates are produced using simulated neural spiking activity that relates directly to the path rather than the target. **(A)** Estimates of the target position are plotted in gray on the x-y axis, with the actual target marked as a black cross. **(B)** Distances from target estimates to the actual target location are plotted in meters against time. **(C)** Variances in estimates of target (black) and path (gray) are plotted on a logarithmic scale over the duration of one reach for position (solid) and velocity (dashed). These target estimate variances reduce with observations consisting only of simulated primary motor cortical activity relating to path.

The form of the reach state equation presented in (5.18) is particularly suggestive of stochastic control. In fact, the u_t component in (5.18) is the solution to the standard linear quadratic control problem. This represents a duality between estimation and control (Kailath, Sayed, & Hassibi, 2000). In this interpretation, the reach state equation is a model for the way in which the subject dynamically plans his path from a current position to the target. The stochastic increment ε_t represents our uncertainty as external observers, about the precise control strategy being employed. The variable u_t takes the role of a control input that represents the adjustments that the subject is expected to make to return the trajectory to a path that puts it on track to the target. In the reach state equation, u_t is a function of the state x_{t-1} and target observation y_T. In the augmented state equation, u_t is a function of x_{t-1} and the actual target x_T rather than the target observation y_T.

Various parameters work together to determine our uncertainty in the control strategy, including the increment variance in the original free movement state equation, distance to target, time to target, and target uncertainty. Together, these parameters determine whether the state equation at any given time forces the trajectory towards a particular target, or whether the trajectory tends to proceed in a relatively unconstrained fashion. Figures 5.2 and 3 describe the variation in trajectories that can be generated by modulating these parameters, from very directed movements to paths with nearly unconstrained directions.

The reach state equation in its simplest form is sufficient to generate, on average, bell-shaped velocity profiles that are similar to those observed in natural arm reaching (Morasso, 1981; Soechting & Lacquaniti, 1981). Models of reaching movement that are based on optimization of specific cost functions, examples of which include Hogan, 1984, Uno, Kawato, & Suzuki, 1989, Hoff & Arbib, 1993, and Harris & Wolpert, 1998, also generate these bell-shaped velocity profiles. It has been previously noted in a literature review (Todorov, 2004a) that these various methods implicitly or explicitly optimize a smoothness constraint. In our reach state equation, the bell-shaped velocity profile emerges implicitly from the zero-mean Gaussian increment of the original free movement state equation. This probability density sets a probabilistic smoothness constraint, where it is more likely that the state at consecutive time steps will be similar.

Additionally, symmetry in the profile emerges from the choice of a constant, invertible matrix A_t in equation (5.18) and equal mean starting and ending velocities, as with trajectories in Figures 5.4A. Optimal control models have previously reproduced the skewed velocity profiles (Hoff, 1992) that occur in experiments (Milner & Ijaz, 1990) where the target must be acquired with increased precision. With the reach state equation, skewed profiles may require the appropriate choice of time varying components such as A_t and w_t. When the arrival time grows longer (Figure 5.4B) or the endpoint becomes less constrained (Figure 5.4C) in the reach state equation, the trajectory tends to resemble a sample path of the free movement state equation, as intended by construction.

As the reaching motion approaches the target arrival time, our sense of the subject's control strategy becomes clearer, because we know the intended target with some uncertainty. We also know that the path must converge to this target soon. Furthermore, we can calculate the control signal that would achieve this goal based on the system dynamics represented by the A_t matrices in equation (5.18). Figure 5.4D illustrates that the uncertainty in the control strategy, represented by the variance in the stochastic increment ε_t, decreases over the duration of the reach based on y_T, the prescient observation of target. In contrast, the free movement state equation maintains constant uncertainty in the control strategy as the reach progresses because it is not informed about the target location.

Because the reach state equation incorporates target information, it is able to perform better than the equivalent free movement state equation that is uninformed about target. This is illustrated in Figure 5.5, where closer tracking is achieved over the entire reach when the state equation is informed about target than otherwise.

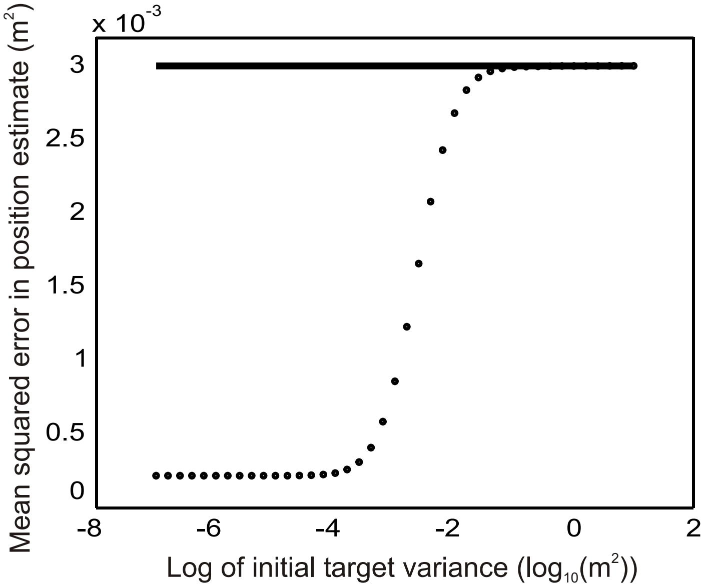

Figure 5.8. Performance comparison between two approaches to estimation on the same simulated set of neural data. Mean squared error (MSE) of position reconstruction is plotted versus $\log_{10}$ of uncertainty (variance) in the prescient observation of target. For each of 30 trials, receptive field parameters, trajectory, and spiking activity were simulated anew. For each target variance, MSE is averaged over reconstructions from the thirty trials. In the case of large initial target uncertainty, the MSE for reconstruction with the reach state equation (dotted) asymptotes to that of the free movement state equation (solid). The MSE for reconstruction with the reach state equation also asymptotes as initial target uncertainty diminishes.

This reach model and its augmented form are minimally constrained linear state equations. In a probabilistic sense, this means that the estimation prior at each step is only as narrow (or broad) as implied by the original free movement state equation and observations of path and target. In contrast, most reach models based on specific control strategies (Todorov, 2004b), cost functions (Todorov, 2004a), or canonical models (Kemere, Santhanam, Yu, Shenoy, & Meng, 2002; Cowan & Taylor, 2005), place additional constraints on the path that make the estimation prior more exclusive of alternate paths to target. An exception is Kemere & Meng, 2005, which uses the linear quadratic control solution that provides identical average trajectories to the reach state equation, based on the estimation-control duality (Kailath, Sayed, & Hassibi, 2000) although the resulting increment variances are different. As depicted in Figure 5.6, estimation with a reach state equation is able to perform under model violation, where arm movements are generated by a different model, while still taking advantage of the target information.

The target-augmented state equation also allows neural activity related to path to inform estimates of the target. This is illustrated in Figure 5.7, where the initial estimate of target position was assigned to be incorrect and with large uncertainty (variance). Consequently, the estimate of the target location relied in large part on neural activity that related to the path. The augmented state equation projects current path information forward in time to refine target estimates. As a result, the estimated target location in Figure 5.7B settled close to the actual target location 0.5 seconds before completion of the 2 second reach. The remaining distance between the target location estimate and the actual target location is limited by the extent to which path-related neurons provide good path estimates. For example, path-related neural activity that is relatively uninformative about path will result in poor final estimates of target when combined only with poor initial target information. Because the target in the augmented state equation is simply the final point of the path, the variance in the target estimate plotted in Figure 5.7C, approaches that of the path estimate as the reach proceeds to the arrival time T.

The reach state equation in (5.18) or (5.20) reduces to the original free movement state equation in the limit that the prescient target observation is completely uncertain. This explains the trend in Figure 5.8, where mean squared error in trajectory estimates with the reach state equation approaches that of the free movement state equation. Estimates were produced from a common simulated set of neural data to allow performance comparison between these two approaches.

Filtering with the reach (5.18) and augmented state equations (5.23) bears resemblance to fixed interval smoothing. Fixed interval smoothing refers to a class of estimation procedures that produce maximum a posteriori estimates of trajectory values over an interval with observations of the trajectory over the entire interval (Kailath, Sayed, & Hassibi, 2000). In filtering with the reach state equation, estimates at a given time t are based on data received through time t and the single prescient observation y_T on the target state x_T. In filtering with the augmented state equation, estimates of x_T are based on data received through time t and potentially multiple prescient observations on x_T. While these three filter types employ observations of future states in maximum a posteriori estimates, there are important distinctions in terms of which observations are used and allowance for multiple sequential observations of a single state, such as with x_T in the augmented state equation.

Although parallels exist to stochastic control, there is a sharp distinction between the results of this chapter and a control-based state equation (Todorov, 2004b; Kemere & Meng, 2005). First, the reach state equation was derived as the natural extension of a free movement state equation, with no further assumptions. In contrast, control based state equations are derived by assuming a specific form for the brain's controller and choosing the parameters that optimize some cost function. Second, the increment in the reach state equation approaches zero for perfectly known targets. The increment of control-based state equations persists, and represents system properties rather than our uncertainty about the control signal. Third, the reach state equation describes the target state in the most general sense, including the possibility of non-zero velocities. While this can be accommodated into the control framework, the classical notion of a reaching motion has been to a target with zero velocity.

Distinctions between the reach state equation and control-based state equations are especially important in considering the study of reaching motions. Recursive estimation coupled with a state equation that relates target to path provides a convenient tool for the analysis of neural data recorded during planning and execution of goal-directed movements. The state-space estimation framework can assess the extent to which neural data and an observation equation improve the reconstruction beyond information about the movement built into the state equation. Classically, control-based state equations have been developed to explain as many features about reaching movements as possible without any neural data. In contrast, the reach state equation was developed to extend the free movement state equation with no further assumptions. Both approaches represent different levels of detail in a spectrum of models for the dynamics that drive the observed neural activity in brain regions that coordinate movement. These models can be used to clarify the roles of various brain regions or the validity of alternate neural spiking relationships.

The reach and augmented state equations may also provide improved control in brain machine interfaces (Srinivasan, Eden, Willsky, & Brown, 2005) by allowing the user to specify a target explicitly with neural signals, or implicitly through the probability density of potential targets in a workspace. This and other recent approaches (Cowan & Taylor, 2005; Yu, Santhanam, Ryu, & Shenoy, 2005; Kemere & Meng, 2005) are hybrids between target based control prosthetics (Musallam, Corneil, Greger, Scherberger, & Andersen, 2004; Santhanam, Ryu, Yu, Afshar, & Shenoy, 2005) and path based control prosthetics (Carmena, et al., 2003; Taylor, Tillery, & Schwartz, 2002; Wu, Shaikhouni, Donoghue, & Black, 2004), perhaps most relevant when neither approach alone is sufficient for the desired level of control using available recording hardware to complete a task. Additionally, the method could support more robust receptive field estimates in the face of disappearing units due to neuronal death or tissue retraction (Eden, Truccolo, Fellows, Donoghue, & Brown, 2004). The flexibility of the reach and augmented state equations over more specific reach models might also allow the user to employ the same reaching algorithm to navigate obstacles in acquiring their target.

In developing the method further for scientific and clinical application, it is important to consider limitations of the equations presented in this chapter. Importantly, both the augmented and reach state equation are written for the prescient observation of a target with known arrival time T. We are currently developing a principled approach to accommodate uncertain arrival time, although uncertainty in the target velocity estimate might be a convenient surrogate. Also, the calculations were simplified greatly by assuming a linear free-arm-movement state equation with Gaussian increments. This may not be possible if linear approximation is insufficient to describe the nonlinear dynamics of a movement. Finally, additional experimental work will be needed to elucidate the appropriate observation equations, recording sites, and patient rehabilitation regimen that would enhance the clinical application of this hybrid approach to control prosthetics.

5.5 Appendix: Proof of Independent Increments in the Reach State Equation

The new increments are defined as $\varepsilon_t = w_t - E\left[w_t \mid y_T, x_{t-1}\right]$. Substituting equation (5.6) into an equation that is equivalent to (5.12), we can rewrite the new increments as

$$\varepsilon_t = w_t - Q_t\phi(T,t)^{'} S_t^{-1}\left(\sum_{i=t}^{T}\phi(T,i)w_i + v_T\right), \tag{5.37}$$

where $S_t = R_T + \sum_{i=t}^{T}\phi(T,i)Q_i\phi(T,i)^{'}$ and R_T is the covariance of the observation random variable y$_T$, with $R_T = \phi(T,t-1)V_{t-1}\phi'(T,t-1) + \sum_{i=t}^{T}\phi(T,i)Q_i\phi'(T,i) + \Pi_T$.

Therefore, ε_t can be written entirely in terms of the future increments $\left\{w_i\right\}_{i=t}^{T}$ and v_T. For $s < t$,

$$\begin{aligned}
E\left[\varepsilon_t\varepsilon_s^{'}\right] &= E\left[\left(w_t - Q_t\phi(T,t)^{'} S_t^{-1}\left(\sum_{i=t}^{T}\phi(T,i)w_i + v_T\right)\right)\left(w_s - Q_s\phi(T,s)^{'} S_s^{-1}\left(\sum_{i=s}^{T}\phi(T,i)w_i + v_T\right)\right)^{'}\right] \\
&= -Q_t\phi(T,t)^{'} S_s^{-1}\phi(T,s)Q_s + Q_t\phi(T,t)^{'} S_t^{-1}\left(\sum_{i=t}^{T}\phi(T,i)Q_i\phi(T,i)^{'} + R_T\right)S_s^{-1}\phi(T,s)Q_s \\
&= -Q_t\phi(T,t)^{'} S_s^{-1}\phi(T,s)Q_s + Q_t\phi(T,t)^{'} S_s^{-1}\phi(T,s)Q_s \\
&= 0
\end{aligned} \tag{5.38}$$

5.6 References

Andersen, R. A., & Buneo, C. A. (2002). Intentional maps in posterior parietal cortex. *Annual Review of Neuroscience* 25:189–220

Ashe, J., and Georgopoulos, A.P. (1994). Movement parameters and neural activity in motor cortex and area 5. *Cerebral Cortex, 4,* 590–600.

Barbieri, R., Frank, L. M., Nguyen, D. P., Quirk, M. C., Solo, V., Wilson, M. A., & Brown, E. N. (2004). Dynamic analyses of information encoding by neural ensembles. *Neural Computation, 16(2),* 277-308.

Brown, E. N., Barbieri, R., Ventura, V., Kass, R. E., & Frank, L. M. (2002). The time-rescaling theorem and its application to neural spike train data analysis. *Neural Computation, 14(2),* 325-346.

Buzáki, G. (2004). Large-scale recording on neuronal ensembles. *Nature Neuroscience, 7,* 446-451.

Carmena, J. M., Lebedev, M. A., Crist, R. E., O’Doherty, J. E., Santucci, D. M., Dimitrov, D. F., Patil, P. G., Henriquez, C. S., & Nicolelis, M. A. L. (2003). Learning to control a brain-machine interface for reaching and grasping by primates. *Public Library of Science Biology, 1(2),* 193-208.

Castanon, D. A., Levy, B. C., & Willsky, A. S. (1985). Algorithms for the incorporation of predictive information in surveillance theory. *International Journal of Systems Science, 16(3),* 367-382.

Cowan, T. M., Taylor, D. M. (2005). Predicting reach goal in a continuous workspace for command of a brain-controlled upper-limb neuroprosthesis. *Proceedings of the 2nd International IEEE EMBS Conference on Neural Engineering*, Arlington VA, p. 74.

Eden, U. T., Frank, L. M., Barbieri, R., Solo, V., & Brown, E. N. (2004). Dynamic analyses of neural encoding by point process adaptive filtering. *Neural Computation, 16(5),* 971-998.

Eden, U. T., Truccolo, W., Fellows, M. R., Donoghue, J. P., & Brown, E. N. (2004) Reconstruction of Hand Movement Trajectories from a Dynamic Ensemble of Spiking Motor Cortical Neurons. *Proceedings of the 26th Annual International Conference of the IEEE EMBS*, San Francisco, CA.

Fu, Q.-G., Suarez, J.I. & Ebner, T.J. (1993). Neuronal specification of direction and distance during reaching movements in the premotor area and primary motor cortex of monkeys. *Journal of Neurophysiology, 70(5),* 2097-2116.

Georgopoulos, A. P., Kalaska, J. F., Caminiti, R., & Massey, J. T. (1982). On the relations between the direction of two dimensional arm movements and cell discharge in primate motor cortex. *Journal of Neuroscience, 2*, 1527-1537.

Georgopoulos, A., Kettner, R., & Schwartz, A. (1988). Primary motor cortex and free arm movements to visual targets in three-dimensional space. ii. Coding of the direction of movement by a neuronal population. *Journal of Neuroscience, 8(8)*, 2928-2939.

Georgopoulos, A. P., Ashe, J., Smyrnis, N., & Taira, M. (1992). Motor cortex and the coding of force. Science, 256, 1692–1695.

Geschwind, N., & Damasio, A. R. (1985). Apraxia. In Vinken, P. J., Bruyn, G. W., & Klawans, H. L. (Eds.), *Handbook of Clinical Neurology* (pp. 423-432) Amsterdam: Elsevier.

Greger, B., Norris, S. A., & Thach, W. T. (2003). Spike firing in the lateral cerebellar cortex correlated with movement and motor parameters irrespective of the effector limb. *Journal of Neurophysiology, 91*, 576-582.

Harris, C. M., & Wolpert, D. M. (1998). Signal-dependent noise determines motor planning. *Nature*, *394*, 780-784.

Hoff, B., & Arbib, M.A. (1993). Models of trajectory formation and temporal interaction of reach and grasp. *Journal of Motor Behavior 25*, 175–192.

Hogan, N. (1984). An organizing principle for a class of voluntary movements. *Journal of Neuroscience*, *4*, 2745–2754.

Kailath, T., Sayed, A. H., & Hassibi, B. (2000). *Linear Estimation*. Upper Saddle River, NJ: Prentice Hall.

Kemere, C., Santhanam, G., Yu, B. M., Shenoy, K. V., & Meng, T. H. (2002). Decoding of plan and peri-movement neural signals in prosthetic systems. *IEEE Workshop on Signal Processing Systems*, San Diego, CA.

Kemere, C., & Meng, T. H. (2005). Optimal estimation of feed-forward-controlled linear systems. *IEEE International Conference on Acoustics, Speech and Signal Processing*, Philadelphia, PA.

Li, C. R., Padoa-Schioppa, C., & Bizzi, E. (2001). Neuronal correlates of motor performance and motor learning in the primary motor cortex of monkeys adapting to an external force field. *Neuron, 30*, 593-607.

Moran, D. W., & Schwartz, A. B. (1999). Motor cortical representation of speed and direction during reaching. *Journal of Neurophysiology, 82(5)*, 2676-2692.

Morasso, P. (1981). Spatial control of arm movements. *Experimental Brain Research, 42,* 223-227.

Mussallam, S., Corneil, B. D., Greger, B., Scherberger, H., & Andersen, R. A. (2004). Cognitive control signals for neural prosthetics. *Science, 305*, 258-262.

Nakano, E. et al. (1999). Quantitative examinations of internal representations for arm trajectory planning: minimum commanded torque change model. *Journal of Neurophysiology, 81,* 2140–2155.

Nudo, R. J., Wise, B. M., SiFuentes, F., & Milliken, G. W. (1996). Neural substrates for the effects of rehabilitation training on motor recovery after ischemic infartct. *Science, 272*, 1791-1794.

Paninski, L., Fellows, M. R., Hatsopoulos, N. G., & Donoghue, J. P. (2004). Spatiotemporal tuning of motor cortical neurons for hand position and velocity. *Journal of Neurophysiology, 91*, 515-532.

Santhanam, G., Ryu, S. I., Yu, B. M., Afshar, A., Shenoy, K. V. (In Press). A high performance neurally-controlled cursor positioning system. *IEEE Engineering in Medicine and Biology (EMBS) 2nd International Conference on Neural Engineering*.

Schwartz, A. B. (1992). Motor cortical activity during drawing movements: single-unit activity during sinusoid tracing. *Journal of Neurophysiology, 68,* 528–541.

Schwartz, A. B., Moran, D. W. & Reina, G. A. (2004). Differential representation of perception and action in the frontal cortex. *Science, 303,* 380-383.

Smith, A. C., Frank, L. M., Wirth, S., Yanike, M., Hu, D., Kubota, Y., Graybiel, A. M., Suzuki, W. A., & Brown, E. N. (2004). Dynamic analyses of learning in behavioral experiments. *Journal of Neuroscience, 24(2)*, 447-461.

Soechting, J.F., & Lacquaniti, F. (1981) Invariant characteristics of a pointing movement in man. *Journal of Neuroscience, 1,* 710-720.

Srinivasan, L., Eden, U. T., Willsky, A. S., & Brown, E. N. (2005). Goal-directed state equation for tracking reaching movements using neural signals. *Proceedings of the 2nd International IEEE EMBS Conference on Neural Engineering,* Arlington, VA, p. 352.

Taira, M., Boline, J., Smyrnis, N., Georgopoulos, A. P., & Ashe, J. (1995). On the relations between single cell activity in the motor cortex and the direction and magnitude of three-dimensional static isometric force. *Experimental Brain Research, 109,* 367–376.

Taylor, D. M., Tillery, S. I. H., & Schwartz, A. B. (2002). Direct cortical control of 3D neuroprosthetic devices. *Science, 296*, 1829-1832.

Todorov, E. (2000). Direct cortical control of muscle activation in voluntary arm movements: a model. *Nature Neuroscience, 3(4)*, 391-398.

Todorov, E., & Jordan, M. I. (2002). Optimal feedback control as a theory of motor coordination. *Nature Neuroscience, 5*, 1226-1235.

Todorov, E. (2004a). Optimality principles in sensorimotor control. *Nature Neuroscience, 7(9)*, 907-915.

Todorov, E. (2004b). Stochastic optimal control and estimation methods adapted to the noise characteristics of the sensorimotor system. *Neural Computation*, *17*, 1084-1108.

Truccolo, W., Eden, U. T., Fellows, M., Donoghue, J. D., & Brown, E. N. (2005). A point process framework for relating neural spiking activity history, neural ensemble and covariate effects. *Journal of Neurophysiology, 93*, 1074-1089.

Turner, R. S., & Anderson, M. E. (1997). Pallidal discharge related to the kinematics of reaching movements in two dimensions. *Journal of Neurophysiology, 77*, 1051-1074.

Uno, Y., Kawato, M. & Suzuki, R. (1989). Formation and control of optimal trajectory in human multijoint arm movement: Minimum torque-change model. *Biol. Cybern. 61,* 89–101.

Verghese, G., & Kailath, T. (1979) A further note on backwards Markovian models. *IEEE Transactions on Information Theory, IT-25(1)*.

Warland, D. K., Reinagel, P., & Meister, M. (1997). Decoding visual information from a population of retinal ganglion cells. *Journal of Neurophysiology*, *78*, 2336-2350.

Wise, S. P., Boussaoud, D., Johnson, P. B., & Caminiti, R. (1997). Premotor and parietal cortex: corticortical connectivity and combinatorial computations. *Annual Review of Neuroscience, 20*, 25-42.

Wu, W., Black, M. J., Mumford, D., Gao, Y., Bienenstock, E., & Donoghue, J. P. (2004). Modeling and decoding motor cortical activity using a switching Kalman filter. *IEEE Transactions on Biomedical Engineering, 51(6)*, 933-942.

Wu, W., Shaikhouni, A., Donoghue, J. P., & Black, M. J. (2004). Closed-loop neural control of cursor motion using a Kalman filter. *The 26th Annual International Conference of the IEEE Engineering in Medicine and Biology Society*, San Francisco, CA.

Yu, B. M., Santhanam, G., Ryu, S. I., & Shenoy, K. V. (2005). Feedback-directed state transition for recursive Bayesian estimation of goal-directed trajectories. *Computational and Systems Neuroscience (COSYNE) meeting*, Salt Lake City, UT.

Chapter 6

General-Purpose Filter Design for Neural Prosthetic Devices

Brain-driven interfaces depend on estimation procedures to convert neural signals into inputs of automated controllers of prosthetic devices that can assist individuals with severe motor deficits. Previous estimation procedures were developed on a case-by-case basis for specific applications. In this chapter, we present a coherent estimation framework that unifies these procedures and motivates new applications. The brain-driven interface is described as an interaction between neural activity and interacting components of a prosthetic device that may take on discrete or continuous values. To support neural prosthetics driven by action potentials, a new filtering estimation procedure is developed for point process observations which depend on hybrid state dynamics. A corresponding Gaussian process filtering procedure is proposed for continuous field potentials. We test our framework against dominant approaches in a motor reaching task using simulated traces of ensemble spiking activity from primary motor cortex. Results predict that the hybrid framework outperforms previous approaches in the control of arm position and velocity based on trajectory and endpoint mean squared error. The hybrid framework can be used to operate a diverse set of devices including computers, robotic limbs, and muscle-embedded electrodes. Moreover, the approach can be applied to a diverse set of biological signals, such as electromyograms (EMG), electroencephalograms (EEG), electrocorticoencephalograms (ECoG), local field potentials (LFP), and action potentials.

6.1 Introduction

Amyotrophic lateral sclerosis, spinal cord injury, brainstem infarcts, advanced-stage muscular dystrophies, and diseases of the neuromuscular junction profoundly disrupt voluntary muscle control. New technologies, variously called brain-computer interfaces [1, 2], motor neural prostheses [3-5], and cognitive prostheses [6, 7], represent a communication link that bypasses affected channels of motor output. Functional electrical stimulation, manually actuated devices, eye tracking, and other approaches [8, 9] represent practical solutions for many patients, but may not be feasible for individuals with profound motor deficits. Moreover, brain-driven interfaces have the potential to provide dexterous and natural control without muscle fatigue.

A brain-driven interface includes a method to monitor neural activity, an algorithm to map neural activity to control signals, a device to be controlled, and a feedback mechanism from the device to the user [10-14]. This chapter relates to the optimal mapping between preprocessed neural activity and estimates of the user's intention that determine control signals. The method presented here unifies four canonical approaches, demonstrates new applications, and suggests one path to further algorithm development.

In prosthetics literature, the optimal mapping is predominantly described as an estimation (filtering) problem followed by a control problem. First, an estimate of the user-intended prosthetic device state is calculated based on neural activity that serves as a noisy observation of that intention. Second, a control law determines inputs to the device that achieve this estimate of the user-intended device state. This optimization ignores feedback to the user, but provides a practical approach that is accomodated within the existing framework of estimation theory or similarly, a tracking problem in stochastic control. Previous approaches to the estimation problem include: manually adjusted linear combinations of power spectral band energies [15], population vectors for automated but sub-optimal linear mappings [16], linear regression for optimized linear mappings [17], support vector machines, and recursive Bayesian estimation procedures, including the Kalman filter [18], particle filter [19], and point process filter [20, 21].

Bayesian estimation allows dramatically better tracking than linear regression in off-line data analyses. This approach describes the intended state of a prosthetic device and observed neural activity as a sequence of random variables indexed by time. The trajectory model defines a prior on the sequence of intended device states. The observation model defines the relationship between neural activity and intended device states. Actual device states are determined from neural activity based on these trajectory and observation models.

In the following sections, we present an estimation framework for brain-driven interfaces that explicitly allows the designer to span a full range of device capabilities by employing a hybrid state space composed of interacting discrete and continuous valued random processes. This method is shown to generalize previous Bayesian approaches to prosthesis design, including finite state machines [6], free arm movement models [18], reaching movement trajectory models [22-28] switching observation model [25], and the mixture of trajectories model [29]. One possible filtering procedure is derived for point process observations on the hybrid state space, and connections are drawn to existing literature on hybrid estimation for Gaussian observation processes (switching Kalman filters). To demonstrate the versatility of this framework, three emerging prosthetic device applications are described: free arm movement with definitive stopping, reaching movements with variable arrival time, and reaching to a target that may change within a discrete set of targets over the course of the movement. This final application is demonstrated in simulation with a point process model of primary motor cortical activity.

6.2 The hybrid framework

In the formulation of the neural prosthesis estimation problem, the user communicates the intended state of the prosthetic device via neural signals. The optimal brain-driven interface must convert these neural signals into an estimate of the intented device state that minimizes some distance metric (cost) to the intended sequence of device states. The cost is commonly assumed to be some form of mean squared error for continuous-valued device states and frequency of proper classification for discrete-valued states [10-14]. Implicit in this formulation, a controller is subsequently expected to receive the estimate and drive the device to the corresponding state with the required precision and response time.

To maintain generality, we describe the user-intended device state at time step k by a vector of discrete random variables s_k and continuous random variables x_k. The user drives neural activity $n_k^{1:C}$ from C channels at time step k based on the desired device states s_k and x_k. Although we refer to n_k^c as the activity of the c^{th} neuron in the specific context of multiple single unit recording, n_k^c may correspond more generally to the c^{th} signal of any measurement of activity, including single neuron spiking, multiunit activity, continuous electric field measurements, and even eye movements. The history of activity this time step, $H_k = \left(n_1^{1:C}, n_2^{1:C}, ..., n_{k-1}^{1:C}\right)$, may also affect $n_k^{1:C}$ due to recurrent neural connections and other sources of history dependence.

As an illustration of these variables, consider driving a car with your EEG instead of with your arms. Your intention to increment or decrement the gear as well as the current gear position can be captured by a discrete variable s_k, whereas the desired wheel or gas pedal angles can be further described by the continuous variable x_k that evolve depending on the resulting gear position recorded in s_{k+1}. The EEG amplitudes on C different channels, indicated by $n_k^{1:C}$, may depend on your discrete and continuous-valued intentions for the car, but also the history of previous amplitudes H_k because of the nature of oscillations. Note that the intended device state need not correspond literally to parts of the car, as with the intention to increment or decrement the gear. The choice of variables can dramatically impact ease of use, just as with the design of an interface to a consumer electronic device such as the MP3 player.

The hybrid state space is a joint probability density on the entire temporal sequence (trajectory) of intended states and neural activity $p(x_1, s_1, n_1^{1:C}, x_2, s_2, n_2^{1:C}, ...)$. Graphical models on acyclic graphs are a pictoral description of this joint density. By describing the state space this way, we constrain the form of the joint density to allow a simple and consistent prescription. Consider our specific graphical model of the hybrid state space (Figure 6.1a), which illustrates only one segment of the entire trajectory. The circles, called nodes, denote random variables corresponding to the intended states and neural activity. The arrows specify interdependencies between the random variables. A consistent prior distribution on the entire set of nodes is provided by specifying distributions for each node conditioned on its parents, which are all nodes at the base of arrows that point to that node. Nodes without parents require unconditioned priors. The graphical model imposes a Markov structure, where any node is independent of all other nodes when conditioned on its parents. The hanging arrows directed towards $n_k^{1:C}$ and $n_{k+1}^{1:C}$ represent history dependence in the neural activity.

The probability distribution $p(n_k^{1:C} \mid x_k, s_k, H_k)$ associated with this hybrid state space corresponds to the observation model, because it relates the present measurement of neural activity to the present intention of the user and the history of neural activity. The probability distributions $p(x_{k+1} \mid x_k, s_{k+1})$ and $p(s_{k+1} \mid s_k)$ comprise the trajectory model; they describe the frequency and types of transitions in user intent for which the prosthetic device is designed.

In principle, the observation model should properly describe the relation between neural observations and user intent and the trajectory model should accurately reflect the distribution of user intents. Model mismatch describes errors that accumulate from an incorrect model specification. Whereas continuous field potentials (LFP, ECoG, EEG) are typically described by Gaussian observation models [30], spiking activity at millisecond resolution is better described by point process observation models [31-34]. The continuous component $p(x_{k+1} \mid x_k, s_{k+1})$ of the trajectory model can often be reasonably approximated as Gaussian to anticipate smooth changes in the user's continuous state intent when conditioned on a particular discrete state. The discrete component of the trajectory model $p(s_{k+1} \mid s_k)$, also called the state transition density, is generally defined by specifying a probability between 0 and 1 for each possible pair of intentions (s_{k+1}, s_k), although parameterization may be relevant to dealing with a large set of discrete intentions.

Alternate connections could have been used to describe the hybrid state space. The specific choice of connections made (Figure 6.1a) draws on a standard form used in hybrid filtering on Gaussian observations [35], but extends it to accommodate arbitrary history dependence. This imposed structure on the state space makes it easy to obtain estimates of the intended device state in a recursive fashion, based on the latest set of neural activity. Moreover, the connections are sufficiently general as to accommodate a diverse set of applications.

Five previously described Bayesian approaches to neural prosthetics fall within this single framework (Figures 6.1 b, c, d, and e). A finite state machine description of the prosthesis [6] consists of a sequence of discrete user-intended states, rules for transitions between those states, and a relationship between states and neural signals (Figure 6.1b). Free arm movement models [18] and reaching movement trajectory models [22-24, 26-28, 36], both describe continuous-valued arm movement intentions that drive neural activity (Figure 6.1c). The switching observation model [25] accomodates poorly sorted neural activity that might be better described by combinations of single cell receptive fields (Figure 6.1d). The mixture of trajectories model [29] was designed for continuous-valued reaching movements to a stationary target drawn from a discrete set (Figure 6.1e).

While the hybrid state space depicted (Figure 6.1) unifies these previous conceptions of neural prosthesis design, an estimation procedure (filter) must still be specified to generate probability densities of intended device states given neural activity from which average cost measures can be minimized. In the following sections, we develop a point process filter for spiking observations in the hybrid state space and review the corresponding Gaussian process filter for continuous field potentials.

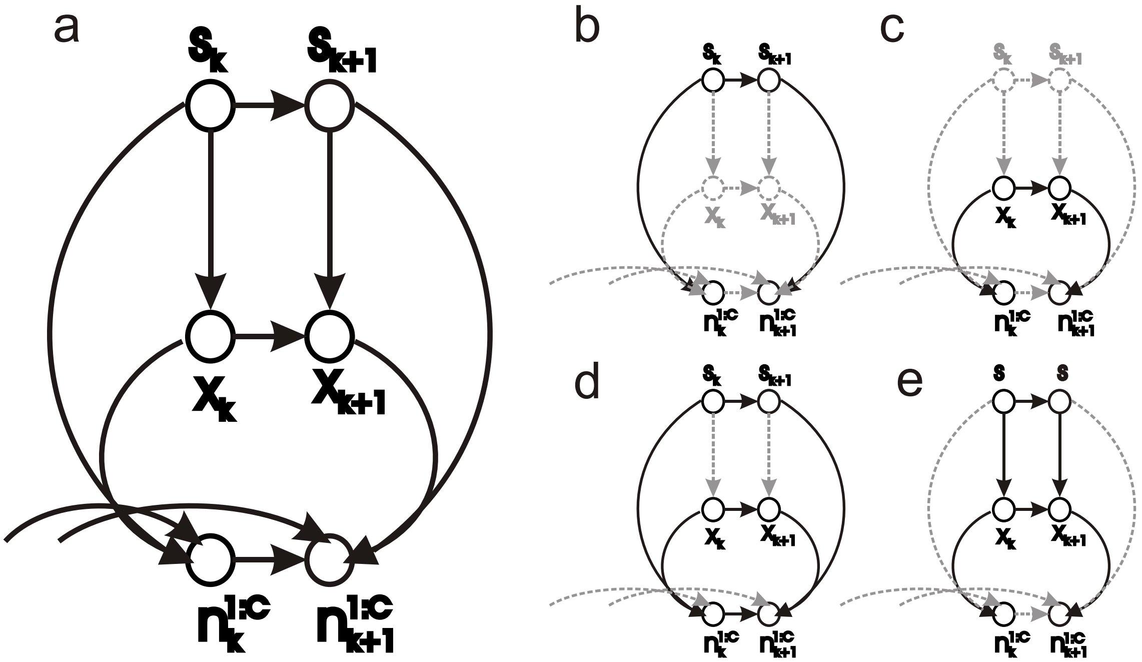

Figure 6.1. Graphical models of the hybrid state space framework and four canonical approaches to estimation for prosthetic devices. Nodes represent random variables, and one probability density is specified for each node conditioned on its parents. Dashed edges are interactions that are possible in the hybrid framework but that are not represented in the canonical approach. **(a)** The hybrid framework represents a specific relationship between the sequence of neural signals (n_k), user-intended continuous states (x_k) and user-intended discrete states (s_k) that encompasses and extends previous approaches (b-e). **(b)** The finite state machine description of cognitive prostheses [6]. **(c)** Free arm movement models [18] and reaching movement trajectory models [22-24, 26-28, 36]. **(d)** The switching observation model [25] for poorly sorted spike trains. **(e)** The mixture of trajectories model [29] for movements to stationary discrete targets.

6.3 Point process models of ensemble spiking activity

Neural activity in the form of action potentials is a sequence of transient spiking events. We first specify an observation model that captures the quality of temporally localized events as well as possible dependencies between neurons in an ensemble.

Signals of this nature are naturally described by point process observation models [31-34]. The crux of the point process description of a single neuron is its conditional intensity function. This is the instantaneous probability of firing as a function of elapsed time t and generally conditioned on continuous-valued signals $x(t)$ discrete-valued signals $s(t)$, and spiking history $H(t)$, where $N(t)$ denotes the total number of spikes generated by the neuron since some arbitary starting time:

$$\lambda(t \mid x(t), s(t), H(t)) = \lim_{\Delta \to 0} \frac{\Pr(N(t+\Delta) - N(t) = 1 \mid x(t), s(t), H(t))}{\Delta} \tag{6.1}$$

We introduce additional notation to accommodate a population of neurons in a discrete time setting. For the k^{th} discrete time step of length δ_k seconds, the conditional intensity of neuron c is represented as λ_k^c, in units of spikes per second. Spiking activity at the k^{th} time step is summarized by a vector $n_k^{1:C} = \left(n_k^1, n_k^2, ..., n_k^C\right)$ of binned spike counts. The c^{th} element of $n_k^{1:C}$ contains the total number of spikes generated by the c^{th} neuron in the respective δ_k-second interval. The observation model for the total spiking activity $n_k^{1:C}$ of each member of an ensemble of C neurons binned at δ_k second intervals is approximated [20] as follows:

$$p(n_k^{1:C} \mid x_k, s_k, H_k) \propto \prod_{c=1}^{C} \exp(n_k^c \log(\lambda_k^c \delta_k) - \lambda_k^c \delta_k) \tag{6.2}$$

where $H_k = \left(n_1^{1:C}, n_2^{1:C}, ..., n_{k-1}^{1:C}\right)$ is the history of spiking activity at step k for the ensemble. This is an approximation in two regards. First, neurons are assumed to be statistically independent conditioned on the history of population activity and current intended device state. This assumption still captures a causal notion of statistical dependence among neurons, that for example, the spiking history of one neuron might affect the present spiking probability of another neuron. Second, the discrete time observation model in (6.2) approximates the exact continuous-time observation model for a point process [37].

6.4 Filtering spikes with the hybrid framework

By combining this observation model and the hybrid state space defined in the previous section, we now derive a specific filter to estimate hybrid device states from ensemble activity that has been modeled as a point process. The continuous-time exact solution to point process filtering with jump-Markov processes is a partial differential equation [38]. The method in this section is one possible approximation.

To develop an estimation procedure that maps spikes to hybrid device states, we looked to the switching Kalman filter [35, 39] which maps Gaussian signals to hybrid device states. We could possibly bin the spike trains (lump them into sequential intervals of time) and then apply a standard switching Kalman filter. However, spike trains that have been binned (lumped into sequential intervals of time) only begin to satisfy the Gaussian assumption as the binsize grows. This results in a tradeoff between the user's control of when an action is supposed to happen versus how it is supposed to happen.

To avoid this tradeoff, we wanted to use the point process observation model (previous section) as a statistical description of spiking that is accurate on a millisecond-by-millisecond time scale [34, 37]. This necessitated the development of a point process filter for hybrid states. Just as there are several approaches to the switching Kalman filter that balance computational complexity and accuracy [39], there are several possible ways to filter spikes for the hybrid framework. Our point process filter is adapted from a mixture-of-Gaussians switching Kalman filter called the Interacting Multiple Model (IMM) [39] that has been a popular choice to balance complexity and accuracy for a variety of Gaussian applications. We summarize the procedure in the box below.

Spike filtering with the hybrid framework in nine steps

Each iteration of the point process hybrid filter involves nine basic steps. The quantities $p(s_k \mid H_{k+1})$ and $p(x_k \mid s_k, H_{k+1})$ come from the previous iteration, where $p(s_1)$ and $p(x_1)$ are used instead for the first iteration. A Gaussian approximation to a probability density on the continuous state x_t is specified by a mean and covariance matrix. A probability mass function on the discrete state s_k is specified by a list of probabilities for each possible value of s_k. See (Supplementary Material, Section 4) for a practical note on numerical issues.

Step 1
Compute $p(s_{k+1} \mid H_{k+1}) = \sum_{s_k} p(s_{k+1} \mid s_k) p(s_k \mid H_{k+1})$

Step 2
Compute $p(s_k \mid s_{k+1}, H_{k+1}) = \dfrac{p(s_{k+1} \mid s_k, H_{k+1}) p(s_k \mid H_{k+1})}{\sum_{s_k} p(s_{k+1} \mid s_k, H_{k+1}) p(s_k \mid H_{k+1})}$

Step 3
Approximate $p(x_k \mid s_{k+1}, H_{k+1}) = \sum_{s_k} p(s_k \mid s_{k+1}, H_{k+1}) p(x_k \mid s_k, H_{k+1})$ with the Gaussian approximation to Mixtures of Gaussians (see Methods, Section B).

Step 4
Calculate the Gaussian approximation to $p(x_{k+1} \mid s_{k+1}, n_{k+1}^{1:C}, H_{k+1})$. Specifically, for each value that s_{k+1} can take on, send $p(x_k \mid s_{k+1}, H_{k+1})$ through one full iteration of a point process filter (see Methods, Section A) with observation equation $p(n_{k+1}^{1:C} \mid x_{k+1}, s_{k+1}, H_{k+1})$ and state equation $p(x_{k+1} \mid x_k, s_{k+1})$. Retain these densities (one Gaussian for each possible value of s_{k+1}) for the next iteration.

Step 5
Calculate $p(n_{k+1}^{1:C} \mid s_{k+1}, H_{k+1}) \approx \dfrac{\left|\Lambda_{k+1|k+1,s_{k+1}}\right|^{1/2}}{\left|\Lambda_{k+1|k,s_{k+1}}\right|^{1/2}} \prod_{c=1}^{C} \exp(n_{k+1}^c \log(\lambda_{k+1}^c \delta_{k+1}) - \lambda_{k+1}^c \delta_{k+1}) \Bigg|_{x_{k+1}=x_{k+1|k,s_{k+1}}}$. Note that $\Lambda_{k+1|k+1,s_{k+1}}$ and $\Lambda_{k+1|k,s_{k+1}}$ are posterior and prediction covariance terms from Step 4 (see also Methods, Section A). This is the Laplace approximation (see Supplementary Material).

Step 6
Calculate $p(s_{k+1} \mid n_{k+1}^{1:C}, H_{k+1}) = \dfrac{p(n_{k+1}^{1:C} \mid s_{k+1}, H_{k+1}) p(s_{k+1} \mid H_{k+1})}{\sum_{s_{k+1}} p(n_{k+1}^{1:C} \mid s_{k+1}, H_{k+1}) p(s_{k+1} \mid H_{k+1})}$. Retain this density for the next iteration.

Step 7
Calculate $p(x_{k+1} \mid n_{k+1}^{1:C}, H_{k+1}) = \sum_{s_{k+1}} p(x_{k+1} \mid s_{k+1}, n_{k+1}^{1:C}, H_{k+1}) p(s_{k+1} \mid n_{k+1}^{1:C}, H_{k+1})$ using the results from Step 4 and Step 6.

Step 8
Choose the discrete and continuous device states for step $k+1$ based on Steps 6 and 7 and your cost function. For example, to approximately minimize average classification error, choose the value of s_{k+1} that maximizes Step 6. To approximately minimize mean squared error, choose the average value of x_{k+1} under the density calculated in Step 7.

Step 9
Return to Step 1 for the next timestep.

Our point process filter derivation (Supplementary Material, Section 1) first manipulates probability densities without specifying their functional form, and later introduces the functional form of the point process observation model given in equation (6.2). The resulting point process filter retains the same flavor as the IMM filter. Just as the IMM filter involves a bank of Kalman filters that run in parallel, our hybrid filter employs a bank of stochastic state point process filters [20] that run in parallel, one for each possible value of the discrete state at a particular timestep. A practical note on numerical issues for implementation is available (Supplementary Material, Section 4).

6.5 Filtering continuous field potentials with the hybrid framework

Continuous field potentials are also viable sources for the control of prosthetic devices, such as with EEG [1], ECoG [2], and LFP [40]. An EEG based device has the potential for wide application because it is completely non-invasive. The ECoG and LFP approaches may allow cheaper and more robust hardware solutions than spike-driven interfaces, because skull screws and coarse electrodes may suffice for these signals where micromachined multiunit arrays are needed to record stable ensemble spiking activity.

The physiological basis of these continuous field potentials is varied and different from that of ensemble spiking activity. Additional research is needed to understand effective training paradigms and hardware design as they pertain to each of these signal sources. However, existing filtering procedures are sufficient to incorporate these signals into the hybrid framework [39]. This is because continuous field potentials have been extensively modeled as Gaussian observation processes, including autoregressive moving average (ARMA) models [30]. As a result, the many types of switching Kalman filter can be applied directly to accommodate these signals into the hybrid framework.

The interacting multiple model (IMM) [39] is the switching Kalman filter that is analogous to the point process filter presented in the previous section. The IMM derivation can be written in almost the same fashion, except that the observation model (6.2) is now Gaussian. Consequently, the IMM procedure is simply the point process hybrid filter procedure of the previous section, but with Kalman filters used in Step 4 instead of point process filters. These are the Gaussian filter equations (6.13) and (6.14) (see Methods, Section A).

6.6 Emerging applications

6.6.1 Application 1: Free arm movement with definitive moving versus stopping

In the control of free movements of a neural prosthetic arm, it would be desireable to bring the arm to rest without explicitly generating a zero-velocity signal. Also, if the person is no longer attending to the arm, it may be safer to bring the arm to rest rather than to allow it to be driven unintentionally. To enable this functionality, define a set of four discrete device states $s_k \in \{(moving, attentive)$, $(moving, inattentive)$, $(stopped, attentive)$, $(stopped, inattentive)\}$ and a continuous device state x_k that corresponds to arm position and velocity. Note that instead of defining two discrete random processes, this approach merges the two into one. The discrete device states now determine the evolution of the continuous arm movement. For $s_k = (moving, inattentive)$, $(stopped, attentive)$, or $(stopped, inattentive)$, the arm velocity in x_k can be safely and gradually damped to zero. In the case where $s_k = (moving, attentive)$, a standard isotropic Gaussian model [18] could be applied with safety constraints on maximum generated velocities and arm compliance. The discrete state transition probabilities would correspond to the expected frequency with which the user would switch between these various modes of operation.

6.6.2 Application 2: Reaching movements with variable arrival time

The reaching movement trajectory models [22-24, 26-28, 36] are currently defined for a fixed, known arrival time. Suppose instead that a more flexible device was desired that could support two arrival times, $T_1 < T_2$, corresponding to a fast reach and a slow reach respectively. We could then define a set of discrete states $s_k \in \{slow, fast\}$ with appropriately permissive state transition probabilities to allow switching between slow and fast reaching. The continuous state trajectory model $p(x_{k+1} \mid x_k, s_{k+1})$ would correspond to a T_1 or T_2 reach state equation conditioned on the discrete state. The T_1 reach state equation could be lengthened with damping dynamics to a Markov chain of the same length as T_2, for consistency. Also, the discrete state transition probability $p(s_{k+1} = fast \mid s_k = slow)$ might be chosen equal to zero for time greater than T_1.

6.6.3 Application 3: Reaching to discrete targets that switch during movement

We now apply the hybrid framework to track a mid-flight change in the desired target. In the switching target reach task, the subject is required to reach to targets with a prosthetic arm driven by ensemble spiking activity from primary motor cortex (MI). Each reach must be completed within 2 seconds in a two dimensional plane from the origin to one of eight targets arranged evenly on a circle of 0.25 meters radius. In addition, the target changes once during the course of the movement, requiring the user to make a corrective maneuver to the new target location. The switch time, unknown to the user, is drawn uniformly between 0.2 and 1.2 seconds post-movement-onset. These parameters are chosen to explore reaching movements at a realistic spatial scale for humans, while maintaining peak arm velocities that are comparable to those studied in related primate electrophysiology experiments of MI [41-43].

How can the hybrid framework solve the switching target reach task? We begin by defining the continuous variable x_k as the arm state and the discrete variable s_k as the target identity from a set of R targets on a 2-dimensional workspace:

$$x_k = \begin{bmatrix} x\ position\ coordinate\ at\ timestep\ k \\ y\ position\ coordinate\ at\ timestep\ k \\ x\ velocity\ coordinate\ at\ timestep\ k \\ y\ velocity\ coordinate\ at\ timestep\ k \end{bmatrix} \quad , \qquad s_k \in \{1, 2, ..., R\} \tag{6.3}$$

For this example, consider neural observations n_k discribed as binned spikes of a point process (see previous section "Filtering on Hybrid Systems: Point Process Observations"). The essential structure of this hybrid state space is depicted by the mixture of trajectories model (Figure 6.1e). To support switching targets, this static target diagram is altered by indexing the target s with time as in the switching observation model (Figure 6.1d) [25].

Next, we specify the conditional densities corresponding to each edge. The density $p(s_{k+1} | s_k)$ is defined by a state transition matrix M :

$$M_{i,j} = p(s_{k+1} = i | s_k = j) \tag{6.4}$$

This notation means that the entry in the i^{th} row and j^{th} column of M corresponds to $p(s_{k+1} = i | s_k = j)$.

The density $p(x_{k+1} | x_k, s_{k+1})$ constrains the path of a reaching movement for any given target s_{k+1}. This conditional density can be obtained from any of several reaching movement trajectory models [22, 23, 27, 28, 36], directed specifically to the target location corresponding to s_{k+1}. In this example, we use the standard (unaugmented) reach state equation detailed in [22, 23] based on the following free movement state equation:

$$x_{k+1} = Ax_k + w_k \tag{6.5}$$

The point process observation model (6.2) that describes $p(n_k^{1:C} \mid x_k)$ is specified by a discrete-time conditional intensity function λ_k^c for each neuron c. In this example, we choose a conditional intensity adapted from a model of primary motor cortex [42] .

$$\lambda_k^c = \exp(\beta_0^c + \beta_1^c (v_x^2 + v_y^2)^{1/2} \cos(\theta - \beta_2^c)) \tag{6.6}$$

$$= \exp(\beta_0 + \alpha_1 v_x + \alpha_2 v_y) \tag{6.7}$$

where v_x and v_y are the velocity components of x_k in (6.3). Here, we assume that any lag between neural activity and the user's intentions is known and has been corrected to allow for the zero-lag indexing used above. In practice, this lag can be estimated as another model parameter.

The parameters of the observation model $p(n_k^{1:C} \mid x_k)$ can be tuned using point process adaptive filtering [20] that also tracks changes due to neural plasticity. The parameters of the trajectory model in $p(x_{k+1} \mid x_k, s_{k+1})$ and $p(s_{k+1} \mid s_k)$ can be optimized *a priori* to reflect the types and frequency of behaviors that the neural prosthesis expects to support. Alternatively, adaptive methods will need to be developed to track the usage statistics of the device and adjust the trajectory model accordingly. In this example, we give our various competing filters an equal footing by providing them the actual trajectory and observation model parameters where applicable. A caveat is the state transition matrix M. In free movement and mixture of trajectories estimation, this parameter is nonexistant, or equivalently, equal to the $R \times R$ identity matrix I. For the hybrid framework, this parameter can be tuned to the expected frequency of target switches. We found that performance was relatively insenstive to a range of choices between $0.9I$ $0.99I$ but changed substantially for $M = I$. (Although 0.99 is close to 1, this difference is geometrically magnified by successively multiplying 0.99 over multiple timesteps.)

With the conditional densities specified, we can now use the hybrid point process filtering framework to drive the prosthetic device with ensemble spiking activity from motor cortex. We compare the performance of the hybrid framework against free movement estimation and the mixture of trajectories model in a simulated analysis of the switching target reach task. The free movement estimation procedure is implemented using a standard point process filter. This is mathematically equivalent to our hybrid framework where each target is given infinite uncertainty. The mixture of trajectories estimation method reported in [29] is implemented using the same reach state equation that our hybrid filter uses to provide equal grounds for comparison. This is mathematically equivalent to the hybrid filter with state transition matrix $M = I$.

We also examine the effect of premovement instructed delay period activity that may be available to the prosthetic device. Such activity is known to provide information about the desired target in posterior parietal cortex [44], premotor cortex [45], frontal cortex [46], and other brain regions. Premovement target information is easily incorporated into the mixture of trajectories model and hybrid filter by specifying a non-uniform initial posterior density on the target states $p(s_1)$. We use one fixed moderately informative non-uniform posterior density (see parameter table) to simulate this premovement target information.

These filtering procedures were compared in a simulated version of the switching target reach task. The simulation comprised two stages. First, the subject's desired arm movement was generated based on the reach state equation [22, 23] which is related to the stochastic optimal control model [28, 47, 48]. Second, the corresponding ensemble spiking activity from primary motor cortex (MI) was simulated based on equation (6.6), a velocity-tuned point process model of MI spiking activity [37, 42].

The subject's arm movement was governed by same unaugmented reach state equation [22] used above to define $p(x_{k+1} \mid x_k, s_{k+1})$ in the hybrid framework. Arm movement at any given time step followed the reach state equation corresponding to the current target with low target uncertainty (see parameter table). The constants q, r, and p in that table refer

Table: Parameters

(a) Receptive field parameters of c^{th} M1 neuron

Parameter	Value
β_0^c	2.28
β_1^c	4.67 sec./m
β_2^c	Drawn uniformly from [-π,π]

(b) Reach state equation parameters

Parameter	Value
Reach distance	0.25 m
Target Positions (degrees)	$(45, \quad 90, \quad 135, \quad 180, \quad 225, \quad 270, \quad 315, \quad 360)$
Time step	0.01 sec.
Noise covariance (q)	$1\text{x}10^{-4}$ m^2
Reach duration	2 sec.
Target position uncertainty (r)	$1\text{x}10^{-6}$ m^2
Target velocity uncertainty (p)	$1\text{x}10^{-6}$ m^2

(c) Other motor task parameters

Parameter	Value
$(p(s_1 = 1), \quad p(s_1 = 2), \quad \ldots \quad p(s_1 = 8))$	$(.6, \quad .15, \quad .02, \quad .02, \quad .02, \quad .02, \quad .02, \quad .15)$
Switch times (sec.)	$(.2, \quad .4, \quad .6, \quad .8, \quad 1, \quad 1.2)$
Ensemble sizes (# neurons)	$(9, \quad 16, \quad 25, \quad 36, \quad 49, \quad 64, \quad 81)$
Randomized trials per data point (Fig. 4,5)	100

to specific entries of the diagonal matrices for noise covariance and target uncertainty specified previously [22]. The target itself was allowed to switch once during the course of the movement. The target switch time was assigned at random, uniformly from a discrete set of possible times between 0.2 and 1.2 seconds post-movement-onset, spaced at 0.2 seconds.

Because ensemble spiking is governed by conditional independence (see equation (6.2)), the spiking activity of each cell could be generated separately. To generate the spike train of a given cell, the arm trajectory was first passed through the point process model in equation (6.6). The conditional intensity generated by the point process model of each neuron was then used to produce ensemble spiking activity based on the time rescaling theorem [34].

For each neuron c, model parameters β_0^c and β_1^c were chosen (see parameter table) to reflect typical background firing rate and depth of modulation for primate MI neurons during instructed-delay center-out reaching movements [37]. The model parameter β_2^c was drawn randomly over $[-\pi,\pi]$ to ensure that preferred directions were uniformly represented over all angles. Neurons in this simulated MI ensemble exhibited background firing rates of 10 spikes/sec., and firing rates of 24.9 spikes/sec. at a speed of 0.2 m/sec. in the preferred direction.

In total, five filtering procedures were compared in the simulated switching target reach task: free movement estimation, mixture of trajectory estimation, and hybrid filtering, the last two methods being evaluated with and without premovement target information. Figures 6.2-5 provide a comprehensive view of the ability of these filtering procedures to convert MI spiking activity into reaching movements to switching targets. Figures 6.2 and 3 show sample trajectories driven by ensemble spiking activity under the various estimation procedures for a population of 25 neurons with a target switch at 1 second post-movement-onset. Figures 6.4 and 5 characterize how filter performance scales with ensemble size and target switch time for each of these procedures.

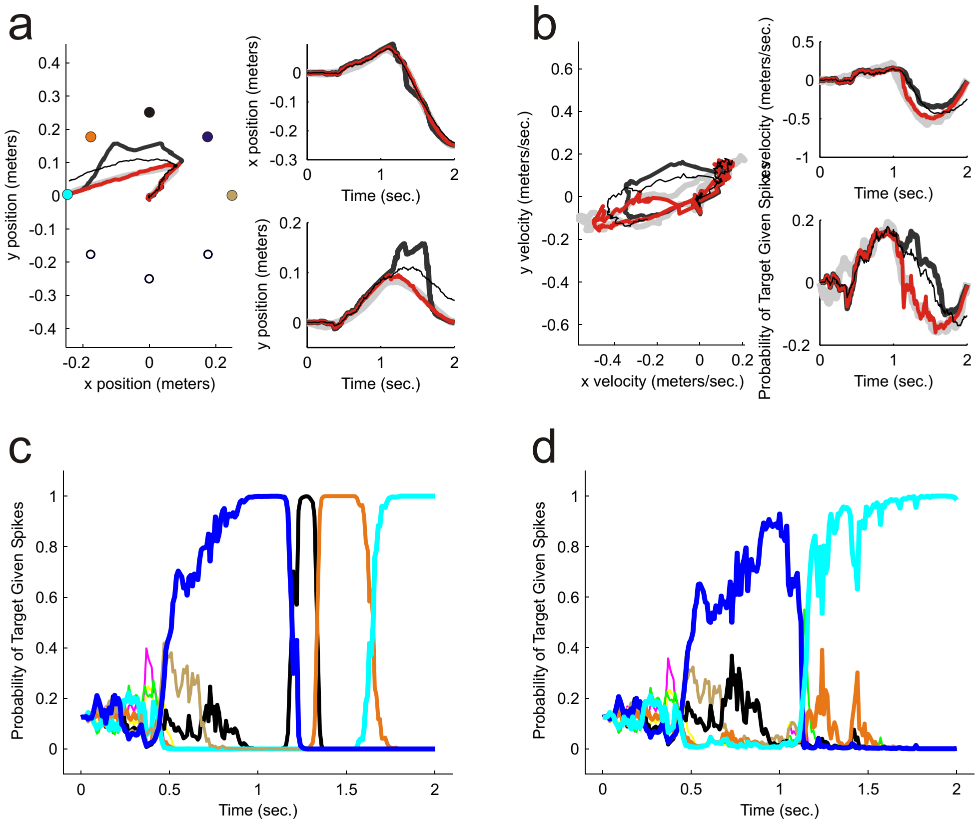

Figure 6.2. Decoding results without premovement target information from one trial of the simulated switching target motor reaching task on a 2-dimensional plane using 25 motor cortical neurons. **(a)** Position trajectories, including the desired arm path (light gray), hybrid filter (red), mixture of trajectories model (dark gray), and free movement estimation (thin black). **(b)** Velocity trajectories with the same color scheme. **(c)** Probability of each target given ensemble spiking as the reach pogresses, as determined by the mixture of trajectories model and **(d)** the hybrid filter. Colors in (c) and (d) correspond to these targets: the primary target at 45 degrees (blue), final target at 180 degrees (cyan), and the neighbors at 0 degrees (gold), 90 degrees (black) and 135 degrees (orange).

Sample decoding results from one trial without premovement target information (Figure 6.2) show that the hybrid framework combines the strengths of free movement estimation and the mixture of trajectories model. By incorporating target information, the hybrid framework and mixture of trajectories estimates drive the prosthetic arm to rest at the desired target location, while free movement estimation leaves the arm displaced from the target and still moving at the 2 second mark. However, this same target information also causes the mixture of trajectories estimate to pull towards each passing target late in the reach (Figure 6.1a). This "gravity effect" is reflected in the target probabilities under the mixture of trajectories model (Figure 6.1c). In the second half of the reach, the current heading causes the passing targets (black and red lines) to quickly become highly likely, drawing the trajectory estimate towards those corresponding target locations. The hybrid framework overcomes this problem because it anticipates that targets may switch. By choosing the state transition matrix $M = 0.99I$, the target densities (Figure 6.1d) decay with time, and additional supporting neural activity is required to drive the probability of any given target to dominate the others. This mollifies the gravity effect of the mixture of trajectories model.

The hybrid filter also handles premovement target information differently from the mixture of trajectories model (Figure 6.3). With the premovement information, the first target's probability under the mixture of trajectories model (blue line, Figure 6.3c) approaches certainty faster than before (Figure 6.2c). However, single trial decoding results (Figure 6.3a and 3b) show that the mixture of trajectories estimate appears to persist to the original target location even when the desired trajectory has begun to reorient to the new target. This is also seen in the target probabilities (Figure 6.3c) where the first target (blue) dominates 200 milliseconds beyond the time of the target switch. In contrast, the hybrid framework incorporates the target information early in the reach but progressively "forgets" or downweight its influence because it anticipates the possibility of a target switch, again by using $M = 0.99I$. The free movement estimate does not incorporate premovement information.

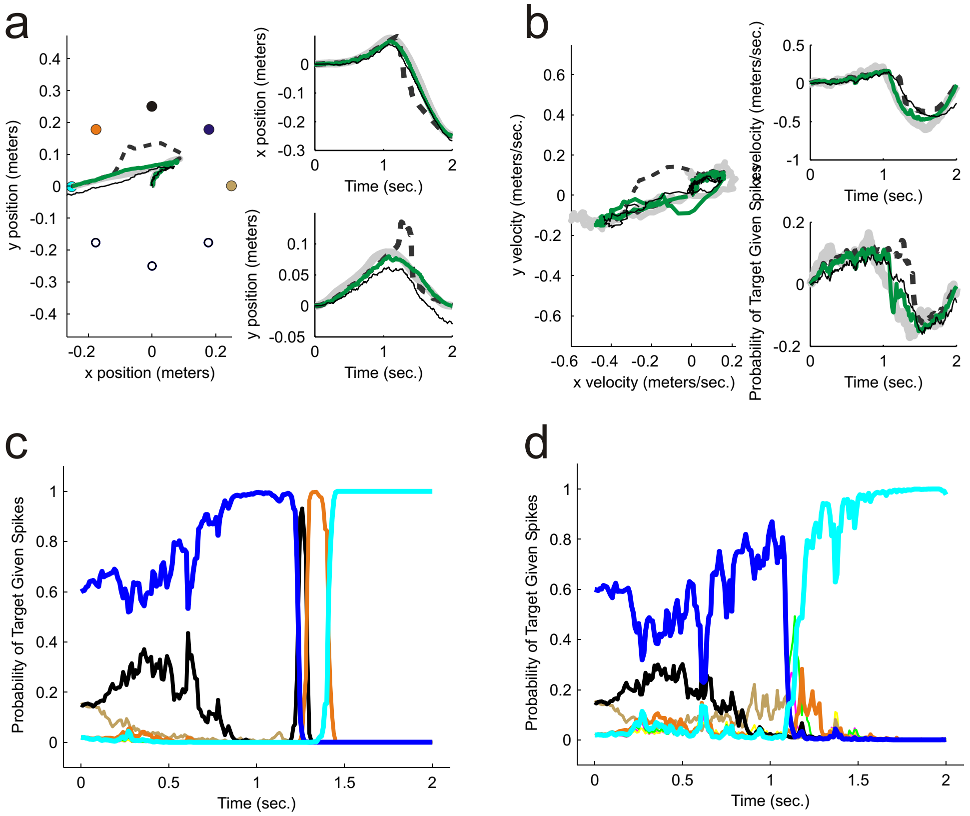

Figure 6.3. Decoding results with premovement target information from one trial of the simulated switching target motor reaching task on a 2-dimensional plane using 25 motor cortical neurons. **(a)** Position trajectories, including the desired arm path (light gray), hybrid filter (green), mixture of trajectories model (dark gray), and free movement estimation (thin black). **(b)** Velocity trajectories with the same color scheme. **(c)** Probability of each target given ensemble spiking as the reach pogresses, as determined by the mixture of trajectories model and **(d)** the hybrid filter. Colors in (c) and (d) follow Figure 2.

We next examined filter performance over a wide range of ensemble sizes, ranging from 15 to 80 neurons. Root mean squared (RMS) error was evaluated in two ways: averaged over the entire trajectory (Figures 6.4 a,b) and over the endpoint at the 2 second mark (Figures 6.4c and d). Additionally, we examined the fidelity of position tracking (Figures 6.4 a,c) and velocity tracking (Figure 6.4b, d) separately. RMS error decreases for all five methods with larger ensemble sizes. This is consistant with Bayes Rule, which predicts that the RMS error of these various methods will converge for large enough population sizes.

Trajectory RMS errors are typically smaller than endpoint RMS errors because trajectories begin with the accurate initial condition and accumulate error with time. All methods appear to perform equally well in endpoint error except free movement estimation which does not incorporate the discrete target locations. Moreover, endpoint error appears to level out faster than trajectory error. This is likely due to the fact that just a few MI neurons are needed to make an accurate target classification, and once the accurate classification is made, the mixture of trajectories and hybrid framework methods will drive the prosthetic arm to rest at that target.

Premovement target information appears to provide a slight or insignificant improvement, but this is largely due to the moderate information provided by our choice of initial target prior. Higher fidelity premovement target information will likely make overshooting more pronounced in mixture of trajectories estimation and decrease RMS error in the first half of the reach generated by hybrid estimation.

Earlier target switches are easier to track for all methods than later target switches (Figure 6.5) for a population of 25 neurons. Later switch times require faster velocity corrections, causing trajectory RMS error to rise across all methods (Figures 6. 5 a,b). Trajectory RMS error accumulates rapidly with later switch time for the mixture of trajectories model which lags in reorienting the arm movement, unlike hybrid estimation which anticipates switching and reorients quickly.

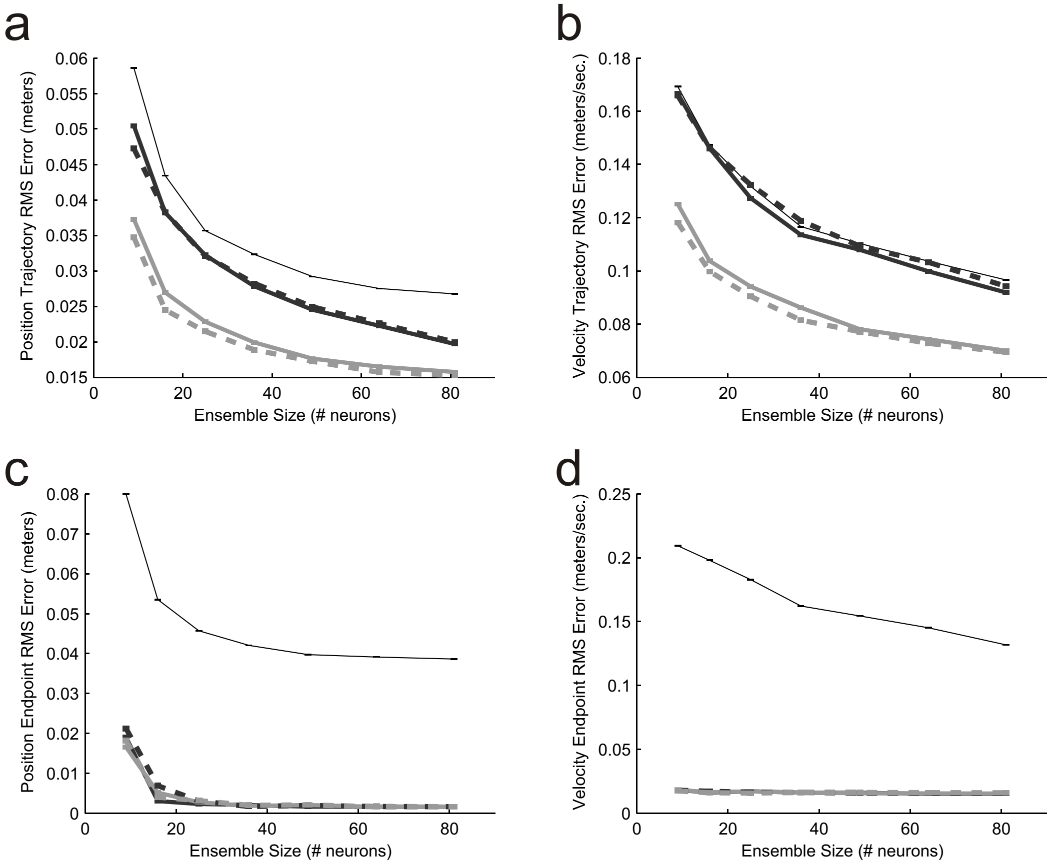

Figure 6.4. Various root mean squared (RMS) error peformance metrics versus ensemble size for free movement estimation (thin black), mixture of trajectories model (solid dark gray), hybrid filter (solid light gray), and versions of the latter two filters with premovement target information (dashed lines). Switch times are drawn uniformly from the set {.2, .4, .6, .8, 1, 1.2}in units of seconds. Error bars represent standard error of the mean across one hundred randomized trials for each mean. **(a)** RMS error averaged over the entire position trajectory. **(b)** RMS error averaged over the entire velocity trajectory. **(c)** RMS error averaged only over the endpoint position. **(d)** RMS error averaged only over the endpoint velocity.

Endpoint errors (Figures 6.5 c,d) under mixture of trajectories and hybrid estimation are largely insensitive to switch time, in contrast to free movement estimation. For mixture of trajectories and hybrid estimation, neural observations after the switch are sufficient to classify the target correctly, and because these latter methods incoporate the set of target locations, the prosthesis movement can reliably converge to the target.

Receiving information from the premovement activity that results in an incorrect maximum likelihood target classification is comparable to a zero second switch time, because in both cases, premovement activity initially push path estimates towards the wrong final target. This represents the easiest case for tracking switching movements, because subsequent neural activity over the full interval of reach time is available to correct estimates towards the final target. In later switches, shorter intervals of neural activity are available to redirect the arm movement. This is the regime where hybrid estimation shows marked improvement over the mixture of trajectories approach.

The simulation predicts that performance breaks down for all methods under moderate ensemble sizes for very late switches, where the target can no longer be reliably identified and high velocity corrective movements must be tracked. A more subtle trend (Figures 6.5 a,b) shows that free movement estimation performs substantially worse than the mixture of trajectories model for early switch times but slightly better in very late switch times. These very late switch times make the overshoot and gravity effects of the mixture of trajectories model so pronounced that resulting trajectory estimates accumulate more RMS error than even the free movement model.

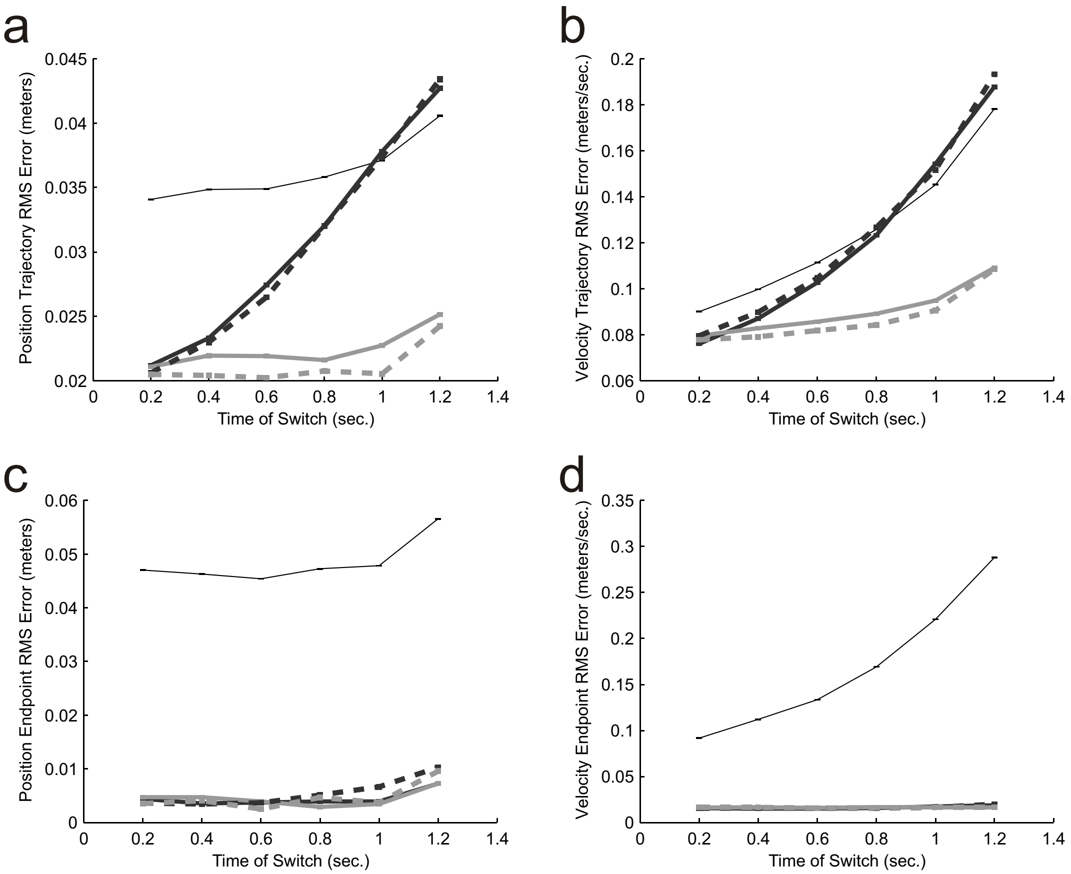

Figure 6.5. Various root mean squared (RMS) error peformance metrics versus the time post-movement onset at which the target switches, for free movement estimation (thin black), mixture of trajectories model (solid dark gray), hybrid filter (solid light gray), and versions of the latter two filters with premovement target information (dashed lines). Ensemble size is fixed at 25 neurons. Error bars represent standard error of the mean across one hundred randomized trials for each mean. **(a)** RMS error averaged over the entire position trajectory. **(b)** RMS error averaged over the entire velocity trajectory. **(c)** RMS error averaged only over the endpoint position. **(d)** RMS error averaged only over the endpoint velocity.

6.7 Discussion

We have introduced a unified approach for the design of filters for prosthetic devices. By using this technique, we can map spikes and continuous field potentials to estimates of the user's intention for a wide array of neural prosthetic device applications. The technique draws on Bayesian filter theory to generalize the dominant approaches to filter design in neural prosthetic devices [1, 3-7, 17-19, 22-29, 36, 49]. Three emerging applications are proposed. The hybrid framework is comprehensively evaluated in a simulated motor reaching task.

For both the hybrid point process filter and the IMM Switching Kalman Filter for Gaussian observation models, the number of operations at time step k scales with $|S_k|$, the number of values that a discrete state variable can take on. This is because the posterior density on the discrete state is nonparametric and the posterior density on the continuous state is represented as a mixture of $|S_k|$ Gaussians. The particle filter, a Monte Carlo approach, would increase the fidelity the posterior density at the expense of increased computational cost. Ultimately, the way in which the posterior density is represented will depend on the cost of computation versus device performance in any specific application.

As shown in the previous section, the hybrid framework accomodates multiple discrete random processes by condensing them into one. Unfortunately, n discrete random variables, each with p possible values at step k, results in a condensed random variable with $|S|=n^p$. Fortunately, filtering on the hybrid framework can be parallelized fairly directly. This means that even with large $|S_k|$ the device can be controlled in real time if the hardware supports parallel computations. Parallelizing a digital hardware implementation may not necessarily save energy, but could require a slower clock speed.

In many applications however, the number of discrete states can be kept small by using context. Context means that the space of device states is restricted at any given step in a way that still allows the user to eventually reach the desired device state. Consider how you organize files on your computer. By arranging your files in a sequence of subdirectories, you make it easy to scan through the list of files at each step. By placing all your files on the desktop, you are forced to select your file from a very large list, even though the file is just one mouseclick away.

Looking forward, we expect to draw extensively on the rich field of dynamic bayesian networks to address future applications. Prototyping is needed to determine the best computation/accuracy tradeoff for specific prosthetic devices. Learning and real time sensory feedback (visual, somatosensory, auditory) must also be considered in developing algorithms that define the prosthetic interface. Associated technologies like computer vision and robotic control can be integrated with the hybrid framework to enhace real-world performance measures.

Finally, estimation with a minimum average cost criterion is not the only approach to formally describing the prosthetics problem. Future work will explore stochastic control, heirarchical design architectures, and other themes in systems design to achieve the increased performance in practical tasks that is necessary to benefit the full spectrum of limited motor function, from locked-in syndrome to single arm amputation.

6.8 Methods

6.8.1 (Section A) Approximate point process filter for Gauss-Markov process (discrete-time)

The Gaussian approximation to the posterior density with a Taylor series expansion about the prediction mean is employed in the following filter equations [20]. Consider a Gauss-Markov trajectory model

$$p(x_{k+1} \mid x_k) \sim N(F_k x_k + b_k, Q_k) \tag{6.8}$$

A point process observation model is specified for an ensemble of C neurons. The conditional intensity function of the c^{th} neuron, denoted λ_k^c, may depend on H_k and x_k. For the k^{th} timestep and c^{th} neuron, n_k^c spikes arrive in a δ_k time interval.

The prediction density mean $x_{k+1|k}$ and covariance $\Lambda_{k+1|k}$ are:

$$x_{k+1|k} = F_k x_{k|k} + b_k \tag{6.9}$$

$$\Lambda_{k+1|k} = F_k \Lambda_{k|k} F_k^{'} + Q_k \tag{6.10}$$

The posterior density covariance $\Lambda_{k+1|k+1}$ and mean $x_{k+1|k+1}$ are:

$$(\Lambda_{k+1|k+1})^{-1} = (\Lambda_{k+1|k})^{-1} + \sum_{c=1}^{C} \left[\left(\frac{\partial \log \lambda_k^c}{\partial x_k} \right) \left[\lambda_k^c \delta_k \right] \left(\frac{\partial \log \lambda_k^c}{\partial x_k} \right) - \left(n_k^c - \lambda_k^c \delta_k \right) \frac{\partial^2 \log \lambda_k^c}{\partial x_k} \right]_{x_{k+1|k}} \tag{6.11}$$

$$x_{k+1|k+1} = x_{k+1|k} + \Lambda_{k+1|k+1} \sum_{c=1}^{C} \left[\left(\frac{\partial \log \lambda_k^c}{\partial x_k} \right)^{'} \left(n_k^c - \lambda_k^c \delta_k \right) \right]_{x_{k+1|k}} \tag{6.12}$$

Consider instead, an array of C neural signals $\underline{n}_k = \left[n_{k+1}^1, n_{k+1}^2, \ldots, n_{k+1}^C \right]^{'}$ described by a Gaussian observation model (such as EEG) with mean $D_k x_k + f_k(H_k)$ and variance W_k. Here, x_k is a $J \times 1$ vector of continuous states, D_k is a $C \times J$ matrix that may depend on s_k, and $f_k(s_k, H_k)$ is a function that maps neural history to a $C \times 1$ vector, such as with

ARMA models. The posterior density covariance and mean are then given by the standard Kalman filter equations [50]:

$$\Lambda_{k+1|k+1} = \Lambda_{k+1|k} - \Lambda_{k+1|k} D'_{k+1} (D_{k+1} \Lambda_{k+1|k} D'_{k+1} + R_{k+1})^{-1} D_{k+1} \Lambda_{k+1|k} \quad (6.13)$$

$$x_{k+1|k+1} = x_{k+1|k} + \Lambda_{k+1|k} D'_{k+1} (D_{k+1} \Lambda_{k+1|k} D'_{k+1} + R_{k+1})^{-1} (\underline{n}_{k+1} - D_{k+1} x_{k+1|k} - f_{k+1}(s_{k+1}, H_{k+1})) \quad (6.14)$$

The probability density in Step 5 of the point process hybrid filter (see Box above) is then replaced by:

$$p(n_{k+1}^{1:C} \mid s_{k+1}, H_{k+1}) \sim N\left(D_{k+1} x_{k+1|k} + f_{k+1}(s_{k+1}, H_{k+1}), D_{k+1} \Lambda_{k+1|k} D'_{k+1} + R_{k+1} \right) \quad (6.15)$$

in order to correspond to the Interacting Multiple Model (IMM) approach to switching Kalman filters [39].

6.8.2 (Section B) Gaussian approximation to Mixture of Gaussians

Consider a distribution composed of the weighted average of R multidimensional Gaussians

$$p(x) = \sum_{i=1}^{R} d_i N(x; \mu_i, \Lambda_i) \quad (6.16)$$

with weights d_i, and where $N(x; \mu_i, \Lambda_i)$ denotes the Gaussian probability density function with mean μ_i, and covariance Λ_i.

The following standard approximation [39] is obtained by moment matching (calculating the mean and covariance of $p(x)$):

$$p(x) \approx N(x; m, K) \quad (6.17)$$

where

$$m = \sum_{i=1}^{R} d_i \mu_i \quad (6.18)$$

$$K = \sum_{i=1}^{R} d_i \times [\Lambda_i + (\mu_i - m)(\mu_i - m)'] \quad (6.19)$$

6.9 Supplementary Material

6.9.1 (Section 1) Derivation of a Point Process Hybrid Filter to Map Spikes to Hybrid Prosthetic Device States

For the k^{th} discrete timestep, define the user-intended continuous state x_k, discrete state s_k, and the ensemble spiking activity of all C neurons $n_k^{1:C}$. The history of ensemble spiking at timestep k is given by $H_k = \left(n_1^{1:C}, n_2^{1:C}, ..., n_{k-1}^{1:C}\right)$. Define the observation model $p(n_{k+1}^{1:C} \mid x_{k+1}, s_{k+1}, H_{k+1})$ that represents the relationship between user intentions and spiking activity. Define the trajectory model $p(x_{k+1} \mid x_k, s_{k+1})$ and discrete state transition density $p(x_{k+1} \mid x_k, s_{k+1})$ that reflect the distribution of intentions that the user is expected to request over time.

In this section, we seek a recursive method to obtain $p(x_{k+1}, s_{k+1} \mid n_{k+1}^{1:C}, H_{k+1})$ from $p(x_k, s_k \mid n_k^{1:C}, H_k)$ and $n_{k+1}^{1:C}$. This constitutes the point process hybrid filtering procedure.

For our specific hybrid state space in Figure 1A,

$$p(x_{k+1}, s_{k+1} \mid n_{k+1}^{1:C}, H_{k+1}) = p(x_{k+1} \mid s_{k+1}, n_{k+1}^{1:C}, H_{k+1})\, p(s_{k+1} \mid n_{k+1}^{1:C}, H_{k+1}) \tag{6.19}$$

This implies that our problem is equivalent to obtaining $p(x_{k+1} \mid s_{k+1}, n_{k+1}^{1:C}, H_{k+1})$ and $p(s_{k+1} \mid n_{k+1}^{1:C}, H_{k+1})$ from $p(x_k \mid s_k, n_k^{1:C}, H_k)$, $p(s_k \mid n_k^{1:C}, H_k)$, and $n_{k+1}^{1:C}$.

Note that

$$p(x_{k+1} \mid n_{k+1}^{1:C}, H_{k+1}) = \sum_{s_{k+1}} p(x_{k+1} \mid s_{k+1}, n_{k+1}^{1:C}, H_{k+1})\, p(s_{k+1} \mid n_{k+1}^{1:C}, H_{k+1}) \tag{6.20}$$

We now calculate $p(x_{k+1} \mid s_{k+1}, n_{k+1}^{1:C}, H_{k+1})$ using equations (6.21)-(6.26) and calculate $p(s_{k+1} \mid n_{k+1}^{1:C}, H_k)$ using equation (6.27).

Observe that

$$p(x_{k+1} \mid s_{k+1}, n_{k+1}^{1:C}, H_{k+1}) = \frac{p(n_{k+1}^{1:C} \mid x_{k+1}, s_{k+1}, H_{k+1})\, p(x_{k+1} \mid s_{k+1}, H_{k+1})}{p(n_{k+1}^{1:C} \mid s_{k+1}, H_{k+1})} \tag{6.21}$$

where $p(x_{k+1} \mid s_{k+1}, H_{k+1})$ is the prediction density given by the Chapman-Kolmogorov equation:

$$p(x_{k+1} \mid s_{k+1}, H_{k+1}) = \int_{x_k} p(x_{k+1} \mid x_k, s_{k+1}, H_{k+1}) p(x_k \mid s_{k+1}, H_{k+1}) dx_k \tag{6.22}$$

Equations (6.21) and (6.22) comprise one step of a filter on $p(x_k \mid s_{k+1}, H_{k+1})$ with the observation model $p(n_{k+1}^{1:C} \mid x_{k+1}, s_{k+1}, H_{k+1})$ and trajectory model $p(x_{k+1} \mid x_k, s_{k+1}, H_{k+1}) = p(x_{k+1} \mid x_k, s_{k+1})$. For computational simplicity, we approximate both the trajectory model and posterior density $p(x_{k+1} \mid s_{k+1}, n_{k+1}^{1:C}, H_{k+1})$ to be Gaussian. Such a filter (reproduced under Methods Section A) is developed in [20] for point processes using a Taylor expansion about the prediction density mean rather than the posterior density mean employed in [50].

The density $p(x_k \mid s_{k+1}, H_{k+1})$ is obtained by

$$p(x_k \mid s_{k+1}, H_{k+1}) = \sum_{s_k} p(s_k \mid s_{k+1}, H_{k+1})\, p(x_k \mid s_k, s_{k+1}, H_{k+1}) \tag{6.23}$$

This density is a mixture of Gaussians that is approximated by one Gaussian density using a standard moment-matching formula given in Methods Section B.

The first density in the summation (6.23) is calculated as follows:

$$p(s_k \mid s_{k+1}, H_{k+1}) = \frac{p(s_{k+1} \mid s_k, H_{k+1})\, p(s_k \mid H_{k+1})}{p(s_{k+1} \mid H_{k+1})} \tag{6.24}$$

where

$$p(s_{k+1} \mid H_{k+1}) = \sum_{s_k} p(s_{k+1} \mid s_k)\, p(s_k \mid H_{k+1}) \tag{6.25}$$

Here, $p(s_{k+1} \mid s_k)$ is the discrete state transition density, and $p(s_k \mid H_{k+1})$ is the posterior density on the discrete state, given in the previous iteration.

The second density in the summation (6.23) is given by a quantity retained from the previous step:

$$p(x_k \mid s_k, s_{k+1}, H_{k+1}) = p(x_k \mid s_k, H_{k+1}) \tag{6.26}$$

This statement is verified in Section 2 below.

We now calculate $p(s_{k+1} \mid n_{k+1}^{1:C}, H_{k+1})$ in equation (6.20) using the following relation:

$$p(s_{k+1} \mid n_{k+1}^{1:C}, H_{k+1}) = \frac{p(n_{k+1}^{1:C} \mid s_{k+1}, H_{k+1})\, p(s_{k+1} \mid H_{k+1})}{p(n_{k+1}^{1:C} \mid H_{k+1})} \tag{6.27}$$

Equation (6.25) calculates $p(s_{k+1} \mid H_{k+1})$. The density $p(n_{k+1}^{1:C} \mid s_{k+1}, H_{k+1})$ is given by the following integral.

$$p(n_{k+1}^{1:C} \mid s_{k+1}, H_{k+1}) = \int_{x_{k+1}} p(n_{k+1}^{1:C} \mid s_{k+1}, x_{k+1}, H_{k+1})\, p(x_{k+1} \mid s_{k+1}, H_{k+1}) dx_{k+1} \tag{6.28}$$

An approximation to this integral for point process observations is given by Laplace approximation as detailed in Section 3 below. Finally, $p(n_{k+1}^{1:C} \mid H_{k+1})$ is a normalizing factor obtained by summing the numerator over all possible values of s_{k+1}.

6.9.2 (Section 2) Corollary

Verify equation (6.26), that $p(x_k \mid s_k, s_{k+1}, H_{k+1}) = p(x_k \mid s_k, H_{k+1})$:

$$\begin{aligned} p(x_k \mid s_k, s_{k+1}, H_{k+1}) &= \frac{p(x_k, s_{k+1} \mid s_k, H_{k+1})}{p(s_{k+1} \mid s_k, H_{k+1})} \\ &= \frac{p(s_{k+1} \mid x_k, s_k, H_{k+1})\, p(x_k \mid s_k, H_{k+1})}{p(s_{k+1} \mid s_k, H_{k+1})} \end{aligned} \tag{6.29}$$

From Figure 1A, observe that

$$p(s_{k+1} \mid x_k, s_k, H_{k+1}) = p(s_{k+1} \mid s_k, H_{k+1}) \tag{6.30}$$

Thus, (6.29) and (6.30) imply that

$$p(x_k \mid s_k, s_{k+1}, H_{k+1}) = p(x_k \mid s_k, H_{k+1}) \tag{6.31}$$

■

6.9.3 (Section 3) Laplace approximation of $p(n_{k+1}^{1:C} \mid s_{k+1}, H_{k+1})$

This section derives the Laplace approximation of equation (6.28), repeated below for convenience:

$$p(n_{k+1}^{1:C} \mid s_{k+1}, H_{k+1}) = \int_{x_{k+1}} p(n_{k+1}^{1:C} \mid s_{k+1}, x_{k+1}, H_{k+1})\, p(x_{k+1} \mid s_{k+1}, H_{k+1}) dx_{k+1} \tag{6.32}$$

Define

$$h(x_{k+1}, n_{k+1}^{1:C}) = \log[p(n_{k+1}^{1:C} \mid s_{k+1}, x_{k+1}, H_{k+1})\, p(x_{k+1} \mid s_{k+1}, H_{k+1})] \tag{6.33}$$

The Laplace approximation to (6.32) is given by:

$$
\begin{aligned}
p(n_{k+1}^{1:C} \mid s_{k+1}, H_k) &\approx (2\pi)^{m/2} \left| -\nabla_{x_{k+1}}^2 h(x_{k+1}, n_{k+1}^{1:C}) \right|^{-1/2} p(n_{k+1}^{1:C}, x_{k+1} \mid s_{k+1}, H_{k+1}) \Big|_{x_{k+1}=x_0} \\
&= (2\pi)^{m/2} \left| -\nabla_{x_{k+1}}^2 h(x_{k+1}, n_{k+1}^{1:C}) \right|^{-1/2} p(n_{k+1}^{1:C} \mid x_{k+1}, s_{k+1}, H_{k+1}) \, p(x_{k+1} \mid s_{k+1}, H_{k+1}) \Big|_{x_{k+1}=x_0}
\end{aligned}
\tag{6.34}
$$

where the mode x_0 maximizes $p(n_{k+1}^{1:C} \mid s_{k+1}, x_{k+1}, H_{k+1}) \, p(x_{k+1} \mid s_{k+1}, H_{k+1})$ for a given $n_{k+1}^{1:C}$.

Approximate the mode as in [20] using a prediction density, in this case given by

$$x_0 \approx x_{k+1|k, s_{k+1}} \tag{6.35}$$

Under this approximation, the following equalities hold:

$$-\nabla_{x_{k+1}}^2 h(x_{k+1}, n_{k+1}^{1:C}) \Big|_{x_{k+1}=x_{k+1|k,s_{k+1}}} = W_{k+1|k+1,s_{k+1}}^{-1} \tag{6.36}$$

$$p(x_{k+1} \mid s_{k+1}, H_{k+1}) \Big|_{x_{k+1}=x_{k+1|k,s_{k+1}}} = \frac{1}{(2\pi)^{m/2} \left| W_{k+1|k,s_{k+1}} \right|^{1/2}} \tag{6.37}$$

where $W_{k+1|k+1,s_{k+1}}$ is precisely the variance of the Gaussian approximation to the posterior density given in [20] and Appendix A.

Using equations (6.36) and (6.37), the Laplace approximation (6.34) simplifies to

$$p(n_{k+1}^{1:C} \mid s_{k+1}, H_{k+1}) \approx p(n_{k+1}^{1:C} \mid x_{k+1}, s_{k+1}, H_{k+1}) \Big|_{x_{k+1}=x_{k+1|k,s_{k+1}}} \tag{6.38}$$

Express $p(n_{k+1}^{1:C} \mid x_{k+1}, s_{k+1}, H_{k+1})$ using a discrete-time approximation for point processes [20]:

$$p(n_{k+1}^{1:C} \mid x_{k+1}, s_{k+1}, H_{k+1}) \propto \prod_{c=1}^{C} \exp(n_{k+1}^{c} \log(\lambda_{k+1}^{c}\delta_{k+1}) - \lambda_{k+1}^{c}\delta_{k+1}) \tag{6.39}$$

Substituting this approximation into (6.38), we have the final approximate equation for $p(n_{k+1}^{1:C} \mid s_{k+1}, H_{k+1})$:

$$p(n_{k+1}^{1:C} \mid s_{k+1}, H_{k+1}) \approx \frac{\left|W_{k+1|k+1,s_{k+1}}\right|^{1/2}}{\left|W_{k+1|k,s_{k+1}}\right|^{1/2}} \prod_{c=1}^{C} \exp(n_{k+1}^{c} \log(\lambda_{k+1}^{c}\delta_{k+1}) - \lambda_{k+1}^{c}\delta_{k+1}) \Bigg|_{x_{k+1}=x_{k+1|k,s_{k+1}}} \tag{6.40}$$

■

6.9.4 (Section 4) Spike filtering with the hybrid framework: practical note on numerical issues

This section documents four points to consider when implementing the hybrid filter:

1. The spike filtering (hybrid point process) filter described in this paper uses a bank of stochastic state point process filters (SSPF), described in [20] and Methods, Section A. As with the SSPF, the prediction or posterior covariance may become singular because of numerical implementation, or badly conditioned if the values in certain matrix elements are dramatically smaller than others. In a practical implementation, it is useful to check that a covariance matrix is well-conditioned or invertible before taking the inverse operation required by the SSPF (also described in Methods, Section A). If the posterior covariance is not invertible, perform a Fisher's scoring step instead of executing the posterior covariance equation, by removing the $-\left(n_k^c - \lambda_k^c \Delta\delta_k\right)\frac{\partial^2 \log \lambda_k^c}{\partial x_k}$ term of the posterior

covariance equation for just that timestep. If the prediction covariance is badly conditioned, retain the prediction covariance as the posterior covariance.

2. You may encounter divide-by-zero or floating-point errors if you incorrectly implement the nine step spike filtering procedure. Check that you are not dividing by a discrete state probability that has approached zero.

3. To generate smoother continuous state trajectories, such as in Example 3 of the paper, augment your state space to include acceleration terms, and introduce the non-zero diagonal term of increment covariance only in the acceleration dimensions.

4. Note that Example 3 is a discrete-target version of problem of reaching to drifting targets [24] that evolve over a continuum of positions. The discrete nature of the targets in Example 3 necessitates the hybrid framework. Similarly, look for parallels between your application and discrete or continuous versions of it.

6.10 References

[1] J. R. Wolpaw and D. J. McFarland, "Control of a two-dimensional movement signal by a noninvasive brain-computer interface in humans," *Proc Natl Acad Sci U S A*, vol. 101, pp. 17849-54, 2004.

[2] E. C. Leuthardt, G. Schalk, J. R. Wolpaw, J. G. Ojemann, and D. W. Moran, "A brain-computer interface using electrocorticographic signals in humans," *J Neural Eng*, vol. 1, pp. 63-71, 2004.

[3] J. M. Carmena, M. A. Lebedev, R. E. Crist, J. E. O'Doherty, D. M. Santucci, D. F. Dimitrov, P. G. Patil, C. S. Henriquez, and M. A. Nicolelis, "Learning to control a brain-machine interface for reaching and grasping by primates," *PLoS Biol*, vol. 1, pp. E42, 2003.

[4] M. D. Serruya, N. G. Hatsopoulos, L. Paninski, M. R. Fellows, and J. P. Donoghue, "Instant neural control of a movement signal," *Nature*, vol. 416, pp. 141-2, 2002.

[5] D. M. Taylor, S. I. Tillery, and A. B. Schwartz, "Direct cortical control of 3D neuroprosthetic devices," *Science*, vol. 296, pp. 1829-32, 2002.

[6] K. V. Shenoy, D. Meeker, S. Cao, S. A. Kureshi, B. Pesaran, C. A. Buneo, A. P. Batista, P. P. Mitra, J. W. Burdick, and R. A. Andersen, "Neural prosthetic control signals from plan activity," *Neuroreport*, vol. 14, pp. 591-6, 2003.

[7] S. Musallam, B. D. Corneil, B. Greger, H. Scherberger, and R. A. Andersen, "Cognitive control signals for neural prosthetics," *Science*, vol. 305, pp. 258-62, 2004.

[8] T. A. Kuiken, G. A. Dumanian, R. D. Lipschutz, L. A. Miller, and S. K.A., "Targeted muscle reinnervation for improved myoelectric prosthesis control," *Proc 2nd Internat IEEE EMBS Conf on Neural Engineering*, pp. 396-399.

[9] D. D. Frey, L. E. Carlson, and V. Ramaswamy, "Voluntary-Opening Prehensors with Adjustable Grip Force," *Journal of Prosthetics & Orthotics*, vol. 7, pp. 124-131, 1995.

[10] J. R. Wolpaw, N. Birbaumer, D. J. McFarland, G. Pfurtscheller, and T. M. Vaughan, "Brain-computer interfaces for communication and control," *Clin Neurophysiol*, vol. 113, pp. 767-91, 2002.

[11] A. B. Schwartz, "Cortical neural prosthetics," *Annu Rev Neurosci*, vol. 27, pp. 487-507, 2004.

[12] R. A. Andersen, J. W. Burdick, S. Musallam, B. Pesaran, and J. G. Cham, "Cognitive neural prosthetics," *Trends Cogn Sci*, vol. 8, pp. 486-93, 2004.

[13] A. Kubler, V. K. Mushahwar, L. R. Hochberg, and J. P. Donoghue, "BCI Meeting 2005 - Workshop on Clinical Issues and Applications," *IEEE Trans Biomed Eng*, vol. 14, pp. 131-134, 2006.

[14] M. A. Lebedev and M. A. Nicolelis, "Brain Machine Interfaces: Past, Present, Future," *Trends Neurosci*, In Press, 2006.

[15] J. R. Wolpaw and D. J. McFarland, "Multichannel EEG-based brain-computer communication," *Electroencephalogr Clin Neurophysiol*, vol. 90, pp. 444-9, 1994.

[16] A. P. Georgopoulos, A. B. Schwartz, and R. E. Kettner, "Neuronal population coding of movement direction," *Science*, vol. 233, pp. 1416-9, 1986.

[17] J. Wessberg, C. R. Stambaugh, J. D. Kralik, P. D. Beck, M. Laubach, J. K. Chapin, J. Kim, S. J. Biggs, M. A. Srinivasan, and M. A. Nicolelis, "Real-time prediction of hand trajectory by ensembles of cortical neurons in primates," *Nature*, vol. 408, pp. 361-5, 2000.

[18] W. Wu, Y. Gao, E. Bienenstock, J. P. Donoghue, and M. J. Black, "Bayesian population decoding of motor cortical activity using a Kalman filter," *Neural Comput*, vol. 18, pp. 80-118, 2006.

[19] A. E. Brockwell, A. L. Rojas, and R. E. Kass, "Recursive bayesian decoding of motor cortical signals by particle filtering," *J Neurophysiol*, vol. 91, pp. 1899-907, 2004.

[20] U. T. Eden, L. M. Frank, R. Barbieri, V. Solo, and E. N. Brown, "Dynamic analysis of neural encoding by point process adaptive filtering," *Neural Comput*, vol. 16, pp. 971-98, 2004.

[21] R. Barbieri, M. C. Quirk, L. M. Frank, M. A. Wilson, and E. N. Brown, "Construction and analysis of non-Poisson stimulus-response models of neural spiking activity," *J Neurosci Methods*, vol. 105, pp. 25-37, 2001.

[22] L. Srinivasan, U. T. Eden, A. S. Willsky, and E. N. Brown, "A State-Space Analysis for Reconstruction of Goal-Directed Movements using Neural Signals," *Neural Computation*, vol. 18 (10), 2006.

[23] L. Srinivasan, U. T. Eden, A. S. Willsky, and E. N. Brown, "Goal-directed state equation for tracking reaching movements using neural signals," *Proc 2nd Internat IEEE EMBS Conf on Neural Engineering*, pp. 352-355, 2005.

[24] L. Srinivasan and E. N. Brown, "Dynamic-goal state equations for tracking reaching movements using neural signals," *1st IEEE RAS-EMBS Internat Conf on Biomed Robotics and Biomechatronics (BioRob '06)*, 2006.

[25] W. Wu, M. J. Black, D. Mumford, Y. Gao, E. Bienenstock, and J. P. Donoghue, "Modeling and decoding motor cortical activity using a switching Kalman filter," *IEEE Trans Biomed Eng*, vol. 51, pp. 933-42, 2004.

[26] T. M. Cowan and D. M. Taylor, "Predicting reach goal in a continuous workspace for command of a brain-controlled upper-limb neuroprosthesis," *Proc 2nd Internat IEEE EMBS Conf on Neural Engineering*, pp. 74, 2005.

[27] C. Kemere, M. Sahani, and T. H. Meng, "Robust neural decoding of reaching movements for prosthetic systems," *Proc 25th Annual Meeting IEEE EMBS*, vol. 3, pp. 2079 - 2082, 2003.

[28] C. Kemere and T. H. Meng, "Optimal estimation of feed-forward-controlled linear systems," *Proc IEEE International Conference on Acoustics, Speech and Signal Processing (ICASSP '05)*, vol. 5, pp. 353-356, 2005.

[29] B. M. Yu, C. Kemere, G. Santhanam, A. Afshar, S. I. Ryu, T. H. Meng, M. Sahani, and K. V. Shenoy, "Mixture of trajectory models for neural decoding of goal-directed movements," *Society for Neuroscience Abstract Viewer/Itinerary Planner, Program No. 520.18*, 2005.

[30] M. P. Tarvainen, J. K. Hiltunen, P. O. Ranta-aho, and P. A. Karjalainen, "Estimation of Nonstationary EEG With Kalman Smoother Approach: An Application to Event-Related Synchronization (ERS)," *IEEE Transactions on Biomedical Engineering*, vol. 51, pp. 516-524, 2004.

[31] D. L. Snyder and M. I. Miller, *Random point processes in time and space*, 2nd ed. New York: Springer-Verlag, 1991.

[32] D. J. Daley and D. Vere-Jones, *An introduction to the theory of point processes*, 2nd ed. New York: Springer, 2003.

[33] E. N. Brown, "Theory of Point Processes for Neural Systems," in *Methods and Models in Neurophysics*, C. C. Chow, B. Gutkin, D. Hansel, C. Meunier, and J. Dalibard, Eds. Paris: Elsevier, 2005, pp. 691-726.

[34] E. N. Brown, R. Barbieri, V. Ventura, R. E. Kass, and L. M. Frank, "The time-rescaling theorem and its application to neural spike train data analysis," *Neural Comput*, vol. 14, pp. 325-46, 2002.

[35] K. Murphy, "Switching Kalman Filters," *U. C. Berkeley Technical Report*, 1998, citeseer.ist.psu.edu/article/murphy98switching.html.

[36] B. M. Yu, G. Santhanam, S. I. Ryu, and K. V. Shenoy, "Feedback-directed state transition for recursive Bayesian estimation of goal-directed trajectories," *Computational and Systems Neuroscience (COSYNE) meeting abstract, Salt Lake City, UT*, 2005.

[37] W. Truccolo, U. T. Eden, M. R. Fellows, J. P. Donoghue, and E. N. Brown, "A point process framework for relating neural spiking activity to spiking history, neural ensemble, and extrinsic covariate effects," *J Neurophysiol*, vol. 93, pp. 1074-89, 2005.

[38] T. P. McGarty, *Stochastic systems and state estimation*. New York: Wiley, 1974.

[39] Y. Bar-Shalom, X.-R. Li, and T. Kirubarajan, *Estimation with applications to tracking and navigation : theory, algorithms and software*. New York: Wiley, 2001.

[40] B. Pesaran, S. Musallam, and R. A. Andersen, "Cognitive neural prosthetics," *Curr Biol*, vol. 16, pp. R77-80, 2006.

[41] N. Hatsopoulos, J. Joshi, and J. G. O'Leary, "Decoding continuous and discrete motor behaviors using motor and premotor cortical ensembles," *J Neurophysiol*, vol. 92, pp. 1165-74, 2004.

[42] D. W. Moran and A. B. Schwartz, "Motor cortical representation of speed and direction during reaching," *J Neurophysiol*, vol. 82, pp. 2676-92, 1999.

[43] C. S. Li, C. Padoa-Schioppa, and E. Bizzi, "Neuronal correlates of motor performance and motor learning in the primary motor cortex of monkeys adapting to an external force field," *Neuron*, vol. 30, pp. 593-607, 2001.

[44] R. A. Andersen and C. A. Buneo, "Intentional Maps in Posterior Parietal Cortex," *Annual Review of Neuroscience*, vol. 25, pp. 189-220, 2002.

[45] M. Weinrich and S. P. Wise, "The premotor cortex of the monkey," *J Neurosci*, vol. 2, pp. 1329-45, 1982.

[46] J. D. Schall, "Neural basis of deciding, choosing and acting," *Nat Rev Neurosci*, vol. 2, pp. 33-42, 2001.

[47] E. Todorov, "Optimality principles in sensorimotor control," *Nat Neurosci*, vol. 7, pp. 907-15, 2004.

[48] D. P. Bertsekas, *Dynamic programming and optimal control*, 3rd ed. Belmont, Mass.: Athena Scientific, 2005.

[49] U. T. Eden, W. Truccolo, M. R. Fellows, J. P. Donoghue, and E. N. Brown, "Reconstruction of hand movement trajectories from a dynamic ensemble of spiking motor cortical neurons," *Proc 26th IEEE Engineering in Medicine and Biology Society Annual Conference (EMBC '04)*, vol. 2, pp. 4017- 4020, 2004.

[50] E. N. Brown, L. M. Frank, D. Tang, M. C. Quirk, and M. A. Wilson, "A statistical paradigm for neural spike train decoding applied to position prediction from ensemble firing patterns of rat hippocampal place cells," *J Neurosci*, vol. 18, pp. 7411-25, 1998.

Chapter 7

Conclusion

7.1 Summary of Results

We first (Chapter 4) addressed several questions regarding the representation of visually-presented targets in the spiking activity of dorsal premotor cortex (PMd) neurons during an instructed delay period before reaching movements. How can PMd be characterized during the instructed delay period before an arm reaching task as a time-invariant ensemble spiking representation of the visually-presented target? How is this characterization interpreted in terms of physiological mechanism and function? How can this characterization advance medical technology?

We concluded that delay period spiking activity in PMd supports the representation of targets through a point process with temporal and history dependence, generated by local and possibly distant neural interactions. Results suggested that a downstream neural movement controller or neural prosthetic device could exploit these dependencies to select targets faster and more reliably.

The analysis comprised three steps:

1. Model description. The millisecond-by-millisecond spiking probabilities were modeled. Previous studies described only total spike counts during the delay period.

2. Model selection. Models were compared with Akaike Information Criterion (AIC) and verified using time rescaling statistics. Previous studies have no direct model verification procedure.

3 Inference. Point process filtering was used to evaluate the quality of target representation as it scaled with time post-stimulus-onset and ensemble size. This analysis was cross-validated in three ways (leave-one-out, leave-zero-out, and simulated) in order to understand the extent to which alternate models suffered from over- or underfitting.

These three steps represent a general prescription for the analysis and interpretation of spiking activity in experiments on the representation of stimuli drawn from a discrete set.

Next (Chapter 5), we investigated how reaching movements can be coordinated with neural activity that corresponds to both the current arm state and the target of the movement. We presented a solution that defines reaching movements as a description of free arm movement (a linear Gauss-Markov process) that is analytically restricted to a target. The resulting state equation can be used with diverse measurement approaches and filtering techniques to reconstruct arm movements from target and path related neural activity.

Finally (Chapter 6), we described the mapping between neural signals and prosthetic device states as an estimation problem where feedback was ignored, in sufficiently general terms as to unify the dominant Bayesian approaches to neural prosthetics design. To support a general-purpose neural prosthetic algorithm, the user’s intentions were described in a state space of interacting discrete- and continuous-valued Markov processes. An approximate discrete-time filtering procedure was developed on this hybrid state space for point process observations. Previous approaches to estimation in neural prosthetics were unified by this framework, which was predicted to improve performance in a simulated reaching task to switching targets. This framework can be readily extended with developments in hardware design, new applications, and discoveries in neuroscience.

7.2 Continuing Research

The work presented in this thesis lends itself to several avenues of further investigation. The study on target representation in PMd (Chapter 4) should be expanded to understand the extent to which target representations generalize across different experimental scenarios, and especially in the context of reaching movements without explicitly instructed delay periods. If these representations of target do change, then how do downstream neural circuits continue to effect reliable arm placement in the face of a changing PMd target representation? Furthermore, all models investigated suffered in part from either under- or overfitting. Anatomical constraints could be introduced in order to simultaneously simplify the models and improve their predictive power.

The reconstruction of reaching movements from target and path related activity (Chapter 5) could be applied to an empirical analysis of neural data from various target and path related regions to understand how those regions might cooperate in specifying trajectories. Estimation based on this approach can also help in model selection similar to the application of cross-validation in Chapter 4. As an alternative, models of reaching movements can be trained on empirical databases of movement trajectories from the particular animal being studied to provide subject-specific priors.

In the context of neural prosthetic devices, closed-loop experiments will be crucial to evaluating both the control of reaching movements (Chapter 5) and the general design framework (Chapter 6) against alternate approaches. In these experiments, the user can receive feedback on the estimated reaching movement, and make online adjustments to neural output. The general framework (Chapter 6) is applicable both to movement control and an emerging class of prostheses for individuals with communication disorders. Successful design approaches will need to address human factors that affect ease of use and reliability, as well as the specific nature and extent of the user's neurological deficits. Ultimately, the principled design of algorithms for these advanced medical applications will rely on the characterization of neural systems through mathematical descriptions that are amenable to engineering, and design approaches that consider the essential features of human-machine interaction.